Molecular Beam Heteroepitaxial Growth and Characterization of Wide Band Gap Semiconductor Films and Devices

Thesis by

Eric C. Piquette

In Partial Fulfillment of the Requirements
for the Degree of
Doctor of Philosophy

California Institute of Technology
Pasadena, California

1999

(Submitted May 11, 1999)

To the One,

my family

and the snails under the bridge.

Acknowledgements

This thesis would not have been possible without the technical and personal support of a number of people. Of primary influence to me and my research in the last five years has been my advisor, Dr. Tom McGill. Tom is a man with great efficiency of influence. He has provided an environment which is conducive to both high caliber research as well as the personal and professional growth of graduate students, in whom he has both high confidence and high expectations. I consider myself very fortunate to have had the opportunity to work with so many talented people as a member of Tom's Solid State Device Physics group.

Jim McCaldin, Ogden Marsh, and Gerry Picus were all of immense help and motivation throughout my time at Caltech. Dr. McCaldin was the inventor and senior investigator for the work done on ZnS/GaN heterojunctions. Ogden Marsh is a fountain of technical knowledge, not to mention a really nice guy. No doubt I am much the better for their acquaintance.

The group could not function without the person in the office next to Tom's. Marcia Hudson contributed to the group's success (and good morale) as much as any student or senior member. Many thanks to Gloria Pendlay for purchase orders and everything else. Most recently, Tim Harris has been a big help to all of us, for which I am very grateful.

I owe much of what I learned about being a graduate student to Johannes Swenberg, Mike Wang, Doug Collins, Per-Olov Pettersson, and Erik Daniel. Johannes gave me my initial training in the art of molecular beam epitaxy, while Doug and Per-Olov were always willing to divulge their knowledge of various experimental equipment. If ever requiring the services of someone who really knows what they are doing, Erik Daniel fits the bill. Thanks, Erik, for teaching me more things than I can recall, and for introducing me to Jackie Chan. I am also glad I had the opportunity to know David Ting. David has always been a good one to ask regarding things theoretical,

and if you get on his good side he is also a good source of baby supplies!

No doubt what I will remember most about my time at Caltech is my interaction with fellow students. Alicia Alonzo and Xiao-Chang Cheng have come through it all with me. Xiao-Chang and I . . . lords of the clean room. Alicia has that friendly personality that always makes me smile. I'm glad to have known her both in the lab and at St. Philips.

It is my honor to have known and worked with Zvonimir Bandić, whom I consider one of the smartest and most talented people I have ever met. Many of the results presented in this thesis are the fruit of my collaboration with Zvonimir. He performed most of the work involving high power nitride devices, including device design, fabrication of high voltage diodes, and EBIC measurement of minority carrier diffusion lengths. Zvonimir also performed most of the photoluminescence measurements presented here, as well as gave me great assistance with SEM, etching, sputtering, and other experiments. I will always recall the trips we took together to Boston for the MRS meetings.

I would like to thank Paul Bridger for helping me with AFM and for many fruitful discussions. I hope he can forgive me for all my "unbelieving" critiques of his very interesting work. Thanks to Robert Beach for XPS and assisting me with the nitride growth; also for trying to teach me how to ride the surf. Thanks to Cory Hill for permforming PL measurements of p-type GaN. It's always fun to talk shop with Cory, from computers to the stock market. Likewise to Joel Jones, the "other" MBE grower. It has also been my pleasure to work with Matt Barton and Xavier Cartoixa – I forsee them having bright futures.

I would also like to express my thanks to those who supplied the funding that made this research possible: Dr. Larry Cooper, Dr. Y.-S. Park, and Dr. John Zolper of the Defense Advanced Research Projects Agency. My best regards to Greg Carpenter, Peter Chow, and Jim Van Hove of SVT Associates – this thesis would not be possible without them as they built our nitride MBE machine.

My thanks also to James Boyk and the Caltech music lab for making my experience here a richer one. To John and Kit Ruminer, Phyllis Russo, and especially Greg

Shepard at Los Alamos, for nurturing a young soul. To the Law family, for being "our family" in Pasadena.

And special thanks go to my wife and family, without whom I would not be who I am.

List of Publications

Work related to this thesis has been or will be published under the following titles:

Effect of Buffer Layer and III/V Ratio on the Surface Morphology of GaN Grown by MBE,

E. C. Piquette, P. M. Bridger, R. A. Beach, Z. Z. Bandić, and T. C. McGill, *MRS Internet J. Nitride Semicond. Res.* **4S1**, G3.77 (1999).

Morphology, polarity, and lateral molecular beam epitaxy growth of GaN on sapphire,

E. C. Piquette, P. M. Bridger, Z. Z. Bandić, and T. C. McGill, to be published in *J. Vac. Sci. Technol. B* **17**(3), (1999).

Growth of III-Nitrides by RF-Assisted Molecular Beam Epitaxy,

E. C. Piquette, P. M. Bridger, Z. Z. Bandić, and T. C. McGill, *Mat. Res. Soc. Symp. Proc.* **512**, 387 (1998).

Experimental Study of Sputter Deposited Contacts to Gallium Nitride,

E. C. Piquette, Z. Z. Bandić, and T. C. McGill, *Mat. Res. Soc. Symp. Proc.* **482**, 1089 (1998).

Growth and Characterization of Light Emitting ZnS/GaN Heterostructures,

E. C. Piquette, Z. Z. Bandić, J. O. McCaldin, and T. C. McGill, *J. Vac. Sci. Technol. B* **15**(4), 1148 (1997).

MBE Growth and Characterization of ZnS/GaN Heterostructures,

E. C. Piquette, Z. Z. Bandić, J. O. McCaldin, and T. C. McGill, *Mat. Res. Soc. Symp. Proc.* **449**, 385 (1997).

The Values of Minority Carrier Lifetime and their Implications for Bipolar Devices,

Z. Z. Bandić, E. C. Piquette, P. M. Bridger, and T. C. McGill, Workshop on wide bandgap bipolar devices, January 1999.

XPS Study of Oxygen Adsorption on (3x3) Reconstructed MBE Grown GaN Surfaces,

R. A. Beach, E. C. Piquette, Z. Z. Bandić, and T. C. McGill, *MRS Internet J. Nitride Semicond. Res.* **4S1**, G6.26 (1999).

Design of GaN/AlGaN High Power Devices,

Z. Z. Bandić, E. C. Piquette, P. M. Bridger, T. F. Kuech, and T. C. McGill, accepted for publication in proceedings of the Electrochemical Society.

Nitride Based High Power Devices: Transport Properties, Linear Defects and Goals,

Z. Z. Bandić, P. M. Bridger, E. C. Piquette, T. F. Kuech, and T. C. McGill, *Mat. Res. Soc. Symp. Proc.* **512**, 27 (1998).

Correlation between the surface defect distribution and minority carrier transport properties in GaN,

P. M. Bridger, Z. Z. Bandić, E. C. Piquette, and T. C. McGill, *Appl. Phys. Lett.* **73**(23), 3438 (1998).

Nitride Based High Power Devices: Design and Fabrication Issues,

Z. Z. Bandić, E. C. Piquette, P. M. Bridger, R. A. Beach, T. F. Kuech, and T. C. McGill, Solid State Electronics **42**, 2289 (1998).

High Voltage (450 V) GaN Schottky Rectifiers,

Z. Z. Bandić, P. M. Bridger, E. C. Piquette, T. C. McGill, R. P. Vaudo, V. M. Phanse, and J. M. Redwing, *Appl. Phys. Lett.* **74**(9), 1266 (1999).

Electron diffusion length and lifetime in *p*-type GaN,

Z. Z. Bandić, P. M. Bridger, E. C. Piquette, and T. C. McGill, *Appl. Phys. Lett.* **73**(22), 3276 (1998).

Minority carrier diffusion length and lifetime in GaN,

Z. Z. Bandić, P. M. Bridger, E. C. Piquette, and T. C. McGill, *Appl. Phys. Lett.* **72**(24), 3166 (1998).

Solid phase recrystallization of ZnS thin films on sapphire,

Z. Z. Bandić, E. C. Piquette, J. O. McCaldin, and T. C. McGill, *Appl. Phys. Lett.* **72**(22), 2862 (1998).

Design and Fabrication of Nitride Based High Power Devices,

Z. Z. Bandić, E. C. Piquette, P. M. Bridger, T. F. Kuech, and T. C. McGill, *Mat. Res. Soc. Symp. Proc.* **483**, 399 (1998).

Compositionally Dependent Band Offsets in AlN/$Al_xGa_{1-x}N$ Heterojunctions Measured by Using X-Ray Photoelectron Spectroscopy,

R. A. Beach, E. C. Piquette, R. W. Grant, and T. C. McGill, *Mat. Res. Soc. Symp. Proc.* **482**, 775 (1998).

Abstract

The thesis consists of two parts. Part I describes work on the molecular beam epitaxial (MBE) growth of GaN, AlN, and $Al_xGa_{1-x}N$ alloys, as well as efforts in the initial technical development and demonstration of nitride-based high power electronic devices. The major issues pertaining to MBE growth are discussed, including special requirements of the growth system, substrates, film nucleation, n- and p-type doping, and the dependence of film quality on growth parameters. The GaN films were characterized by a variety of methods, including high resolution x-ray diffraction, photoluminescence, and Hall effect measurement. It is found that the film polarity and extended defect density as well as quality of photoluminescence and electrical transport properties depend crucially on how the nitride layer is nucleated on the substrate and how the subsequent film surface morphology evolves, which can be controlled by the growth conditions. A technique is proposed and demonstrated that utilizes the control of morphology evolution to reduce defect density and improve the structural quality of MBE GaN films.

In addition to growth, the design and processing of high voltage GaN Schottky diodes is presented, as well as an experimental study of sputter-deposited ohmic and rectifying metal contacts to GaN. Simple models for high power devices, based on materials properties such as minority carrier diffusion length and critical electric breakdown field, are used to estimate the voltage standoff capability, current carrying capacity, and maximum operating frequency of unipolar and bipolar GaN power devices. The materials and transport properties of GaN pertinent to high power device design were measured experimentally. High voltage Schottky rectifiers were fabricated which verify the impressive electric breakdown field of GaN (2-5 MV/cm). Electron beam induced current (EBIC) experiments were also conducted to measure the minority carrier diffusion length for both electrons and holes in GaN.

Part II of the thesis describes studies of the MBE growth of ZnS and investigations

of ZnS/GaN light emitting heterojunctions which show promise for application as blue and green light emitters. Zinc sulfide layers doped with Ag and Al were grown by MBE on sapphire, GaAs, and GaN substrates and characterized by x-ray diffraction and photoluminescence. Preliminary current-voltage and electroluminescence results are presented for a processed ZnS:Al,Ag/GaN:Mg prototype blue light emitting device.

Contents

List of Figures

List of Tables

Glossary of Acronyms

AFM	atomic force microscopy
CL	cathodoluminescence
GSMBE	gas source MBE
HVPE	hydride (or halide) vapor phase epitaxy
IR	infrared
LED	light-emitting diode
MBE	molecular-beam epitaxy
MOCVD	(=OMVPE=MOVPE) metalorganic chemical vapor deposition
MOMBE	metalorganic molecular-beam epitaxy
MOVPE	(=MOCVD=OMVPE) organometallic vapor-phase epitaxy
OMVPE	(=MOCVD=MOVPE) metalorganic vapor-phase epitaxy
PL	photoluminescence
RF	radio frequency
RFMBE	(=RF-MBE) radio frequency plasma assisted MBE
SEM	scanning electron microscopy
SIMS	secondary ion mass spectroscopy
TEM	transmission electron microscopy
UHV	ultra-high vacuum
UID	unintentionally doped
VASE	variable angle spectroscopic ellipsometery
XPS	X-ray photoemission spectroscopy
XTEM	cross sectional tramsmission electron microscopy

Chapter 1 Introduction

1.1 Introduction to thesis

This thesis consists of two parts. Part I describes research in the growth of gallium nitride by molecular beam epitaxy and in the development of GaN-based high power devices. Part II describes a proposed light emitting device based on the ZnS/GaN heterojunction and presents results for the MBE growth and characterization of ZnS layers as well as the fabrication of prototype ZnS/GaN blue LEDs. Both parts of the thesis deal with the growth of highly mismatched heteroepitaxial systems and the ways of overcoming the difficulties of this mismatch to realize the promise of these wide band gap semiconductor materials.

1.1.1 Note on collaboration

Some of the results presented in this thesis were obtained as part of a collaboration between several researchers. The high power nitride device research as well as development of the ZnS/GaN light emitter was an effort involving the author, Z. Bandić [1], and to a lesser extent P. Bridger [2]. At several places in this thesis it is desirable, in order to achieve the desired context, to describe results that were obtained by my collaborators. In particular, the ZnS solid-phase recrystallization (section 8.4), the EBIC measurements of minority carrier diffusion lengths in GaN (section 5.5), and the fabrication of high voltage HVPE diodes (section 5.4) were carried out for the most part by Z. Bandić. The results of my collaborators are clearly labeled as such in the succeeding chapters.

1.2 General motivation

The suitability of the wide band gap semiconductors for application in optoelectronics throughout the visible range and into the ultra-violet has long been known. Their ability to sustain high electric fields without breakdown also makes them desirable for high voltage device applications [3, 4]. Past difficulties regarding the growth, doping, and processing of these materials have, however, caused them to remain largely unstudied. As a result, they have until recently been relatively uncharacterized and the procedure for MBE growth far from established.

1.2.1 Group III-nitrides

Visible and UV optoelectronics

The group III-nitrides present a very versatile materials system, with direct band gaps ranging from 1.9 eV (InN) to 6.2 eV (AlN) in the wurtzite crystal structure. The direct bandgap allows high efficiency light emitters throughout the visible range [5]. The surge of interest in GaN since 1989 has brought forth a number of exciting applications. Light emitting diodes based on the nitrides are expected to ultimately replace more conventional light sources such as traffic lights and incandescent light bulbs. The exceptional energy efficiency of the nitride LEDs offers up to a ten-fold energy savings over conventional light bulbs [6] while their lifetime of 10^6 hours (over 100 years) is especially remarkable compared with the $10^3 - 10^4$ hour lifetime of incandescent bulbs. White LEDs developed by Nichia Chemical Industries, Ltd. [7], if used for home lighting, may almost never need replacement. Ultraviolet electrically injected semiconductor GaN-based lasers will allow a leap ahead in laser printing resolution [8] and optical storage density. The shorter wavelength of UV lasers supports a smaller spot size on optical media, allowing a quadrupling of storage space for advanced compact discs and DVDs. Photodetectors based on GaN can be made visible-blind. With the addition of some Al, solar-blind AlGaN detectors can be made, which are of interest to the military for detection of missile exhaust plumes.

The nitrides have very high melting points ($T_{M,GaN} \simeq 2800$ K) and are hard and robust refractory compounds, which makes them suitable for device applications in high temperature and extreme environments. They are resistant to etching or solution by almost any reagent. An important added benefit of the III-nitrides is that they are not composed of toxic materials, and so are environmentally friendly as compared to other III-V and II-VI materials.

III-nitride high power devices

In chapter 5 we discuss the use of GaN and AlGaN for high power switching and rectifying applications. These materials have the potential of revolutionizing the power industry, from AC/DC converters, to electric motor drives, to national power grid management, because they can possibly be made more power efficient and smaller in size than the current technology. Both domestic and military electric vehicles using these light weight, power efficient nitride-based devices would have diminished energy consumption and longer travel range.

1.2.2 Group II-sulfides and ZnS/GaN junctions

The other wide gap material presented in this thesis, zinc sulfide, has been put to wide use as a phosphor, and its luminescence properties have been widely studied. Yet even though the zinc chalcogenides were used as phosphors for decades before the first semiconductor p-n junctions were made, they were left behind in the semiconductor revolution of Si and Ge. Reports of MBE growth of ZnS are extremely sparse in the literature. One of the possible applications we envision for the ZnS/GaN heterojunction devices is low power, full color flat panel electroluminescent displays. These displays could be made large area, competing with other flat-panel display technologies such as active matrix liquid crystal displays, plasma displays, or field emission displays. The ZnS/GaN displays would also make a light weight, low power, personal head mounted viewer, such as virtual reality goggles, with the added safety advantage of not placing high voltages or vacuum tubes near the eye.

1.3 Summary of results

1.3.1 MBE growth of group III-nitrides and high power devices

Growth of GaN by RF-MBE

GaN, AlN, and $Al_xGa_{1-x}N$ were grown by radio frequency plasma assisted molecular beam epitaxy (RF-MBE) on sapphire substrates. Plasma-assisted MBE of nitrides is a very young field, and still requires significant development of the basic aspects of the technique. This thesis documents the development of the GaN MBE growth capability of the McGill research group as well as our study of the microstructure and morphology of MBE-grown GaN films, and presents methods for optimizing the surface morphology and defect density of MBE-grown GaN.

The conditions of film nucleation and buffer layer deposition were found to be of high importance. The nucleation conditions determine the polarity of the GaN film on sapphire, and set the microstructural template for subsequent growth. It was found that both N-face and Ga-face polarity films could be grown by using slightly Ga-rich conditions. This selectability of film polarity may be very valuable in the fabrication of piezo-electric or pyro-electric [9] based devices. The selectability also seems to be a unique ability of the RF-MBE growth technique, because MOCVD and HVPE are known to grow Ga-polar material, and under the conditions when N-polarity is nucleated, the films are of poor quality with pyramidal faceted surface morphology [10].

Reflection high energy electron diffraction (RHEED) is a widely used technique in MBE, and is useful for the growth of GaN as well. RHEED can be used quite effectively for the real-time optimization of growth conditions in the nitrides. Spotty RHEED patterns correspond to nitrogen rich growth conditions, while streaky RHEED images can be observed for Ga-rich growth, although Ga droplets can form if the Ga arrival rate is too high. The optimum crystal quality is obtained for just slightly Ga-rich growth.

Much work was focused on characterization of the surface morphology of MBE-grown GaN films by SEM and AFM. The surface morphology was found to be somewhat controllable by altering the growth parameters, specifically the N/Ga flux ratio. For even slightly N-rich growth, the surface became rough – films had a high density of dislocations and stacking faults, and a fine grained microstructure. For highly nitrogen rich growth, open "mesh-like" microstructures can result. For slightly Ga-rich growth, the surfaces were locally smooth and showed streaky RHEED patterns, but surface features such as pits and shallow canyons were visible depending on the buffer layer type, thickness, and deposition conditions. For growth of GaN films on GaN low temperature buffer layers, the surfaces showed a shallow "brain-like" texture when grown under slightly Ga-rich conditions and were very flat with small pits at the grain boundaries for more Ga-rich growth. Highly Ga-rich growth resulted in formation of Ga liquid droplet condensation. Growth on low temperature AlN buffer layers produced morphology that was highly dependent on the conditions of buffer layer deposition. For AlN buffers deposited under Al-rich flux conditions, the morphology was rougher and fine-grained, likely resulting from the nitridation of condensed aluminum at the buffer layer surface. For buffers grown under N-rich conditions, the shallow "brain-like" texture similar to growth on GaN buffers was observed. Aluminum nitride buffers grown under near "stoichiometric" conditions showed the flattest overall surfaces, but the AFM scans also revealed the presence of both large and small pits. For reasons discussed in chapter 4 the small pits are thought to arise from threading dislocations, while the larger pits are likely due to inversion domains [11]. The depth of the larger pits was seen to vary as a function of Ga/N flux ratio, becoming shallower as the Ga flux is increased. The density of the large pit defects could be reduced and eliminated for growth under more metal-rich conditions, resulting in the flattest observed surfaces (RMS roughness less than 1 nm), but the density of small pits (dislocations) remained high. It is evident from these results that production of reduced defect density material and maintaining flat morphology throughout growth may be somewhat mutually exclusive goals. An attempt was made to reduce the dislocation density in the films using a two stage growth approach. In this approach,

growth was initially proceeded under N-rich conditions, allowing the surface of the film to become rough. The second stage of growth was then conducted under Ga-rich conditions in hope of re-planarizing the surface. It was found that the morphology in the second stage corresponded to growth of micron-scale islands which were growing laterally from prominances in the rough underlying layer. This lateral growth mechanism is believed to be effective in diverting dislocations from propagation along the growth direction, resulting in films with fewer defects at the surface. The surfaces of the two-stage films did indeed show fewer small pits in the laterally grown regions, and x-ray diffraction analysis showed the two-stage films to be structurally superior to single-stage grown films.

In our study of the growth of III-nitrides, doping using Si and Mg was explored. Doping control in n-type GaN is accomplished straightforwardly by co-evaporation of Si during growth. The free electron concentration can be controlled between 10^{14} and 10^{20} by variation of Si cell temperature. Magnesium doping is relatively more difficult. As a high vapor pressure species, Mg does not have a long residence lifetime on the GaN surface and desorption is rapid. The incorporation rate is small at typical growth temperatures and is basically independent of the level of Mg flux [12]. The Mg doping level can rather be controlled by the substrate temperature, the optimum temperature being in the region of $\sim$ 700°C. Magnesium is the shallowest known acceptor in GaN and $Al_xGa_{1-x}N$, yet it is still rather deep (170-250 meV), making hole concentrations much lower than acceptor concentrations (freeze-out regime). The measured Hall mobility was rather low for n-type films, indicating a high degree of scattering from charged traps at dislocations [13, 14]. The dislocation density as estimated from mobility measurements was $\sim 10^{10}$, which is typical for MBE grown GaN films as have been reported in the literature.

GaN-based high power devices

Utilizing the favorable materials properties of GaN and $Al_xGa_{1-x}N$ in the context of high power switches and rectifier devices, the design parameters of standoff layers in Schottky diodes and thyristors were derived. Based on an analysis of Monte-Carlo-

derived impact ionization coefficients for GaN [15], it was found that the critical field for electric breakdown can be as high as 5×10^6 V/cm in GaN and even higher in $Al_xGa_{1-x}N$. It was found that due to the higher breakdown fields, standoff (depletion) layer thicknesses could be made much smaller, as compared to Si-based power devices, for the same voltage specification. The doping concentrations could likewise be increased. The thinner layers, in combination with the higher doping, leads to much reduced ON-state series resistance for a given device. For these basic reasons, it is estimated that 5 kV GaN diodes and thyristors can be made using only 18 μm thick layers, with a doping concentration of $\sim 1.3 \cdot 10^{16}$ cm^{-3}.

Of course, these numbers are estimates based on theoretical calculations, and require experimental verification before they can be considered credible. To test and verify the high breakdown field capability of GaN, therefore, Schottky diodes were fabricated using $8 - 10\,\mu$m thick GaN layers grown by HVPE. The gold Schottky diodes withstood 450-750 V in reverse bias, which corresponds to breakdown field of $(2.2-2.7)\cdot 10^6$ V/cm in an ideal planar geometry device. The lateral geometry used in this case, however, with lack of suitable edge termination, resulted in field crowding at the edges of the Schottky electrode. Because of this, these devices displayed premature edge breakdown [16], so the 2.7 MV/cm value should be taken as a lower limit. This result is of importance, because the high breakdown field property of GaN is now demonstrated. Some processing attempts at edge termination geometries were carried out, but no increase in standoff voltage could be obtained, although reverse leakage (saturation) current varied greatly with the processed device geometry. To really achieve high quality devices, guard ring structures are required which have characteristic dimensions on the micron scale and diffused dopant ring profiles, which is a difficult undertaking.

Other nitride materials properties besides breakdown field are of interest for design of high power devices. The minority carrier lifetime and diffusion length govern many facets of device operation, including allowable current density before thermal breakdown, device operating frequency, the forward resistance of bipolar devices, and the switching characteristics of two terminal thyristors. The minority carrier

transport properties of the III-nitrides had never been measured, so we performed electron beam induced current (EBIC) measurements to determine them. EBIC of both n-type and p-type GaN were investigated, revealing electron diffusion lengths of $0.2 - 2\,\mu$m depending on sample quality, and hole diffusion length of $0.28 \pm 0.02\,\mu$m. Minority carrier lifetimes estimated from these diffusion lengths using the Einstein relation are approximately 7 ns and 0.1 ns for holes and electrons, respectively.

Metallic contacts to GaN

In chapter 6, results of a study of ohmic and Schottky contacts to n- and p-type GaN are reported. The majority of work focused on sputter-deposited ohmic contacts. Many different metals were evaluated, using a range of sputtering conditions, but in the end the best results were obtained with Ti/Al contacts which have been widely studied in the literature. Gold as an ohmic contact to p-GaN was studied as a function of annealing temperature and showed rectifying dot-to-dot I-V curves. These contacts improved after annealing at up to 780°C but the I-V trace never became truly linear. Schottky gold contacts to n-GaN were measured by current-voltage analysis and showed a barrier height of $0.6 - 1.05$ eV with ideality factors from 1.4 to 4.

1.3.2 Growth and fabrication of ZnS/GaN light emitting devices

The n-ZnS/p-GaN heterojunction has been proposed as a novel visible light emitter [17]. The efforts described in this thesis are towards development and improvement of the MBE growth of ZnS crystalline films, and the fabrication of LEDs from Ag-doped ZnS grown on p-GaN substrates. Since p-GaN layers are expensive and largely unavailable, a significant amount of the ZnS growth studies was performed on sapphire substrates. Using a valved cracking source for elemental sulfur, crystalline films could be grown, but usually contained a high number of stacking faults and twins as observed by RHEED. X-ray diffraction and SEM electron channeling pattern analysis, used to characterize the ZnS structural quality, indicated that the ZnS

films were single crystalline with a high degree of mosaicity. Doping of ZnS was accomplished with aluminum and silver, which act as shallow donor and deep acceptor center, respectively. Cathodoluminescence and photoluminescence were very bright for optimally doped films, with emission centered on the 450 nm wavelength Ag blue "low energy" peak. A comparison of growths done on different substrates, including GaN, GaAs, and sapphire, demonstrated an obvious correlation between crystalline quality and luminescence intensity. ZnS films doped with Al and Ag which were grown on Mg doped GaN layers were fabricated into p-GaN:Mg/n-ZnS:(Al,Ag) LED structures. Current-voltage and electroluminescence results for these devices indicate diode-like behavior with a slow forward turn on of $3-4$ Volts. The electroluminescence spectrum is blue-violet at turn on, shifting slightly to violet emission at 15 V forward bias, where intensity saturates. This shift to violet likely indicates that electrons from the ZnS layer are transporting across the interface into the GaN layer and recombining at the deep Mg acceptor centers.

1.4 Outline of thesis

The thesis is divided into two parts. Part I (chapters 2-6) describes work on the molecular beam epitaxial growth of GaN, AlN, and $Al_xGa_{1-x}N$ alloys, as well as our efforts in the initial technical development and demonstration of nitride high power electronic devices. The major issues pertaining to growth are discussed, including special requirements of the growth system, substrates, film nucleation, and the dependence of film quality on growth parameters. In addition to growth, our work on design and processing of high voltage Schottky diodes is presented in chapter 5, and a study of metal contacts to GaN in chapter 6. Part II of the thesis describes studies of the MBE growth of ZnS and investigations of ZnS/GaN light emitting heterostructures which show promise for blue and green LEDs or RGB flat panel displays.

Chapter 2 contains an overview of the fundamentals of the nitride materials system. Although a complete discussion of all the materials issues in the nitrides is beyond the scope of this thesis, topics are presented which include crystallography

and crystal polarity issues including the piezo-electric effect, techniques for growth of GaN, substrates, delivery of active nitrogen species, n- and p-type doping of GaN and $Al_xGa_{1-x}N$, and defects in the nitrides.

Chapter 3 describes work done in the development of our group's gallium nitride growth capability by molecular beam epitaxy (MBE). The MBE technique is described and compared to other methods, such as MOCVD and HVPE, for growth of GaN. The MBE system and typical growth procedure is described, and results are shown for GaN, AlN, and $Al_xGa_{1-x}N$ growth, n-type doping with silicon, and p-type doping with magnesium. The films were characterized by a variety of methods, including high resolution x-ray diffraction, photoluminescence, and Hall effect measurement.

Chapter 4 relates a more detailed study of how the MBE growth parameters, such as gallium to nitrogen beam flux ratio, affect the microstructure and surface morphology of the GaN films. This chapter in many ways attempts to address the most significant of the nitride growth issues. The extended defect density as well as quality of photoluminescence and electrical transport properties depend crucially on how the nitride layer is nucleated on the sapphire substrate and how the subsequent morphology evolves, which can be controlled by the growth conditions. In section 4.5 a technique is proposed and demonstrated to utilize the control of morphology evolution to reduce defect density and improve the structural quality of MBE GaN films.

Chapter 5 contains results of our investigation of high power electronic devices based on GaN and $Al_xGa_{1-x}N$, specifically Schottky barrier diodes and thyristors. The design considerations for high voltage standoff layers in wide band gap semiconductors are derived. Also, it is shown how materials properties such as carrier mobility, critical electric breakdown field, and minority carrier diffusion length can affect device design and performance. To demonstrate the feasibility of GaN for high power applications, high voltage Schottky rectifiers were fabricated. These devices verify the impressive electric breakdown field of GaN ($2 - 5$ MV/cm). We also used electron beam induced current experiments to measure the minority carrier diffusion length for both electrons and holes in GaN. These diffusion length measurements,

which we used to estimate minority carrier lifetimes, are instrumental in determining the current carrying capacity, limited by thermal breakdown, of a given device as well as the switching characteristics of *p-n-p-n* two terminal thyristors. I am pleased to acknowledge Z. Bandić, who performed the major fraction of work presented in this chapter.

Chapter 6 describes work involving metallic contacts to GaN. Both Schottky and ohmic contacts were investigated. The majority of the results are comprised of a sweeping study of sputter-deposited ohmic contacts to *n*-type GaN. Seven different metals were tested using the circular transmission line (transfer length) method, which were Al, Ti/Al, W, Cr, Mo, Mg, and Ce. The specific ohmic resistance is presented for as-deposited and annealed samples. Over 750 measurements were taken, investigating the effects of sample surface preparation and sputtering deposition conditions. For rectifying contacts (including Au), which bear on the device efforts of chapter 5, the Schottky barrier height and ideality factor were measured by current-voltage analysis.

In Part II of this thesis, chapter 7 describes the basic principles of operation of *n*-ZnS/*p*-GaN light emitting diodes. Chapter 8 then reports on our efforts in the growth and fabrication of these devices. A significant amount of work was done on the MBE growth of ZnS, doped with silver and aluminum, on sapphire, GaAs, and GaN (epilayer) substrates in attempts to improve the ZnS material quality in this highly lattice mismatched system. X-ray diffraction and SEM electron channeling pattern analysis were used to characterize the ZnS structural quality, while photoluminescence and qualitative cathodoluminescence using RHEED were heavily used to optimize the silver and aluminum doping of the films. Preliminary current-voltage and electroluminescence results are presented for a processed ZnS:Al,Ag/GaN:Mg prototype blue light emitting device.

Bibliography

[1] Z. Z. Bandić, Thesis, California Institute of Technology, 1999.

[2] P. M. Bridger, Thesis, California Institute of Technology, 1999.

[3] Z.Z. Bandić, E.C. Piquette, P.M. Bridger, T.F. Kuech, and T.C. McGill, *Mat. Res. Soc. Symp. Proc.* **483** 399 (1998).

[4] Z.Z. Bandić, P.M. Bridger, E.C. Piquette, R.A. Beach, T.F. Kuech, and T.C. McGill, accepted for publication in *Solid State Electronics.*

[5] S. Nakamura, N. Senoh, N. Iwasa, and S. Nagahama, *Jpn. J. Appl. Phys. Pt. 2* **34**, L797 (1995).

[6] S. Nakamura and G. Fasol, *The Blue Laser Diode* (Springer, Berlin, 1997).

[7] S. Nakamura, *Solid State Commun.* **102**, 237 (1997).

[8] R. D. Bringans, *Mat. Res. Soc. Symp. Proc.* **482**, 1203 (1998).

[9] M. S. Shur, A. D. Bykhovski, and R. Gaska, *MRS Internet J. Nitride Semicond. Res.* **4S1**, G1.6 (1999).

[10] M. Seelmann-Eggebert, J. L. Weyher, H. Obloh, H. Zimmermann, A. Rar, and S. Porowski, *Appl. Phys. Lett.* **71**, 2635 (1997).

[11] L. T. Romano and T. H. Myers, *Appl. Phys. Lett.* **71**, 3486 (1997).

[12] S. Guha, N. A. Bojarczuk, and F. Cardone, *Appl. Phys. Lett.* **71**, 1685 (1997).

[13] N. G. Weimann, L. F. Eastman, D. Doppalapudi, H. M. Ng, T. D. Moustakas, *J. Appl. Phys.* **83**, 3656 (1998).

[14] H. M. Ng, D. Doppalapudi, T. D. Moustakas, N. G. Weimann, and L. F. Eastman, *Appl. Phys. Lett.* **73**, 821 (1998).

[15] J. Kolnik, I.H. Ogusman, K.F. Brennan, R. Wang, and P.P. Ruden, *J. Appl. Phys.* **82**, 726 (1997).

[16] B. J. Baliga, Power Semiconductor Devices, (PWS Publishing Company, Boston, 1996), p. 148.

[17] J. O. McCaldin, M. W. Wang, and T. C. McGill, *J. Cryst. Growth* **159**, 502 (1996).

Part I

MBE Growth of III-Nitride Films, Characterization and Devices

Chapter 2 Issues in the III-nitride materials system

2.1 Introduction

This chapter provides a brief introduction to the III-nitride materials system and addresses some of the issues relevant to the succeeding chapters. Section 2.2 lists some of the materials properties of GaN, InN, and AlN, such as band gap and dielectric constants. Several popular techniques that have been used for growth of the nitrides are described in section 2.3. The very pertinent issues of substrates, wurtzite crystallography (and polarity), nitrogen delivery, and doping are then discussed in the remaining sections.

2.2 Materials properties of the III-nitrides

The wide, direct bandgap of GaN, along with favorable luminescence and electronic transport properties, make the nitride system promising for a wide range of applications. When coupled with InN and AlN, the nitride alloys make up a very versatile materials system with an energy gap variable between 1.9 eV (InN) and 6.2 eV (AlN). Table 2.1 lists some of the physical parameters of GaN, AlN, and InN.

In terms of semiconductor device design, the III-nitrides offer almost unlimited possibilities. The nitride band lineups span the extremes, with reports of negative electron affinity for AlN [1, 2] on one hand, and on the other GaN, which has (along with diamond) one of the lowest lying valence bands (highest work functions) of all p-dopable materials [3]. The low lying valence band of GaN is exploited in work described in chapter 7, where p-GaN is used as a material for injection of holes into a (non-p-dopable) ZnS luminescent layer, forming structures for ZnS-based blue

Table 2.1: Select materials properties of GaN, AlN, and InN.[4]

Properties of GaN	
Wurtzite polytype	
Band gap	E_g (300 K) = 3.39 eV
	E_g (1.6 K) = 3.50 eV
Temperature coefficient	$\mathrm{d}E_g/\mathrm{d}T = -6.0 \times 10^{-4}$ eV K^{-1}
Pressure coefficient	$\mathrm{d}E_g/\mathrm{d}P = 4.2 \times 10^{-3}$ eV kbar^{-1}
Lattice constants	$a = 3.189$ Å, $c = 5.185$ Å
Thermal expansion	$\Delta a/a = 5.59 \times 10^{-6}\mathrm{K}^{-1}$
	$\Delta c/c = 3.17 \times 10^{-6}\mathrm{K}^{-1}$
Thermal conductivity	$\kappa = 1.3$ W cm^{-1} K^{-1}
Index of refraction	n (1 eV) = 2.33, n (3.38 eV) = 2.67
Dielectric constants	$\epsilon_0 \approx 9, \epsilon_\infty = 5.35$
Zinc blende polytype	
Band gap	E_g (300 K) = 3.2 − 3.3 eV
Lattice constant	$a = 4.52$ Å
Index of refraction	n (3 eV) = 2.5
Properties of AlN	
Wurtzite polytype	
Band gap	E_g (300 K) = 6.2 eV
	E_g (5 K) = 6.28 eV
Lattice constants	$a = 3.112$ Å, $c = 4.982$ Å
Thermal expansion	$\Delta a/a = 4.2 \times 10^{-6}\mathrm{K}^{-1}$
	$\Delta c/c = 5.3 \times 10^{-6}\mathrm{K}^{-1}$
Thermal conductivity	$\kappa = 2$ W cm^{-1} K^{-1}
Index of refraction	$n = 2.15 \pm 0.05$
Dielectric constants	$\epsilon_0 = 8.5 \pm 0.2, \epsilon_\infty = 4.68 - 4.84$
Zinc blende polytype	
Band gap	E_g (300 K) = 5.11 eV†
Lattice constant	$a = 4.38$ Å
Properties of InN	
Wurtzite polytype	
Band gap	E_g (300 K) = 1.89 eV
Temperature coefficient	$\mathrm{d}E_g/\mathrm{d}T = -1.8 \times 10^{-4}$ eV K^{-1}
Lattice constants	$a = 3.548$ Å, $c = 5.760$ Å
Index of refraction	$n = 2.80 - 3.05$
Zinc blende polytype	
Band gap	E_g (300 K) = 2.2 eV†

†Theoretical.

and green p-n LEDs. The large band gap of the nitrides, particularly $Al_xGa_{1-x}N$, results in a correspondingly large critical field for electric breakdown and avalanche by impact ionization. The large critical field of GaN and $Al_xGa_{1-x}N$ can be used for high performance power devices as discussed in chapter 5.

Indeed, the potential of nitrides has long been known, but only recently have modern growth techniques been applied to the production of high quality nitride films.

2.3 Techniques of growth

The potential and promising properties of the III-nitride system have been known for several decades, but the technology for production of high quality material has not, until recently, been satisfactory. Early attempts at growth of GaN employed the halide vapor phase transport technique, but the resulting material was highly defective with a high background electron concentration [5]. Several techniques have since been employed in the attempt to grow single crystal GaN.

2.3.1 Bulk growth

At first glance, perhaps the most obvious way to produce large defect free GaN wafers and crystals would be by the growth of large boules from the melt, which is a common and established technique for other elemental and compound crystals. There are a number of technical reasons why growth of bulk GaN is very difficult, however. The conditions of temperature and pressure that would be ideal for melt growth of GaN are beyond current technological capabilities. The problem lies with the group V component, nitrogen. With perhaps the strongest bond in nature (9.8 eV), N_2 is highly stable and resistant to any reaction in which it is required to dissociate, such as the solution of N in the gallium melt. Initial attempts of GaN bulk growth from nitrogen dissolved in molten gallium at high temperature and pressure have been carried out at Unipress in Poland [6]. The pressure in their growth apparatus was 20 kbar at a temperature of 1900-2000°C. To date, the largest crystals produced have

been plate-like with a plate area of up to 100 mm^2. These crystals typically have high background electron concentrations, characteristic of a high oxygen impurity content a large number of native donor point defects, unless they are intentionally compensated with magnesium acceptors [6] in which case the crystals are high resistivity. Nevertheless, even this limited success gives hope that bulk GaN may some day become commercially available, even though that time seems far off.

2.3.2 Heteroepitaxy

Since bulk crystals and free standing substrates of gallium nitride are unavailable, growth on a dissimilar substrate is necessary, and a technique for epitaxial growth must be used to produce GaN films. The methods recently used for heteroepitaxy of GaN films include sublimation [7], hydride vapor phase epitaxy (HVPE) [8], pulsed laser deposition [9], and several variations of molecular beam epitaxy (MBE), including plasma assisted MBE (RF-MBE or ECR-MBE), ammonia gas source MBE (GSMBE) [10], and metalorganic molecular beam epitaxy (MOMBE) [11]. By far the most widely used technique, however, has been metalorganic chemical vapor deposition (MOCVD), alternatively referred to as metalorganic vapor phase epitaxy (MOVPE). Akasaki and coworkers [12] as well as S. Nakamura of Nichia Chemical Industries [13] have had success in growing GaN by MOCVD on sapphire substrates, and their development of p-type doping of GaN as well as low temperature buffer layer techniques for improvement in crystal quality and surface morphology opened the flood gates for the vast amount of research interest the GaN-based materials system has received in recent years.

2.3.3 MOCVD

The MOCVD growth technique is depicted in the schematic diagram of Figure 2.1. Growth is carried out inside an inductively heated reactor. The substrate is placed on a graphite susceptor, and several gas flow lines introduce the precursor reactants to the chamber. The precursor gas for nitrogen is ammonia (NH_3), while the group

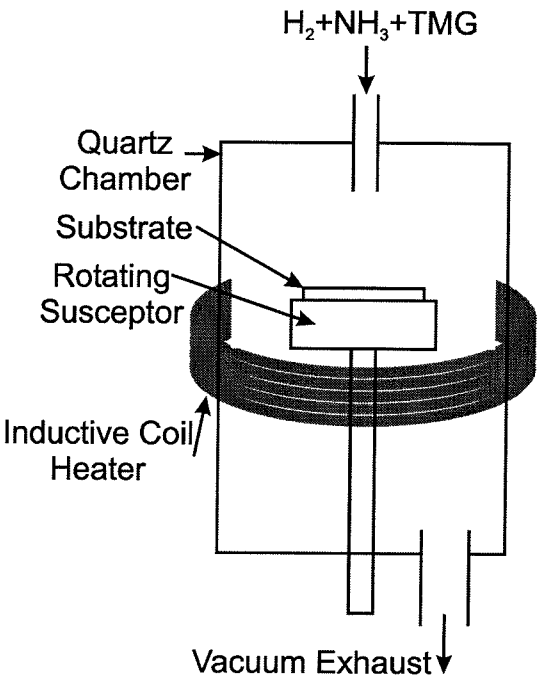

Figure 2.1: One possible configuration of an MOCVD reactor.

III precursors are the metalorganic compounds, typically trimethyl-gallium (TMG) and trimethyl-indium (TMI) for Ga and In transport, respectively, while trimethyl-aluminum (TMA) or triethyl-aluminum (TEA) are used to deliver Al. In addition to these nutrient gasses, carrier and diluent gasses such as H_2 and N_2 are used to control the convection and flow patterns within the reactor. Pressure during growth is usually between 0.1 and 1 atmospheres, while typical growth temperatures for GaN are 1050°C to 1100°C. MOCVD usually achieves 2-5 μm per hour growth rate. MOCVD has shown proven success with the fabrication of high efficiency blue, green, and yellow GaN/$In_xGa_{1-x}N$ LEDs [14, 15] and 400 nm semiconductor lasers [16, 17, 18, 19], which are now available commercially.

2.3.4 HVPE

The HVPE technique has also received renewed interest for growth of GaN and $Al_xGa_{1-x}N$. HVPE uses a reactor chamber somewhat similar to that of MOCVD (Figure 2.1), but differs in the transport of the group III species to the growth front. While MOCVD uses metalorganic vapor precursors, in HVPE hydrogen chloride HCl

gas flows over a hot reservoir of high purity liquid gallium (or In or Al), reacting to form $GaCl_3$ which then reacts with ammonia at the sample surface via the reaction $2NH_3 + 2GaCl_3 \rightarrow 2GaN + 3H_2 + 3Cl_2$ [20] to form GaN. The substrate temperature is typically 950°C to 1000°C and the reactor pressure is similar to that of MOCVD. Growth rates of GaN by HVPE can be greater than 100 μm per hour, which makes this technique very attractive for thick epilayer substrates.

2.3.5 MBE

Molecular beam epitaxy, a major focus of the work presented in this thesis, along with MOCVD and HVPE, represent the most widely used techniques for the growth of GaN. MBE is usually carried out under high or ultra-high vacuum conditions ($10^{-6} - 10^{-4}$ torr for GaN growth) and has traditionally been a useful technique for materials and device research due to the large number of *in situ* real-time diagnostic analysis techniques available, as well as because of the fine control that is possible over the thickness of constituent layers at near the atomic scale. A further description of the MBE growth technique for nitrides is presented in chapter 3, and a further comparison of the above growth techniques for GaN can be found in section 3.2.

2.4 Substrates

2.4.1 Desired substrate qualities

As heteroepitaxial growth of GaN using the techniques described above continues to be understood, and as material properties improve, it is evident that the quality of grown films is significantly hampered by the lack of a suitable substrate. Ideally, one would like to have a substrate that is lattice matched to GaN; that is, their in-plane lattice parameters are equal. A substrate should also be matched to GaN by coefficient of thermal expansion, in order to avoid lattice misfit at growth/room temperatures as well as to avoid thermally induced strain. The substrate should be chemically inert, except that it should allow nucleation of the GaN film, and it should

Table 2.2: Comparison of some substrates for GaN heteroepitaxy.

Substrate Material	a (hex) (Å)	Mismatch (%)	$\Delta\alpha_{Ta}$ ($10^{-6}K^{-1}$)	Stacking Mismatch
Al_2O_3 (0001)	4.758	16.1	-1.9	yes, NP
$6H$-SiC (0001)	3.08	3.5	1.4	yes
ZnO (0001)	3.252	-1.9	2.7	no
GaAs (111)	3.997	-20.0	~ -1	yes
Si (111)	3.840	-17	3	yes, NP
GaAs (100)	5.653	-20.0	~ -1	no

be thermally stable enough not to decompose at the typical temperatures required for nitride growth. Also, GaN is a III-V, and thus polar, compound, so an ideal substrate should provide an unambiguous anion/cation ordering template. For example, GaAs or SiC would provide an adequate polar template because of their alternating layers of atoms with different electronegativities, but Si would not. Lack of polar ordering can give rise to inversion (anti-phase) domains (section 2.5.1). A similar problem with substrates of different crystal structure is the so-called stacking mismatch, which involves the HCP stacking sequence. If a wurtzite film, with stacking sequence of (ABABAB...) is grown atop a hexagonal substrate with different stacking sequence, for example zinc blende (ABCABCABC...) or $6H$-SiC (ABCACB...), there can arise stacking mismatch boundary effects [21, 22] at step edges of the substrate.

2.4.2 Silicon carbide

There is no substance for heteroepitaxy that can satisfy all the above requirements. In the absence of the ideal, the most widely used substrates have been c-plane oriented sapphire (Al_2O_3) and the $6H$ polytype of silicon carbide. Silicon carbide has many suitable qualities as a substrate for GaN. As shown in Table 2.2, the in-plane lattice constant mismatch is 3.5% and the thermal mismatch is $1.4 \cdot 10^{-6}K^{-1}$. SiC is also a polar material, and it has been shown that GaN growth on the Si (0001) face of $6H$-SiC results in (0001) Ga face oriented GaN, while growth on the C face of SiC results in growth on the $(000\bar{1})$ N face orientation of GaN. Silicon carbide is a generally stable

and robust material, and has the advantage that it can be made conductive, both n- and p-type. Disadvantages of SiC are its high cost, the availability of only small sized substrates ($1-2$ inch diameter) and the presence of open micro-pipe defects [23]. Due to its close lattice and thermal mismatch, growth of GaN on SiC can result in epitaxial films of marginally better quality than films grown on the most widely used substrate, sapphire.

2.4.3 Sapphire

Sapphire is a very robust and chemically inert material [24]. Several surface orientations are available, including c-plane (0001), a-plane $(11\bar{2}0)$, r-plane $(1\bar{1}02)$, m-plane $(10\bar{1}0)$, n-plane $(11\bar{2}3)$, and s-plane $(10\bar{1}1)$, the most common of these used for GaN substrates being the c-plane cut. The lattice parameter and thermal expansion mismatch with GaN are rather high ($\sim 16\%$ lattice mismatch), but the cost is about 5% that of $6H$-SiC. And although sapphire is a highly ionic compound, it does not present a preferred polarity for growth. That is, the (0001) face and the $(000\bar{1})$ face of Al_2O_3 are functionally symmetric and thus control of GaN polarity becomes a significant issue. But despite the large lattice mismatch and non-polar symmetry, the highest quality light emitting devices have been grown on sapphire. In the last five years, a great deal of research has focused on the nucleation and initial stages of growth of GaN on sapphire resulting in MOCVD recipes for the production of unipolar (0001) Ga-face films with defect densities a factor of 100 below those typical of unoptimized growth. [25] To date, nearly all the highest performance GaN-based devices, including light emitting diodes [14], lasers [19], HFETs [26], and high power diodes [27] have been grown on sapphire substrates.

2.4.4 Other substrates

In addition to sapphire and silicon carbide, several other substrates have been tried for growth of GaN. Gallium arsenide (111) and (100) have been used, the (100) orientation specifically for growth of the zinc blende phase of GaN. Problems with GaAs

include its large lattice mismatch (20%), its instability at optimum GaN growth temperature, and strong interfacial reactions involving N-As anion exchange [28]. Silicon (111) substrates have been used to produce material of mediocre quality [29] but inversion domains and the harmful effects of silicon nitridation at the interface are problems. Also receiving some attention are more "exotic" oxide substrates such as spinel ($MgAl_2O_4$, 9.5% mismatch [30]), $LiGaO_2$ [31], $LiAlO_3$ [32], $LiGaO_3$ [33], and $NdGaO_3$ [34], which are closely lattice matched to GaN, but suffer from instability at high temperatures and other problems. The wurtzite crystal ZnO is also a promising substrate candidate, having a close lattice match and providing an ideal crystallographic stacking template, but it also has a tendency to decompose at high temperatures.

2.4.5 Techniques for free-standing GaN substrates

The best quality films grown on SiC or sapphire still contain as many as 10^8 cm^{-2} dislocations. Perhaps surprisingly, these defects have not fatally impaired device operation. In fact, continuous wave edge emitting lasers have been fabricated by Nichia using material containing as high as 10^{10} cm^{-2} dislocations [35]. But while the dislocations do not appear to be device killers, there have been observations of maleficent effects of dislocations in several circumstances. Firstly, dislocations appear to be leakage pathways that increase the reverse saturation current of *p-n* and Schottky diodes [36]. Secondly, there is some evidence that dislocations may act as non-radiative recombination centers (see section 5.6.3). Thirdly, for FETs and other devices in which current transport is not along the (0001) direction, the threading dislocations have been shown to severely limit the electron mobility by scattering from charged electron traps at edge dislocations [37, 38].

For these reasons and others it is evident that free-standing, defect free GaN substrates are still very desirable. Free-standing substrates would also allow electrical back contacting, which would significantly simplify the processing requirements of many devices, and would drastically improve performance of nitride power devices

such as thyristors, bipolar transistors, and diode rectifiers (see chapter 5). Free-standing substrates could also better take advantage of the high thermal conductivity of GaN (as, *e.g.*, compared to a sapphire substrate) for more efficient power dissipation and cooling of devices, particularly lasers and power devices. While bulk GaN crystals grown by high pressure melt (or other means) are still under development, several alternative techniques for production of free-standing substrates have come to light in the interim. These techniques involve the growth of a thick heteroepitaxial layer, approximately 200-300 μm thick, followed by removal of the original host substrate. Nakamura has recently reported long lifetime lasers grown on free-standing GaN substrates which were grown by HVPE on sapphire substrates, the sapphire being removed subsequent to HVPE growth by chemomechanical polishing [18]. Growth of HVPE GaN layers on Si substrates, followed by removal of the Si at growth temperature, is also under development by Kuech, *et al.*, at the University of Wisconsin, Madison and at Advanced Technology Materials, Inc. (ATMI). ATMI has also demonstrated a GaN substrate which was removed from a sapphire wafer by a technique involving exposing the back side of the sample to excimer laser pulses. The energy of the laser pulses ($E_{g,GaN} < h\nu_{laser} < E_{g,sapphire}$) is absorbed by the GaN near the sapphire/GaN interface, dissociating the GaN and detaching the film [39].

2.5 Nitride crystallography

2.5.1 Polarity

Many issues discussed in part I of this thesis could benefit from a brief recounting of the crystallography of the wurtzite and zinc blende crystal structures. Specifically, the issue of polarity bears strongly on many aspects of the study of the III-nitrides, from growth to device design to film characterization [40, 41]. Just as the zinc blende III-V semiconductors such as GaAs have a distinct (111)A face (Ga-face) and a $(\bar{1}\bar{1}\bar{1})$B face (As-face), so does GaN in the wurtzite structure have a corresponding (0001) Ga-face and $(000\bar{1})$ N-face. Convention has taken the (0001) direction in GaN to

be the direction pointing from a Ga atom to its nearest neighbor N atom along the bond perpendicular to the wurtzite basal plane, as shown in Figure 2.2. It is stressed that crystal polarity is a bulk property, independent of surface atomic termination. In fact, it has been shown that the surfaces of both polarities are likely Ga-terminated [42]. Wurtzite GaN has been predicted to have a strong spontaneous electric polarization on the order of several MV/cm, along with large piezo-electric coefficients from which moderate strain can induce polarization fields of the same magnitude [43, 44]. There are significant effects of film polarity (Ga-face or N-face) on growth mode (see chapter 3), while polarity-dependent stark shifts affect quantum well light emitters [45]. Polarity and polarization effects are indeed the basis for high performance HFETs [26, 46] which utilize the high mobility of a two-dimensional electron gas which is induced by the strong piezo-electric field at the interface between GaN and a strained $Al_xGa_{1-x}N$ layer. It is therefore crucial to have knowledge and control of the III-nitride film polarity.

2.5.2 Polytypes

The most stable form of GaN, AlN, and InN is the wurtzite crystal structure, although the metastable zinc blende polytype can also be grown. Total internal energy differences between the two polytypes are not very large [47], which indicates that the zinc blende phase is not unstable. On the other hand, this low energy difference means that stacking faults may be more easily formed. In fact, stacking faults are believed to play a significant role in the nucleation and initial growth of GaN on sapphire by MOCVD [48]. There are some differences in the material properties of the zinc blende and wurtzite polytypes, for instance, the band gap of zinc blende GaN is slightly smaller than that of wurtzite. But this thesis deals entirely with the wurtzite form of GaN, so no further details concerning zinc blende GaN are included.

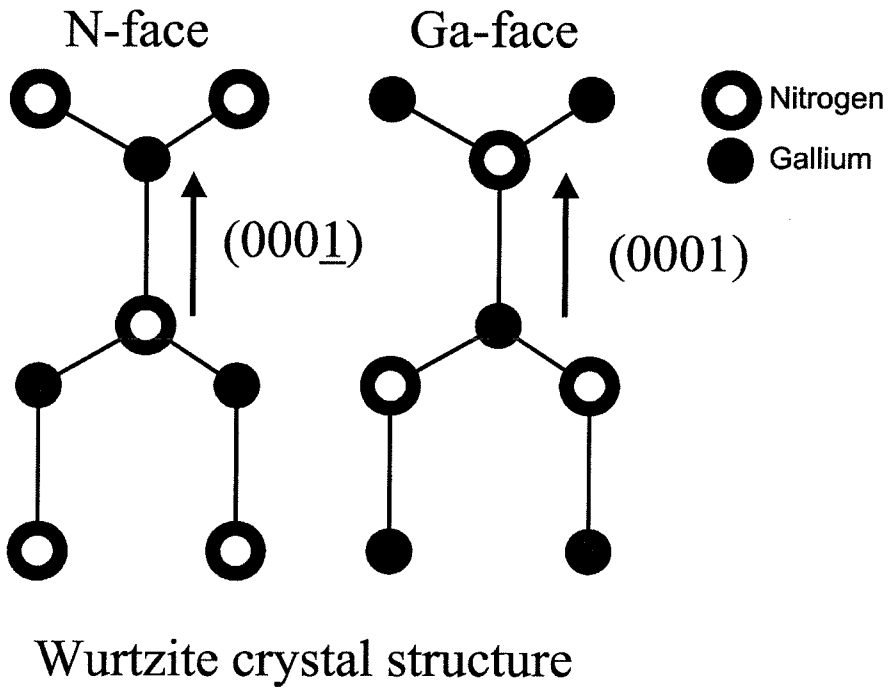

Figure 2.2: This diagram shows the difference between the Ga-face (0001) and N-face ($000\bar{1}$) polar orientations for wurtzite GaN. Polarity is critical in growth of GaN as well as device design due to the large spontaneous and piezo-electric polarization fields to which the polarity gives rise.

2.6 Nitrogen delivery

In the growth of III-nitrides, a means for making nitrogen available for reaction and bonding at the growth front has had to be developed. Vapor transport growth methods have traditionally used ammonia (NH_3), for nitrogen delivery, in which case it is thermally cracked at the surface. For physical deposition methods such as MBE, the issue of nitrogen delivery is quite important, as no solid or liquid source for nitrogen is available. Modifications to the growth technique to incorporate ammonia gas or plasma-cracked N_2 gas have had to be made. More details concerning nitrogen delivery issues are discussed in section 3.3.3.

2.7 Doping

To fabricate many electronic devices in the nitrides, both n- and p-type doping have to be available. n-type doping of GaN is rather easily accomplished as the material already has a strong tendency to be intrinsically n-type. Because of this tendency, the major emphasis has been in reduction of the background electron concentration when semi-insulating or p-type material is called for. Doping for p-type conduction has always been one of the challenges of the GaN system. A major breakthrough was made in the study of GaN when Akasaki discovered how to produce high conductivity p-GaN by low energy electron bombardment irradiation (LEEBI) [12]. Subsequent studies have shed some light on acceptor doping of GaN with magnesium, including the realization that hydrogen efficiently compensates the substitutional Mg, forming neutral H-Mg centers [13]. The passivating hydrogen can be removed from the acceptor complex by post-annealing in a hydrogen-free environment. Even non-compensated Mg-doped GaN is made difficult by the relatively deep level of the Mg acceptor ($\sim$ 200meV), which results in the free hole concentration being one to two orders of magnitude lower than the active acceptor concentration at room temperature. (See section 3.6.2.)

2.8 Defects in GaN

Since GaN is most often grown heteroepitaxially, with a large lattice mismatch between substrate and film, the extended defect structure [49] will depend on this mismatch and the number of defects be limited by it. The interface energy of a strained mismatched interface can in general be lowered by the generation of misfit dislocations. A simplistic estimate of the density of misfit dislocations is of the order $(f/a)^2$ where f is the mismatch and a is the lattice parameter. This formula predicts defect densities as high as 10^{13} cm^{-2} might occur in the worst case. Using unoptimized low temperature AlN or GaN buffer layers, the density of dislocations is typically $10^{10} - 10^{11}$ cm^{-2} in a GaN film on sapphire, which is still quite high. Unlike in zinc blende crystals, the dislocations in wurtzite GaN have a tendency to thread along the growth direction and do not experience a strong attraction to move toward each other and annihilate. Only after growth of large thicknesses ($> 20\,\mu$m) is significant defect reduction seen [50].

The threading dislocations can cause significant degradations in material quality, especially in transport and luminescent properties. Rosner, *et al.*, have observed by cathodoluminescence imaging that dislocations can be non-radiative recombination sites [51]. Dislocations have also been shown to be leakage pathways, shorting reverse bias devices [36]. But perhaps the area in which the dislocations most make their presence known is in the reduction of carrier mobility by scattering from charged traps at dislocations [37, 38].

In order to further reduce the density of extended defects, deliberate manipulation of the propagation of the dislocations must be accomplished, forcing them to annihilate in the early stages of film growth by control of the film morphology evolution.

2.8.1 Methods of defect reduction

The optimized process for MOCVD growth of GaN on sapphire involves the coalescence of micron-scale islands. The substrate nitridation and buffer layer thickness are optimized such that upon commencement of growth, a specific density of islands

nucleate and grow, likely by the spiral growth mechanism. After these islands are about 1 μm high, they grow laterally and coalesce, resulting in a flat film surface. It is in the lateral growth step that the dislocations are forced to bend sideways and meet with each other at the island boundaries. Using optimized conditions, dislocation densities as low as $2 \cdot 10^8$ cm^{-2} have been grown by this evolutionary process [25]. Another more recent technique for reduction of defect density is the lateral epitaxial overgrowth technique [52, 53], where GaN selectively over grows a SiO_2 or SiN mask. The mask blocks threading dislocations from propagating through from below.

In the case of HVPE, the high growth rate capability allows defect reduction through the growth of very thick layers. After approximately 200 μm of growth, defect densities have been observed to be reduced to the order of 10^7 cm^{-2} [50].

There have been several reports of MBE-grown GaN films with dislocation densities in the 10^9 range, but in general neither the morphological evolution control or ultra-high growth rate capability are available for MBE growth. In chapter 4 some possibilities are proposed and some techniques presented for defect reduction in GaN by MBE.

Bibliography

[1] C. I. Wu, A. Kahn, and E. S. Hellman, *Appl. Phys. Lett.* **73**(10) 1346 (1998).

[2] R. J. Nemanich, P. K. Baumann, M. C. Benjamin, S. W. King, J. vanderWeide, and R. F. Davis, *Diam. Relat. Mater.***5**, 790 (1996).

[3] J. O. McCaldin, M. W. Wang, and T. C. McGill, *J. Cryst. Growth* **159**, 502 (1996).

[4] S. Strite, M. E. Lin, and H. Morkoç, *Thin Solid Films* **231**,197 (1993).

[5] H. P. Maruska and J. J. Tietjen, *Appl. Phys. Lett.* **15**, 367 (1969).

[6] S. Porowski, *MRS Internet J. Nitride Semicond. Res.* **4S1**, G3.10 (1999).

[7] Y. A. Vodakov, E. N. Mokhov, M. G. Ramm, M. S. Ramm, A. D. Roenkov, A. G. Ostroumov, A. A. Wolfson, S. Y. Karpov, Y. N. Makarov, and H. Jurgensen, *Mat. Res. Soc. Symp. Proc.* **482**, 27 (1998).

[8] N. R. Perkins, M. N. Horton, and T. F. Kuech, *Mat. Res. Soc. Symp. Proc.* **395**, 243 (1995).

[9] R. D. Vispute, V. Talyansky, R. P. Sharma, S. Choopun, M. Downes, T. Venkatesan, K. A. Jones, A. A. Iliadis, M. A. Khan, and J. W. Yang, *Appl. Phys. Lett.* **71**, 102 (1997).

[10] N. Grandjean, J. Massies, P. Vennegues, M. Leroux, F. Demangeot, M. Renucci, and J. Frandon, *J. Appl. Phys.* **83**, 1379 (1998).

[11] M. Yoshimoto, A. Hatanaka, H. Itoh, and H. Matsunami, *J. Cryst. Growth* **188**, 92 (1998).

[12] H. Amano, M. Kitoh, K. Hiramatsu, N. Sawaki, and I. Akasaki, *Jpn. J. Appl. Phys. Pt. 2* **28**, L2112 (1989).

[13] S. Nakamura, N. Iwasa, M. Senoh, and T. Mukai, *Jpn. J. Appl. Phys.* **31**, 1258 (1992).

[14] S. Nakamura, M. Senoh, N. Iwasa, S. Nagahama, T. Yamada, and T. Mukai, *Jpn. J. Appl. Phys. Pt. 2* **34**, L1332 (1995).

[15] S. Nakamura, N. Senoh, N. Iwasa, and S. Nagahama, *Jpn. J. Appl. Phys. Pt. 2* **34**, L797 (1995).

[16] S. Nakamura, *J. Cryst. Growth* **195**, 242 (1998).

[17] S. Nakamura, *Mat. Res. Soc. Symp. Proc.* **482**, 1145 (1998).

[18] S. Nakamura, M. Senoh, S. Nagahama, N. Iwasa, T. Yamada, T. Matsushita, H. Kiyoku, Y. Sugimoto, T. Kozaki, H. Umemoto, M. Sano, and K. Chocho, *Appl. Phys. Lett.* **73**, 832 (1998).

[19] S. Nakamura and G. Fasol, *The Blue Laser Diode* (Springer, Berlin, 1997).

[20] R. Zhang, L. Zhang, D. M. Hansen, M. P. Boleslowski, K. L. Chen. D. Q. Lu, B. Shen, Y. D. Zheng, and T. F. Kuech, *MRS Internet J. Nitride Semicond. Res.* **4S1**, G4.7 (1999).

[21] D. J. Smith, S. C. Y. Tsen, B. N. Sverdlov, G. Martin, and H. Morkoç, *Solid–State Electron.* **41**, 349 (1997).

[22] J. E. Northrup, J. Neugebauer, and L. T. Romano, *Phys. Rev. Lett.* **77**, 103 (1996).

[23] R. C. Glass, D. Henshall, V. F. Tsvetkov, and C. H. Carter, *Phys. Stat. Solid. (B)* **202**, 149 (1997).

[24] *Properties of Sapphire*, Union Carbide Crystal Products, Washougal, WA (1993).

[25] X. H. Wu, P. Fini, E. J. Tarsa, B. Heying, S. Keller, U. K. Mishra, S. P. DenBaars, and J. S. Speck, *J. Cryst. Growth* **190**, 231 (1998).

[26] M. J. Murphy, B. E. Foutz, K. Chu, H. Wu, W. Yeo, W. J. Schaff, O. Ambacher, L. F. Eastman, T. J. Eustis, R. Dmitrov, M. Stutzmann, and W. Rieger *MRS Internet J. Nitride Semicond. Res.* **4S1**, G8.4 (1999).

[27] Z.Z. Bandić, P.M. Bridger, E.C. Piquette, and T.C. McGill, *Appl. Phys. Lett.* **74**(9), 1266 (1999).

[28] Z. Z. Bandić, R. J. Hauenstein, M. L. O'Steen, and T. C. McGill, *Appl. Phys. Lett.* **68**, 1510 (1996).

[29] A. Strittmatter, A. Krost, M. Strassburg, V. Turck, D. Bimberg, J. Blasing, and J. Christen, *Appl. Phys. Lett.* **74**, 1242 (1999).

[30] A. Kuramata, K. Horino, K. Domen, K. Shinohara, and T. Tanahashi, *Appl. Phys. Lett.* **67**, 2521 (1995).

[31] W. A. Doolittle, T. Kropewnicki, C. Carter-Coman, S. Stock, P. Kohl, N. M. Jokerst, R. A. Metzger, S. Kang, KI. Lee, G. May, and A. S. Brown, *Mat. Res. Soc. Symp. Proc.* **482**, 283 (1998).

[32] E. S. Hellman, Z. Lilienthal-Weber, and D. N. E. Buchanan, *MRS Internet J. Nitride Semicond. Res.* **2**, 30 (1997).

[33] P. Kung, A. Saxler, X. Zhang, D. Walker, R. Lavado, and M. Razeghi, *Appl. Phys. Lett.* **69**, 2116 (1996).

[34] C. Fechtmann, V. Kirchner, S. Einfeldt, H. Heinke, D. Hommel, T. Lukasiewicz, Z. Luczynski, and J. Baranowski, *Mat. Res. Soc. Symp. Proc.* **482**, 295 (1998).

[35] S. Nakamura, at the fall meeting of the Materials Research Society, Boston, MA, December (1997).

[36] P. Kozodoy, J. P. Ibbetson, H. Marchand, P. T. Fini, S. Keller, J. S. Speck, S. P. DenBaars, and U. K. Mishra, *Appl. Phys. Lett.* **73**(7), 975 (1998).

[37] H. M. Ng, D. Doppalapudi, T. D. Moustakas, N. G. Weimann, and L. F. Eastman, *Appl. Phys. Lett.* **73**, 821 (1998).

[38] N. G. Weimann, L. F. Eastman, D. Doppalapudi, H. M. Ng, T. D. Moustakas, *J. Appl. Phys.* **83**, 3656 (1998).

[39] R. P. Vaudo, V. M. Phanse, M. C. Cattrel, and J. M. Redwing, presented at the meeting of the Electrochemical Society, Boston, MA, November 1998.

[40] For a more detailed description of GaN crystal polarity, see for example, J. L. Rouviere, J. L. Weyher, M. Seelmann-Eggebert, and S. Porowski, *Appl. Phys. Lett.* **73**, 668 (1998).

[41] E. S. Hellman, *MRS Internet J. Nitride Semicond. Res.* **3**, 11 (1998).

[42] A. R. Smith, R. M. Feenstra, D. W. Greve, M. S. Shin, M. Skowronski, J. Neugebauer, and J. E. Northrup, *J. Vac. Sci. Technol. B* **16**, 2242 (1998).

[43] J. A. Majewski, G. Zandler, and P. Vogl, *Semicond. Sci. Technol.* **13**, A90, Suppl. S Aug. (1998).

[44] M. S. Shur, A. d. Bykhovski, and R. Gaska, *MRS Internet J. Nitride Semicond. Res.* **4S1**, G1.6 (1999).

[45] A. Hangleiter, J. S. Im, H. Kollmer, S. Heppel, J. Off, and F. Scholz, *MRS Internet J. Nitride Semicond. Res.* **3**, 15 (1998).

[46] E. T. Yu, X. Z. Dang, L. S. Yu, D. Qiao, P. M. Asbeck, S. S. Lau, G. J. Sullivan, K. S. Boutros, and J. M. Redwing, *Appl. Phys. Lett.* **73**, 1880 (1998).

[47] Z.Z. Bandic, T.C. McGill, and Z. Ikonic, *Phys. Rev. B* **56**, 3564 (1997).

[48] A. Munkholm, C. Thompson, C. M. Foster, J. A. Eastman, O. Auciello, G. B. Stephenson, P. Fini, S. P. DenBaars, and J. S. Speck, *Appl. Phys. Lett.* **72**, 2972 (1998).

[49] X. H. Wu, L. M. Brown, D. Kapolnek, S. Keller, B. Keller, S. P. DenBaars, and J. S. Speck, *J. Appl. Phys.* **80**(6), 3228 (1996).

[50] R. P. Vaudo, V. M. Phanse, M. C. Cattrel, and J. M. Redwing, 2nd International Conference on Nitride Semiconductors, Tokushima, Japan, 25-31 October 1997.

[51] S. J. Rosner, E. C. Carr, M. J. Ludowise, G. Girolami, and H. I. Erikson, *Appl. Phys. Lett.* **70**, 420 (1997).

[52] D. Kapolnek, S. Keller, R. Vetury, R. D. Underwood, P. Kozodoy, S. P. Den Baars, and U. K. Mishra, Appl. Phys. Lett. **71**, 1204 (1997).

[53] T. S. Zheleva, S. A. Smith, D. B. Thomson, T. Gehrke, K. J. Linthicum, P. Rajagopal, E. Carlson, W. M. Ashmawi, and R. F. Davis, *MRS Internet J. Nitride Semicond. Res.* **4S1**, G3.38 (1999).

Chapter 3 Molecular Beam Epitaxial Growth of Gallium Nitride, Aluminum Nitride, and Alloys

3.1 Introduction

For the past several decades the molecular beam epitaxy (MBE) technique has been used successfully for the growth of thin epitaxial films [1]. MBE has been used to grow a wide variety of materials, including semiconductors, metals, and superconductors. For many applications it is the deposition technique of choice, competitive with other growth methods such as vapor phase and liquid phase epitaxy. There has been considerable work done in the MBE growth of IV/IV, III/V and II/VI semiconductors for applications ranging from VCSELs to photodetectors, and adding in no small way to our understanding of these materials. MBE is a very valuable tool in the research of thin films due to the relatively large number of *in situ* characterization and real-time diagnostic techniques that are available, such as desorption mass spectroscopy (DMS) [2], ellipsometry [3], and a variety of electron diffraction techniques including LEED, RHEED, and HREELS [4]. Most of these *in situ* characterization methods are available because of the high (and ultrahigh) vacuum environment in which growth takes place.

During the surge of attention that has been focused towards GaN beginning in the early 1990s, there has been considerable interest in the growth of the group III-nitrides by MBE [5, 6]. MBE has also been successfully used for growth of GaN-based light emitting diodes [7, 8, 9, 10] and field effect transistors [11].

3.2 Comparison of growth techniques for nitrides

The nitride materials system is significantly different in a variety of ways from the compounds which have been more commonly grown by MBE, so special considerations have had to be made to overcome these differences. Several methods have been reported for growth of GaN, including MOCVD, HVPE, sublimation, MBE, and high pressure bulk growth from the melt.

3.2.1 Bulk growth

Ideally, one would like to have large boules of single crystal GaN and AlN from which substrates could be cut and on which devices could be epitaxially grown. However, bulk growth of GaN is tremendously difficult due to the high pressures and temperatures required [12, 13]. Using N_2 gas dissolved in Ga liquid at a pressure of 20 kbar and at 1900°C, some small bulk crystals have been produced ($\sim$ 100 mm^2). These crystals are plate-like, and have a very large background donor concentration ($\sim 3 \cdot 10^{19}$ cm^{-3}) unless Mg is added to the melt, in which case they can be made highly resistive [14]. Large bulk GaN crystals seem to be a thing of the future. In the absence of which, one is left with vapor phase heteroepitaxy or other techniques such as MBE.

3.2.2 MOCVD

By far the majority of nitride growth research in recent years has been by the MOCVD technique [15, 16]. This is not surprising, considering the rapid advances in GaN-based LEDs and laser diodes by S. Nakamura and Nichia Chemical Industries of Japan [17]. There has been a large effort in the United States to develop our own nitride laser technology, following Nichia, but to date no continuous wave nitride lasers have been produced in this country that operate at room temperature. The MOCVD growth of GaN has advanced considerably as a result of the quest for the UV GaN/InGaN laser. Many thousands of GaN films have been grown on various substrates at companies

and universities in the past five years, and the growth recipe and procedure have been optimized to a large degree. There have been extensive studies of the various stages of MOCVD growth, including substrate cleaning and nitridation [18, 19, 20], buffer layer optimization [21], growth temperature and pressure [22], and gas flow ratio [23].

All this attention to MOCVD has not been fruitless, as the method has shown its advantages in the growth of (relatively) high quality material. MOCVD benefits from a relatively high growth rate capability for GaN, typically $2-5\,\mu$m per hour, as well as provides a good deal of control of the morphology evolution during growth. The control of morphology evolution can be used to reduce extended defect density by up to a factor of 100 via the lateral coalescence of micron-scale islands [24] or perhaps even more by the lateral epitaxial overgrowth (LEO) technique [25, 26]. There have also been many reports on both n and p-type doping of GaN by MOCVD as well as growth of $In_xGa_{1-x}N$ and $Al_xGa_{1-x}N$ alloys.

Although MOCVD has been perhaps the most successful way of growing GaN, the technique does have several disadvantages. The high growth temperature, usually around 1050°C, presents several problems. There is difficulty in the incorporation of high vapor pressure elements such as indium and magnesium (acceptor) at this temperature. Doping profiles between n- and p-type layers tend to be smeared out due to the resistance of Mg to incorporate [27] and to Mg diffusion. The high growth temperature also aggravates strain effects due to differences in thermal expansion coefficient between the epilayer and substrate. Additionally, magnesium doped films must be post annealed to achieve p-type conductivity, since hydrogen, which is present in the reactor, is an efficient compensator of Mg acceptor centers in GaN [28]. MOCVD also has difficulties with aluminum containing compounds because of premature reactions between the ammonia and metalorganic aluminum precursor, usually trimethyl-aluminum (TMA) or triethyl-aluminum (TEA). The pre-reaction results in "AlN dust" which falls to the bottom of the reactor before reaching the substrate, drastically reducing growth rate of AlN or $Al_xGa_{1-x}N$ layers.

3.2.3 HVPE

Another promising technique for growth of III-nitride layers is hydride (or halide) vapor phase epitaxy (HVPE). In this method, the nitrogen precursor is ammonia, but the group III metal is transported to the substrate by passing HCl gas over a hot receptacle of, *e.g.*, gallium and forming $GaCl_3$ gas which then reacts with NH_3 at the growth surface. The source materials are available in high purity, and are relatively inexpensive compared to the metalorganics used in MOCVD. One of the appealing features of the HVPE method is that it allows very high growth rates, over 200 μm per hour for GaN. For this reason it is a prime candidate for growth of thick layers, which might be used as high voltage stand-off regions in high power devices [29], or might be converted to free standing substrates. Thick HVPE films have among the lowest dislocation densities, typically 10^7 cm^{-2} [30]. HVPE has also been used in the growth of LEO structures [31]. Disadvantages with the HVPE method are in p-type doping and with reactivity of $AlCl_3$ with quartz reactor chamber walls.

3.2.4 MBE

Molecular beam epitaxy has received relatively less attention than have MOCVD and HVPE, and for this reason among others GaN material quality has lagged somewhat behind. Depending on the source for nitrogen, GaN growth rates have (until recently, see section 3.3.4) been relatively slow in comparison with MOCVD, typically 0.2-1.0 μm per hour. MBE has also had a more limited investigation into the optimization of growth on mismatched substrates such as c-plane sapphire (Al_2O_3), SiC, and GaAs. Nevertheless, material quality of films grown by MBE can be nearly equal to the best grown by MOCVD [32] and devices made from MBE-grown layers can perform on par with MOCVD-grown devices [33]. An advantage of MBE is the relatively lower growth temperature ($650 - 800$°C), which is more amiable to incorporation of the high vapor pressure elements In and Mg and also should result in less thermal stress. This also allows more abrupt p-n junctions. Other advantages of MBE include the absence of carbon and hydrogen in the growth environment, hydrogen being a

compensator of Mg acceptors – the result is p-type films that do not require post-annealing activation. Also MBE, unlike MOCVD, has no fundamental problems with the growth of Al-containing compounds. Some of the stated advantages of MBE can also at times be disadvantages, however. For example, since MBE growth occurs far from thermodynamic equilibrium, one cannot take advantage of effects that happen near equilibrium, like the high differentials in growth rate for different crystal directions which are used in lateral epitaxial overgrowth [25]. The lack of hydrogen allows as-grown p-type films, but hydrogen also increases the solubility of Mg in GaN [34] and provides beneficial surface termination which can lead to higher growth rate [35] and a lower surface energy.

3.3 Our MBE machine

3.3.1 Transfer tube cluster system

The III-nitride MBE system used in this study is connected as part of a large cluster of growth and analysis chambers. Four MBE growth chambers, including dedicated chambers for III-nitride, II-VI, Si-Ge, and III-As/Sb materials, are interconnected via UHV transfer tube, as shown in Figure 3.1. There are also three sample introduction load locks, several sample-heating and cleaning stages, an e-beam vacuum metalization station, and an x-ray photoemission spectroscopy (XPS) analysis chamber. All these systems share common sample handling protocol (Perkin-Elmer), so a sample can be moved from any one chamber into any other. This is very useful for the nearly unlimited possible combinations of heteroepitaxy, while the XPS system provides invaluable information on fresh-grown surfaces that have not yet been contaminated by exposure to atmosphere. The XPS analysis has been heavily used in the past for measurement of heterojunction band offsets [36].

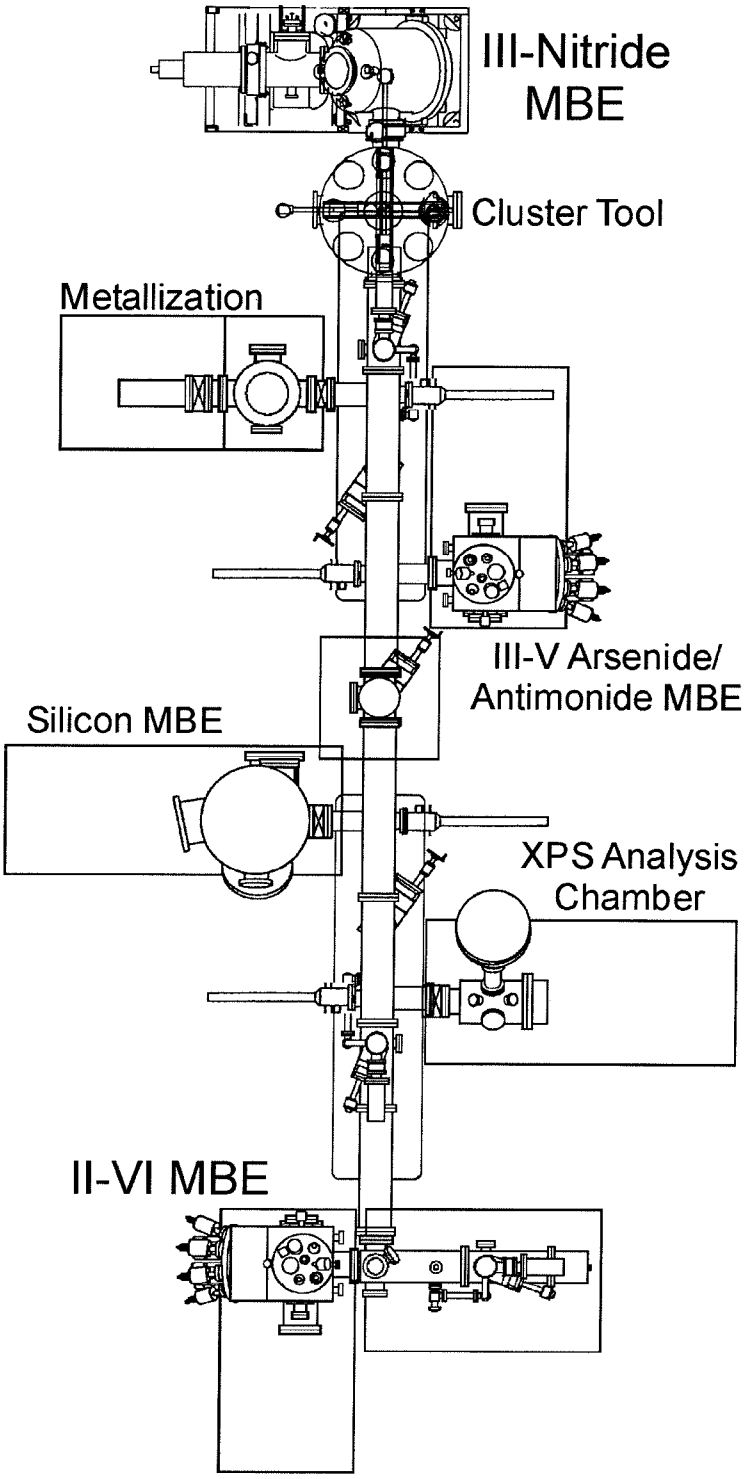

Figure 3.1: The MBE chamber used for this work is part of a large system of growth and analysis chambers. Four MBE growth chambers (III-N, III-As/Sb, IV-IV, II-VI) as well as metalization and ESCA/XPS/Auger analysis chambers, load-lock and sample preparation chambers are all connected via ultra-high vacuum (UHV) transfer tube.

3.3.2 Sources for group III materials and dopants

A schematic diagram of the III-nitride MBE system is shown in Figure 3.2. The effusion cells used for gallium and indium are dual filament cells. These ovens have two separate temperature zones, one near the crucible lip and one main zone for heating the bulk of the loaded material. For Ga and In, the lip is typically heated to a somewhat higher temperature (usually $20 - 40°C$ higher) in order to prevent any condensation of Ga or In metal at the lip of the crucible, which can cause "spitting" from the cell, which has been ascribed as a cause of oval defects in III-Vs [37].

Unlike the sources used for the group III elements Ga and In, the effusion cell for aluminum is a "cold lip" cell. In this case, the outer lip of the cell is kept cooler than the main bulk of the cell in order to reduce or prevent aluminum creep. At high temperatures, aluminum wets the PBN crucible walls and has a tendency to creep up and out of the crucible by capillary action, around to the back where it can short out the heater filament or cause other damage to the source cell. The cold lip cell is effective in combination with keeping a group V overpressure in the chamber. The group V overpressure (in this case the nitrogen plasma) bonds with the creeping aluminum to form a solid compound (in this case AlN) and prevents aluminum from reaching the rear of the PBN.

Due to the very low vapor pressure of silicon, its effusion cell is specially designed to be capable of reaching high temperatures. Typical silicon cell temperatures during growth can range from 1200°C to 1400°C. The magnesium dopant source uses a standard 16cc effusion cell.

3.3.3 Specific customizations for nitride growth

While MBE usually uses condensed phase (solid or liquid) elemental or compound source materials, there is no such available for nitrogen. Elemental nitrogen N_2 is effectively inert and useless as a source component. The delivery of an *active* nitrogen component beam is thus a primary issue. Several different methods have been employed in the delivery of active nitrogen species to the substrate, all of which are

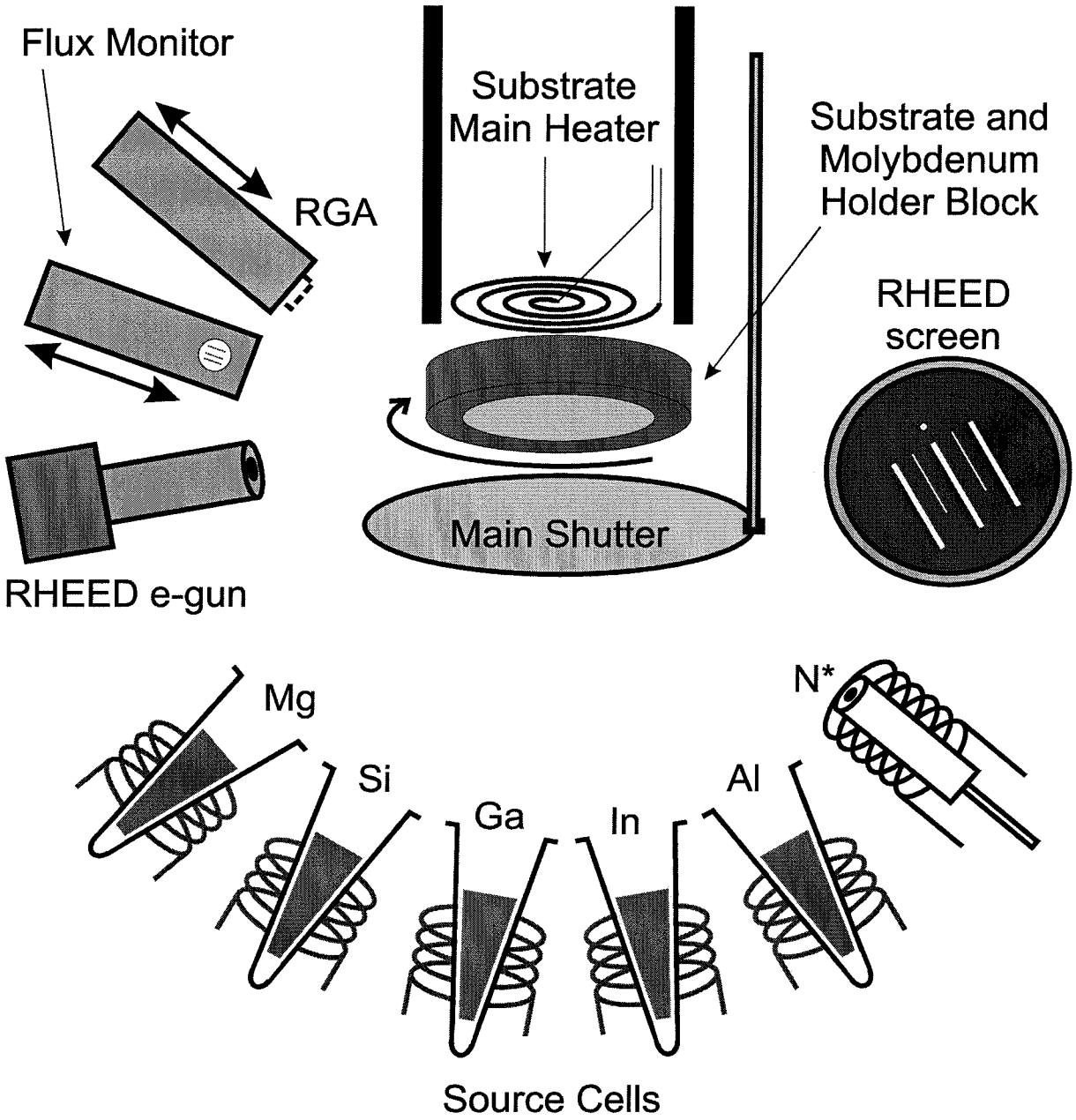

Figure 3.2: Shown is a schematic diagram of the SVT Associates N35 MBE growth chamber for III-nitrides. The system is equipped with a number of especially useful features as described in the text, including the following: a specially designed RF nitrogen source, dual filament cells for Ga and In, cold lip cell for Al, high temperature cell for Si; specially shaped close-fitting linear action shutters including main shutter; mass spectrometer and flux monitor ionization gauge which are both translatable into the focus of the source beams; RHEED electron gun and phosphor screen; high temperature substrate heater and non-bonded holder block.

based on nitrogen-containing gasses.

One source of active nitrogen is ammonia (NH_3) gas. MBE growth using ammonia is sometimes referred to as ammonia MBE or gas source MBE (GSMBE) [38]. In this case the ammonia is cracked at the substrate surface. Ammonia MBE requires substrate temperatures of approximately 900°C and background pressures of greater than 10^{-4} torr, but can achieve growth rates of $1-2\,\mu$m per hour [38]. Other reactive nitrogen-containing gases have also been tried, such as azides and hydrazine [39], but it is not clear that their use offers any advantage over ammonia, and the azides can provide a greater safety risk as they are explosive.

Another method of active nitrogen delivery is by a nitrogen plasma source. The most common of these are electron cyclotron resonance (ECR) plasma sources and radio frequency (RF) plasma sources. Early versions of the plasma sources were highly inefficient, resulting in only about one percent activation in the nitrogen beam, and limiting growth rate to 0.1 to $1.0\,\mu$m per hour at a system pressure of typically 10^{-5} to 10^{-4} torr.

At the high background pressures required by the nitrogen beam, special care must be taken to extend the lifetime of all hot filaments in the MBE system, particularly the substrate heater, the source oven filaments and the RHEED gun filament. Filament life is especially shortened by the presence of ammonia. An issue exacerbating the issue of filament life is the rather high substrate temperature required for GaN growth, typically 800°C for GaN to over 1000°C for $Al_xGa_{1-x}N$. At these temperatures, most heating is radiative and indium substrate mounting becomes problematic, making non-bonded substrate holders required for best performance.

3.3.4 RF plasma nitrogen delivery

Two types of plasma sources have been used for growth of nitrides and for p-type doping of II-VI compounds [40], electron cyclotron resonance (ECR) sources [41] and radio frequency plasma sources [9, 42]. High quality material has been produced with both types of sources. The work presented in this chapter was carried out using a RF

plasma source from SVT Associates of Eden Prairie, MN.

The source operates by releasing high purity filtered N_2 into the source through a precision leak valve, where it enters the pyrolytic boron nitride (PBN) plasma chamber and is excited by a water cooled coil. Radio frequency power is applied to the coil at 13.56 MHz and at a forward power level of 200 to 600 W. The excited nitrogen species exit the plasma chamber through an aperture plate which is directed toward the substrate. The particular geometry as well as number and area of the holes in the aperture plate strongly influences the character and number of excited species produced by the source for growth. Aperture plates with anywhere from one to 400 holes have been used by other researchers [43] while for these studies a single hole aperture of 3 mm^2 area was used.

Until recently, commercial RF plasma sources have been rather inefficient, producing beams with typically only $1-2\%$ of the nitrogen gas throughput being incorporated into the nitride film. Using these sources requires large flow rates of N_2 resulting in high chamber background pressures during growth, up to 10^{-4} torr. The inefficiency also places a limit on the maximum growth rate attainable, since at sufficiently high flow rates, the plasma becomes unstable and is extinguished. Older source designs, such as the Oxford Applied Research (OAR) MPD21 (which was designed as a II-VI doping source), are limited to $0.1-0.2\,\mu$m per hour. Newer designs have become more efficient, such as the EPI Unibulb (EPI Vacuum Products, St. Paul, MN), which can attain rates of $1-2\,\mu$m per hour. The SVT Associates source used here is capable of $1-1.5\,\mu$m per hour growth rate, but a lower rate of $0.4\,\mu$m per hour was typically used in favor of a lower system pressure. In recent months, even higher efficiencies have been attained (up to 45% effective efficiency), and growth rates of up to $6\,\mu$m per hour demonstrated by an upgraded version of the SVT Associates source [44].

The radio frequency sources produce a number of active species, including ionized and neutral atomic N, as well as ionized and excited metastable N_2. The particular species that takes place in the growth process is still being investigated. However, several tentative conclusions regarding the nitrogen species have been reached [43].

Firstly, no growth can be achieved using ground state molecular N_2. Secondly, high energy ions are considered to be damaging and undesirable during growth [45]. Thirdly, both the atomic and metastable excited molecular species are thought to significantly contribute to growth [43]. The specific roles and processes in growth involving these latter continue to be investigated and are at present not well understood.

Another issue pertinent to the use of nitrogen plasma sources which has not yet received much attention is the generation of boron. Secondary ion mass spectroscopy studies have shown that MBE-grown GaN films can contain anywhere from 10^{16} to 10^{19} incorporated B atoms cm^{-3} [43]. The origin of the boron is likely the PBN plasma chamber walls of the source, which can slowly be degraded by the highly reactive N* plasma. Boron can have malignant effects on film quality, so efforts should be taken to minimize the boron contamination. Reduction in plasma power may be effective in this regard, but changing the liner material from PBN to something else such as Al_2O_3 or quartz is no improvement since these chamber materials are known to give off contaminant oxygen, which is more deleterious.

3.3.5 Pumping

The pumping requirements for III-nitride MBE are basically similar to MBE of other materials. One difference is the increased N_2 gas load which is present for growth of nitrides. The MBE system used here is equipped with a CTI Cryogenics CT-8 cryopump and a 600 L/s ion pump, with a small turbo pump station for roughing. During growth, the gate valve to the ion pump is closed (and pressure interlocked) and the rather high throughput of N_2 gas is pumped by the cryopump. We have observed no problems with this setup, and the CT-8 has to be regenerated only after 6-9 months. The chamber is equipped with a spare port for additional pumping capacity, and a further reduction in growth pressure may be achieved by installation of another cryopump or a large turbo-molecular pump in this location.

3.3.6 *In situ* characterization and diagnostics

The MBE system is equipped with a number of *in situ* characterization tools which can be extremely useful in the study of nitride growth. Reflection high energy electron diffraction (RHEED) is carried out using a 10keV electron gun, built by SVT Associates, in combination with a large 8 inch phosphor screen. The RHEED images are captured directly to personal computer using a CCD camera and frame grabber board. Using the captured RHEED image, software analysis can provide a wealth of information, including measurement of the frequency of specular intensity oscillations for growth rate, the spacing of streaks for lattice constant measurement and determination of alloy fraction, as well as surface reconstruction and specular intensity as an indicator of surface stoichiometry.

The chamber is equipped with an ionization flux monitor, essential for calibration of the beam fluxes, which is linearly translatable on a bellows for positioning at the substrate location (see Figure 3.2). A residual gas analyzer is also mounted on a translatable bellows for mass spectroscopy of both background partial pressures and quantitative measurement of the beam constituents and ratios. The system is also equipped with ports for *in situ* ellipsometry and *in situ* cathodoluminescence, which can be added at a later date. The chamber also is equipped with ports for atomic absorption flux measurements as well as a large 6 inch port in the center of the source flange for line-of-sight characterization techniques such as laser reflectivity (normal incidence) for measurements of growth rate and surface flatness or an etalon assembly similar to that of Reference [46] for measurement of residual strain.

3.3.7 Sample heating

Due to the somewhat higher than normal substrate temperatures required for growth of GaN and $Al_xGa_{1-x}N$, a specially designed substrate heater was installed. The heater is based on a specially shaped graphite filament, and is specified to reach sample temperatures of up to 1200°C. The extra durability of the heater also helps to mitigate the effects of high background N_2 pressure during growth.

3.3.8 Substrate preparation, mounting and handling

In this chapter, results are presented for growth on c-plane (0001) sapphire substrates. The substrates are sourced from Union Carbide Crystal Products, are single side polished, and are 17 thousandths of an inch thick. An issue for consideration in MBE of GaN is how to mount the substrates. Traditionally, *e.g.*, for GaAs growth, the substrate is bonded to a molybdenum holder block using In. This method works well for substrate temperatures up to about 650°C, but at higher temperatures the indium begins to rapidly evaporate resulting in dropped samples and/or poor temperature uniformity where the indium metal is gone. An alternative is the use of non-bonded radiatively heated substrate holder blocks. In the non-bonded blocks, the substrate is held in place with refractory metal wire clips or springs and is heated directly by the black body radiation of the heater filament. In the case of sapphire substrates, however, radiative heating can be very inefficient because sapphire is non-absorptive in the visible and most of the infrared. To assist in the radiative heating of the substrates, they were back-side coated with molybdenum or titanium. In this case, the radiative heat is absorbed in the metal coating and transferred to the sapphire by thermal conduction.

The substrates were typically used directly as received from the manufacturer, as etching of substrates in acid solution seemed to make no noticeable difference. The 2 inch wafers, after metalization, were loosely mounted in a non-bonded holder block with suspended tantalum wires and loaded into the vacuum system.

3.4 Typical GaN growth procedure

In preparation for a typical growth, the chamber cryopanneling is first filled with liquid nitrogen (LN_2) and the ion pump isolation gate valve closed. The fresh substrate and block is then brought into the chamber and its temperature is ramped up at a rate of approximately 15-20°C per minute to 800-1000°C. The heating thermally cleans and outgasses the substrate. As the substrate is ramping up, the source cells are brought

from idle to the temperatures used for growth of the nucleation layer – for AlN buffers, the Al is set to approximately 1130°C while for GaN buffer layers the Ga cell is heated to a main thermocouple temperature of $\sim$ 850°C with the crucible lip approximately 20 degrees higher. The RF nitrogen source is turned on and set to 350 W, the N_2 gas flow slowly opened until the plasma ignites and then the flow is reduced to a corresponding chamber pressure of $\sim 5 \cdot 10^{-5}$ torr. Also at this time the RHEED gun filament is slowly ramped up to optimum operating current (approximately 2 Amps) and the RHEED image of the substrate is observed.

When the substrate and source cells reach their target temperatures, the main shutter is opened to expose the sapphire substrate to the nitrogen plasma. This is the nitridization stage, which varies in duration from 5-30 minutes. After nitridation, the RHEED pattern has brightened and become diffuse streaks corresponding in spacing and symmetry to those from an AlN surface. This can be taken as evidence of conversion of the top thin layer of Al_2O_3 to AlN or AlO_xN. After nitridation, the substrate temperature is ramped to the buffer layer deposition temperature, typically 650°C, but sometimes as high as 800°C. After sufficient time for temperatures to stabilize, the Ga or Al shutter is opened to start growth of the buffer layer. The specific III/V flux ratio is crucial in the deposition of the buffer layer, as will be seen in section 4.2.2. The typical deposition time for the buffer layer is two minutes, which was estimated to deposit approximately 20 nm based on measurements of film thickness for longer runs under the same conditions. Unfortunately, the thickness and deposition time of the buffer layers has not yet been fully optimized for our system. The 20 nm (approximate) thickness was chosen in compliance with other results from the literature.

After deposition of the buffer layer, the Ga cell temperature is raised to approximately 870°C for growth of the main layer. For Si doped n-type films, the Si cell temperature is raised to the desired doping level (see section 3.6.1), approximately 1250°C. Except for the growth of p-type GaN (section 3.6.2) the substrate temperature of the main layer is set to 800°C. The Ga cell shutter is then opened for growth of the main layer. The exact temperature of the Ga cell usually varies within a few

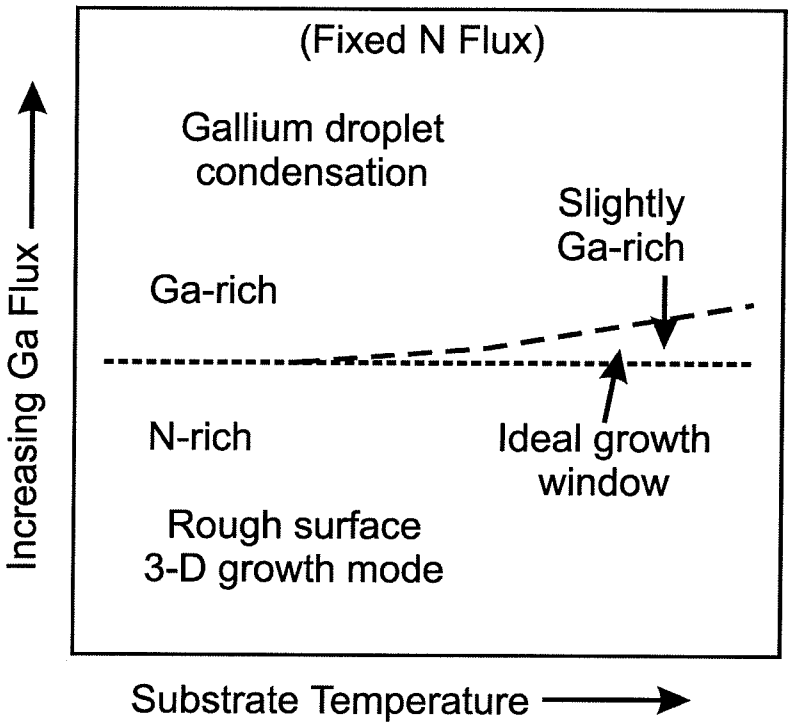

Figure 3.3: The optimal condition for RF-MBE growth of GaN is slightly Ga-rich. If the gallium flux is too low in relation to the effective arrival rate of nitrogen, growth proceeds in a 3-D mode resulting in a rough surface and poor structural quality. If the Ga flux is too high, metal droplets will build up on the surface. The window for slightly Ga-rich growth without condensation becomes wider for increased substrate temperatures, since the excess Ga can re-evaporate more readily from the surface.

degrees as RHEED is used to optimize the growth conditions, which are slightly Ga-rich (see chapter 4). If the Ga temperature is slightly too low, the RHEED image becomes spotty indicating surface roughening, while if the Ga temperature is too high, the RHEED image dims indicating Ga condensation on the film surface (see Figure 3.3). Growth of the main layer then proceeds for typically a number of hours, resulting in a $1-2\,\mu$m thick film. For AlN or $Al_xGa_{1-x}N$ films, the same basic procedure is followed, except that the Al shutter is open instead of or in addition to the Ga shutter.

3.4.1 RHEED Observations

The RHEED image abruptly transforms from spotty to streaky-like upon transition from effectively nitrogen rich to slightly Ga-rich flux conditions. The window of tran-

sition is usually very small, typically a temperature change of few degrees of the Ga source cell, and corresponds to varying the flux ratio from approximately 0.98:1 to 1.02:1. The important factor being the type of atoms which terminate the surface under quasi-steady-state growth conditions. For even slightly nitrogen rich conditions, the resulting surface becomes predominantly nitrogen atomic terminated, and maintains a spotty wurtzite transmission RHEED pattern. As the Ga cell temperature is increased, the surface evolves to become gallium terminated, and the RHEED pattern streaks out, usually to an unreconstructed (1x1) pattern. Usually no reconstructions are observed during growth, although a two-fold reconstruction is observed for growth interruption under N* soak. In general, the surface reconstructions are only observed at lower temperatures and are distinctive for the different polarities of GaN (see section 2.5.1). A comprehensive study of RHEED patterns and reconstructions for the nitride system was performed by Smith, Feenstra, *et al.* [48]

3.5 Film characterization

Films were characterized *ex situ* by atomic force microscopy (AFM) using a multimode Digital Instruments Nanoscope IIIA, and by high resolution x-ray diffraction (XRD) using a Philips diffractometer equipped with 4-crystal Ge (440) collimation and 2 crystal Bonse-Hart triple axis detector. Layer thickness was confirmed by variable angle spectroscopic ellipsometry (VASE) over the wavelength range 380-780 nm, and carrier concentrations were measured by the Van der Pauw Hall technique.

The polarity of films grown using a GaN buffer layer is believed to be predominantly $(000\bar{1})$ (N-face) based on low temperature observation of the RHEED reconstruction and KOH selective etch tests [47]. (3×3) and (6×6) reconstructions are observed for Ga-rich surfaces when substrate temperatures are below about 400°C, confirming the work of Smith, *et al.* [48] A typical (3×3) reconstructed RHEED pattern (with faint 6-fold lines) is shown in Figure 3.4. These reconstructions are sometimes observed for N-face films at temperatures as high as 700°C, although they are stable for long time periods only below about 400°C [48].

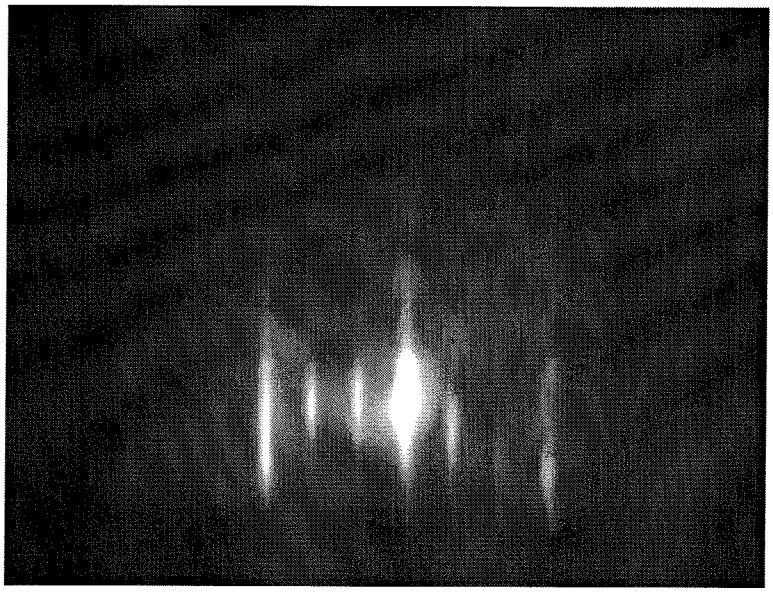

Figure 3.4: (3×3) and (6×6) RHEED reconstructions are observed at low temperature ($< 400°C$) indicating that the GaN films are of $(000\bar{1})$ polarity [48]. Only unreconstructed (1×1) surfaces are observed during growth for either film polarity.

The surface morphology of many of the GaN films was characterized using atomic force microscopy (AFM) and scanning electron microscopy (SEM). Typical AFM images of the sample surfaces are shown in Figure 3.5. Figure 3.5A shows the very flat surface of a 2.2 μm thick sample which contains shallow pits. The pits are believed to be induced by inversion domains. Figure 3.5B shows the surface of a sample grown by first proceeding under N-rich growth conditions followed by growth under Ga-rich conditions. Large, hexagonally faceted mesa-type structures are evident, but the crystalline quality within these structures appears to be quite good. More details on the study of how growth conditions affect surface morphology is presented in chapter 4.

X-ray rocking curves (ω-scans) for several samples, including GaN, $Al_{0.2}Ga_{0.8}N$, and AlN, are shown in Figure 3.6. Very low values for the full width at half maximum (FWHM) have been achieved for these films, which indicates a very high degree of in-plane crystalline ordering. As is common in heteroepitaxy, these nitride films display a mosaic pattern with a range of tilts and twist between domains. The anomalously low values for FWHM observed here can be attributed to the coherent scattering of

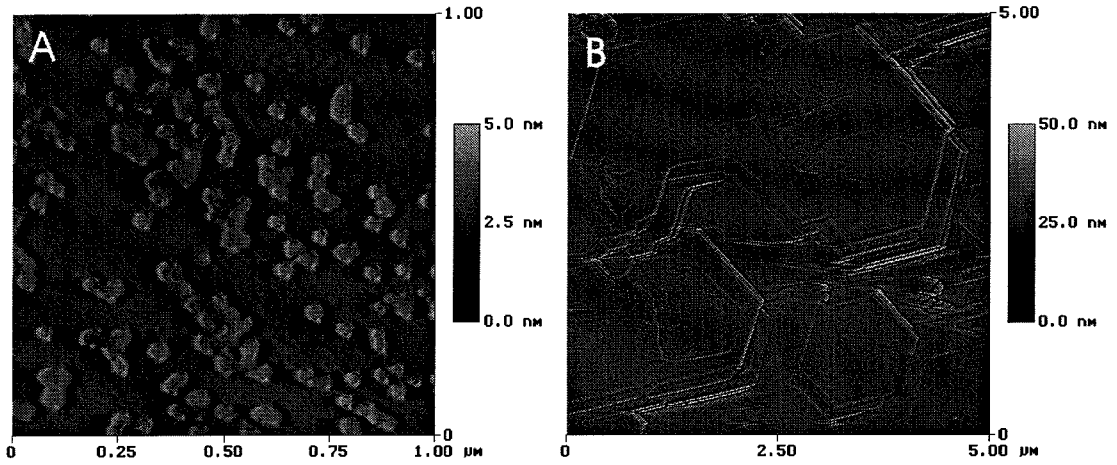

Figure 3.5: A) Tapping mode AFM scan of a 2.2 μm thick GaN sample grown under slightly Ga-rich conditions. The features are pits believed to correspond to N-face inversion domains in a Ga-face polarity matrix. (See chapter 4.) B) AFM scan of a 4 μm thick GaN layer grown by a two stage technique demonstrating increased grain size.

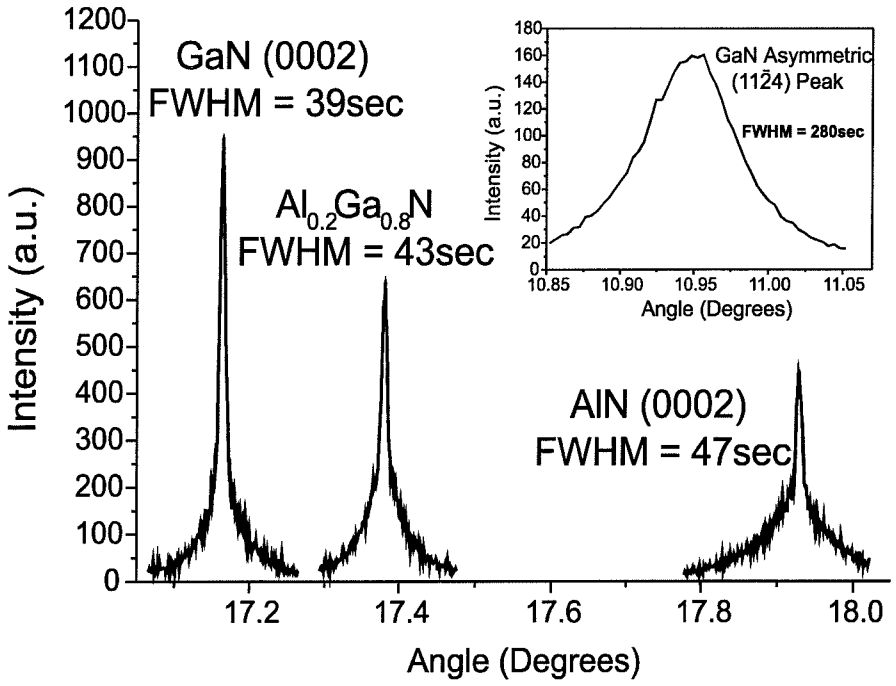

Figure 3.6: Extremely small rocking curve widths (FWHM) can be achieved for GaN, AlGaN, and AlN grown on sapphire. Shown inset is the asymmetric (11$\bar{2}$4) ω-scan for the sample shown in Fig 3.5B.

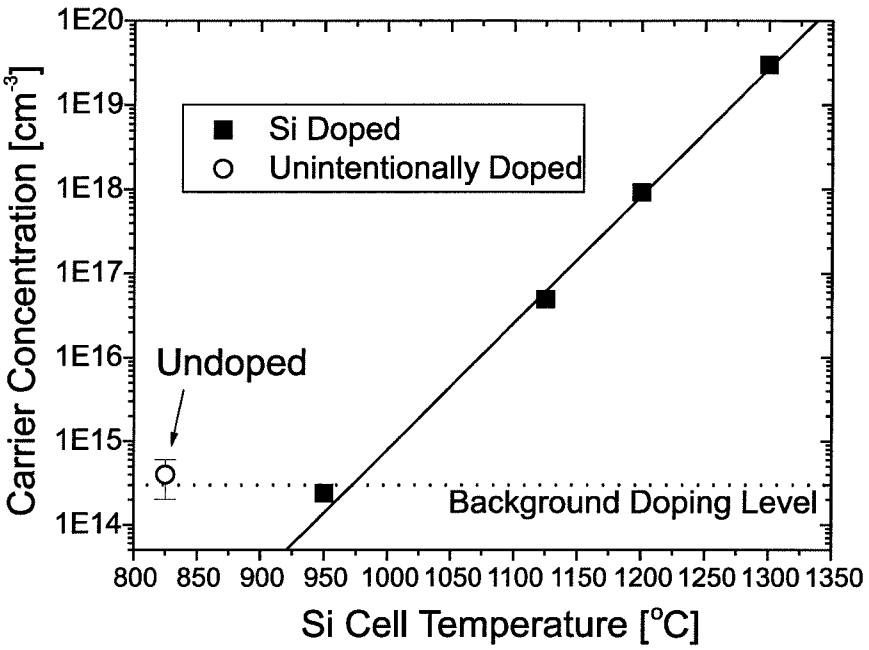

Figure 3.7: The carrier concentration as measured by Hall is shown for Si-doped GaN as a function of Si effusion cell temperature. Doping is controllable and reproducible between the background level (2-4)·10^{14}cm^{-3} and 10^{20}cm^{-3}.

x-rays by mosaic domains that are highly aligned in the growth plane but have a distribution of twists about the c-axis [49]. These films likely have a large number of non-c-axis edge dislocations but relatively fewer screw or mixed dislocations. A better measure of overall structural quality is perhaps the asymmetric $(11\bar{2}4)$ peak width, which is in the 240-300 arcsec range for the best films (and nondetectable for the worst). Inset in Figure 3.6 is the asymmetric $(11\bar{2}4)$ ω-scan for a relatively high quality sample grown using a two stage technique (section 4.5), the AFM surface scan of which is shown in Fig 3.5B.

3.6 Doping of GaN by MBE

3.6.1 Silicon doping of GaN

A series of silicon doped GaN samples was grown in which the doping concentration was varied by adjustment of the Si effusion cell temperature. Figure 3.7 shows the carrier concentration, measured by Hall effect in the Van der Pauw configuration, for

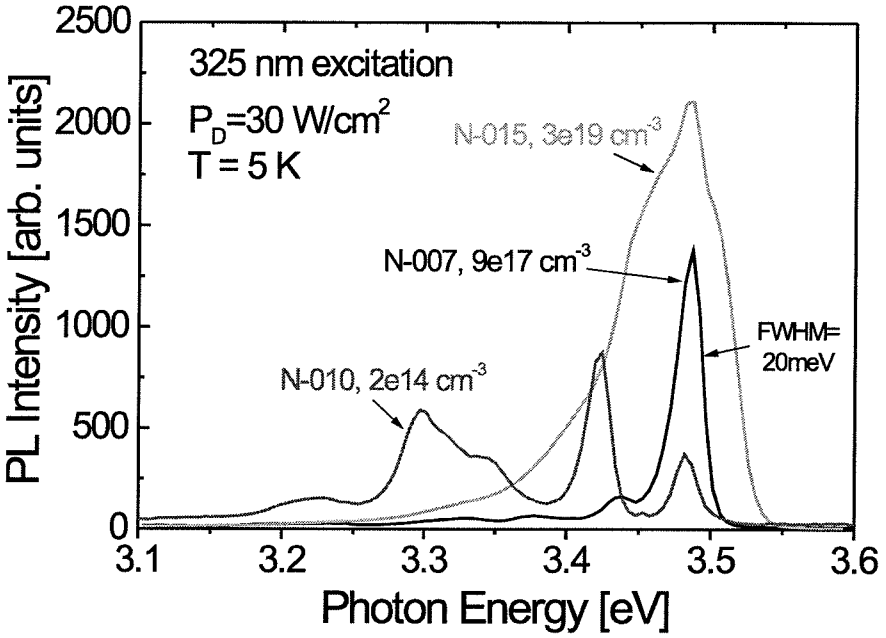

Figure 3.8: Photoluminescence spectra of n-type GaN films taken near the band-edge. Except for the undoped sample, the spectra is dominated by the so-called I_2 line, a neutral donor-bound exciton recombination at 3.48 eV. The unintentionally doped sample also shows some deeper level features at 3.41 eV and 3.3 eV. The PL measurements were done by Z. Bandić.

some of these samples. Control of the donor concentration was found to be rather straightforward, continuously variable between approximately 10^{20} cm^{-3} and the unintentionally doped background concentration of $2-4\cdot10^{14}$ cm^{-3}. The Hall mobility was rather low for films with carrier concentrations below 10^{16} cm^{-3}, typically 50-80 cm^2/Vs, which is quite typical for MBE grown GaN films, but inferior to the best films grown by vapor phase techniques. The low mobility of these is likely limited by scattering and space charge effects due to a high density of edge dislocations, which act as electron traps [50, 51]. The dislocation densities of the films as estimated from mobility measurements were $(1-5)\cdot10^{10}$ cm^{-2}, which is typical for MBE grown GaN films as reported in the literature.

Photoluminescence spectra of the Si-doped n-type GaN films show strong band edge excitonic emission, as shown in Figure 3.8. For the sample doped to $9\cdot10^{17}$ cm^{-3}, the luminescence full width at half maximum (FWHM) is 20 meV, which is quite narrow for GaN grown on sapphire by MBE. When the Si doping level is increased to

$3 \cdot 10^{19}$ cm^{-3} the FWHM broadens to approximately 80 meV. The unintentionally doped sample spectra shown in Figure 3.8 also contains some deeper level features at 3.41 eV and 3.3 eV, which may be due to donor-acceptor transitions between shallow donors and acceptors which are related to impurities or (unscreened) structural defects. These deeper features are not in the right spectral range to correspond to phonon replicas or to cubic phase inclusions.

For most samples, deep "yellow" luminescence centered at 2.2 eV can be observed to a varying degree (see Figure 3.11). There have been a considerable number of reports in the literature regarding the yellow luminescence in GaN, but the specific cause of the deep level has not yet been resolved. The 2.2 eV level has variably been attributed to carbon or other extrinsic impurities, dislocations or other native structural defects, or to gallium vacancies. The yellow level appears in GaN material grown by all techniques, but in most cases its relative intensity can be reduced by growing under optimized conditions. This seems to indicate that the yellow luminescence is linked to native point or extended defects rather than impurities, assuming the incorporation rate of impurities is the same regardless of film microstructure or slight variations in growth conditions.

3.6.2 Magnesium doping of GaN

It is difficult to grow p-type GaN due to the lack of a shallow impurity dopant. The best doping material to date has been magnesium, which achieves an acceptor energy of approximately $E_A \sim 180$ meV [52]. At room temperature, this leads to the hole concentration being much smaller than the active acceptor concentration (N_A).

Using the charge neutrality condition that the number of holes must equal the number of ionized acceptors, the Fermi level position and charge populations can be determined.

$$\frac{N_A}{1 + 2\exp(\frac{E_A - E_F}{kT})} = N_V \exp(\frac{E_V - E_F}{kT}) \tag{3.1}$$

The Fermi level is situated approximately halfway between the acceptor level and the

valence band edge.

$$E_F \simeq E_V + \frac{E_A}{2} + \frac{kT}{2}\ln(\frac{2N_V}{N_A}) \tag{3.2}$$

The standard formula for NV is

$$N_V = 2(\frac{2\pi mkT}{h^2})^{\frac{3}{2}} \simeq 1 \cdot 10^{19}\text{cm}^{-3} \tag{3.3}$$

This value is not exactly correct due to the small splitting of the wurtzite valence band. Shown in Figure 3.9 is the calculated relationship between the free hole concentration and the Mg acceptor concentration in GaN, assuming an acceptor level 176 meV above the valence band edge. Since the acceptor binding energy is much larger than kT, the majority of free holes are frozen out, and the ratio of ionized to neutral acceptors is very small. Because of this, achieving highly p-type GaN is very difficult. To achieve hole concentrations above 10^{18} cm^{-3} requires Mg concentrations in the $10^{20} - 10^{21}$ cm^{-3} range, where doping efficiency is poor, typically resulting in less than 1% of acceptors being ionized.

In our attempts to produce p-type GaN layers, several samples were grown at various substrate temperatures, varying from 660°C to 750°C. The layers grown at or above 750°C were found to be n-type, while the films grown between 660°C and 720°C were verified to be p-type by hot probe measurement. The p-type films are distinctive because of their luminescence spectra. Most of the Mg-doped films showed no band-edge luminescence, rather a broad and deep emission in the region of $380 - 420$ nm. Photoluminescence spectra of several p-type samples is shown in Figure 3.10.

3.7 Growth of nitride alloys

Three aluminum gallium nitride alloy samples were grown. Using x-ray diffraction and assuming Vegard's law, the aluminum content of the films was determined to be 5% for sample N011, 21% for N012, and $\sim$ 76% for sample N006. The photoluminescence scan for sample N011 ($Al_{0.05}Ga_{0.95}N$) is shown in Figure 3.11. The band edge luminescence is now centered on 3.6 eV with a FWHM of 100 meV. We see also

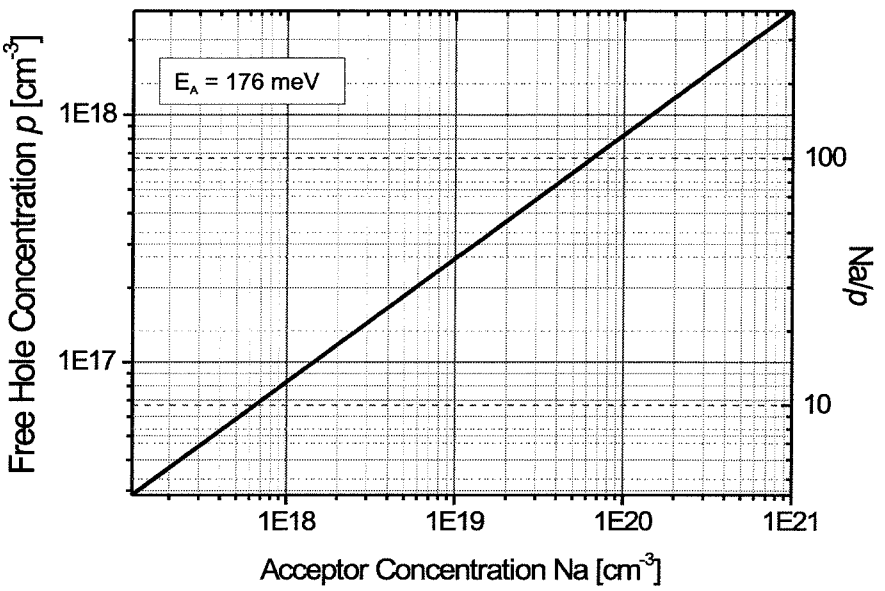

Figure 3.9: Shown is the calculated relationship between the free hole concentration and the Mg acceptor concentration in GaN, assuming an acceptor level 176 meV above the valence band edge. Since the acceptor binding energy is much larger than kT, the majority of free holes are frozen out, and the ratio of ionized to neutral acceptors is very small. Because of this, achieving highly p-type GaN is very difficult.

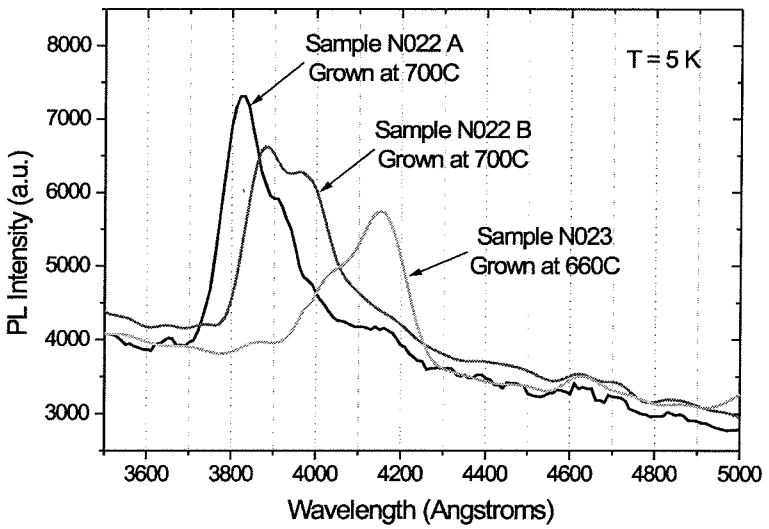

Figure 3.10: Photoluminescence spectra of p-type Mg-doped GaN films. PL scans by C. Hill.

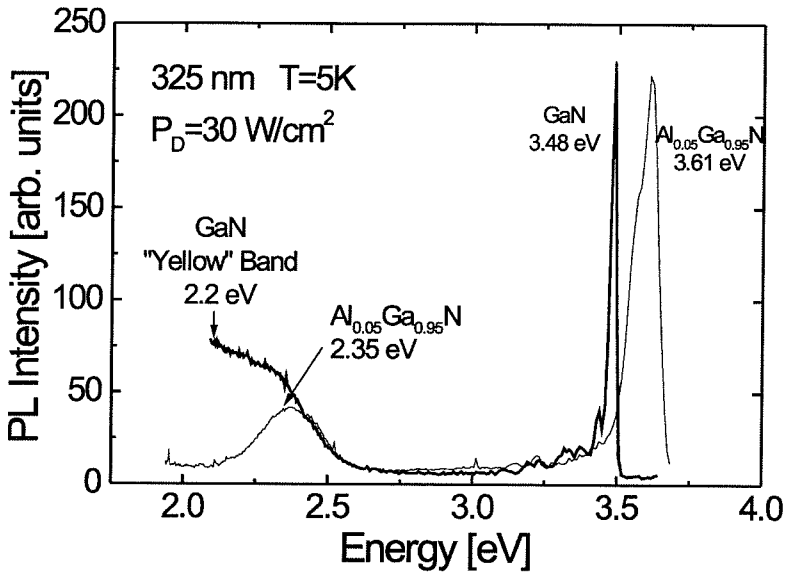

Figure 3.11: Photoluminescence spectra of $Al_{0.05}Ga_{0.95}N$. PL scans by Z. Bandić.

that the "yellow" deep luminescence has shifted to higher energy with the addition of Al. The shift in band edge luminescence indicates that there is very little band gap bowing in these alloy samples.

3.8 Summary and conclusion

GaN, AlN, and $Al_xGa_{1-x}N$ were grown by radio frequency plasma assisted molecular beam epitaxy (RF-MBE) on sapphire substrates. Plasma-assisted MBE of nitrides is a very young field, and still requires significant development of the basic aspects of the technique. This chapter described the MBE system used for the experiments presented in this and subsequent chapters. Reflection high energy electron diffraction (RHEED) was found to be quite useful for the real-time optimization of growth conditions in the nitrides. Spotty RHEED patterns were found to correspond to nitrogen rich growth conditions, while streaky RHEED images were observed for Ga-rich growth, although Ga droplets formed if the Ga arrival rate was too high. The optimum crystal quality was obtained for slightly Ga-rich growth. The GaN films were characterized by AFM and x-ray diffraction. The x-ray curves indicated that films could be grown with very high in-plane structural coherence, despite the large

lattice mismatch present in this materials system. The best FWHM achieved for GaN, AlGaN, and AlN films were 39, 43, and 47 arcsec, respectively.

Doping using Si and Mg was explored. Doping control in n-type GaN was accomplished straightforwardly by co-evaporation of Si during growth. The free electron concentration was controlled between 10^{14} and 10^{20} by variation of Si cell temperature. The measured Hall mobility was rather low for n-type films, indicating a high degree of scattering from charged traps at dislocations. The dislocation densities of the films as estimated from mobility measurements were $(1-5)\cdot 10^{10}$ cm^{-2}, which is typical for MBE grown GaN films as reported in the literature. Magnesium doping was found to be relatively more difficult. As a high vapor pressure species, Mg does not have a long residence lifetime on the GaN surface and desorption is rapid. Incorporation rate is small at typical growth temperatures and is basically independent of the level of Mg flux. The Mg doping level can however be controlled by the substrate temperature, the optimum temperature being in the region of $\sim$700°C. Magnesium is the shallowest known acceptor in GaN and $Al_xGa_{1-x}N$, yet it is still rather deep (170-250 meV), making hole concentrations much lower than acceptor concentrations. The hole mobility was too low for measurement in our Hall setup, but p-type conductivity was confirmed in the Mg-doped samples by hot-probe measurements.

Bibliography

[1] A. Y. Cho and J. R. Arthur, *Prog. Solid-State Chem.* **10**, 157 (1975).

[2] R. Held, D. E. Crawford, A. M. Johnson, A. M. Dabiran, and P. I. Cohen, Surface Rev. and Lett. **5**, 913 (1998).

[3] K. K. Svitashev, V. A. Shvets, A. S. Mardezhov, S. A. Dvoretsky, Y. G. Sidorov, N. N. Mikhailov, E. V. Spesivtsev, and S. V. Rychlitsky, *Mater. Sci. Eng. B* **44**, 164 (1997).

[4] M. Noguchi, K. Hirakawa, and T. Ikoma, *Surf. Sci.* **271**, 260 (1992).

[5] M. J. Paisley, Z. Sitar, J. B. Posthill, and R. F. Davis, *J. Vac. Sci. Technol. A* **7**, 701 (1989).

[6] C. R. Eddy and T. D. Moustakas, *J. Elec. Mater.* **19**, 17 (1990).

[7] H. Sakai, T. Kiode, H. Suzuki, M. Yamaguchi, S. Yamasaki, M. Kioke, H. Amano, and I. Akasaki, *Jpn. J. Appl. Phys. Pt. 2* **34**, L1429 (1995).

[8] H. Tews, R. Averbeck, A. Graber, and H. Reichert, *Electron. Lett.* **32**, 2004 (1996).

[9] J. M. Van Hove, G. Carpenter, E. Nelson, A. Wowchak, and P. P. Chow, *J. Cryst. Growth* **164**, 154 (1996).

[10] R. P. Vaudo, I. D. Goepfert, T. D. Moustakas, D. M. Beyea, T. J. Frey, and K. Meehan, *J. Appl. Phys.* **79**, 2779 (1996)

[11] S. Mohammad, W. Kim, A. Salvador, and H. Morkoç, MRS Bull. **22**, 22 (1997).

[12] S. Porowski, *Mater. Sci. Eng. B* **44**, 407 (1997).

[13] S. Porowski, I. Grzegory, *J. Cryst. Growth* **178**, 174 (1998).

[14] S. Porowski, *MRS Internet J. Nitride Semicond. Res.* **4S1**, G3.10 (1999).

[15] H. Amano, N. Sawaki, I. Akasaki and Y. Toyoda, *Appl. Phys. Lett.* **48**, 353 (1986).

[16] S. Nakamura, Y. Harada and M. Seno, *Appl. Phys. Lett.* **58**, 2021 (1991).

[17] S. Nakamura and G. Fasol, *The Blue Laser Diode* (Springer, Berlin, 1997).

[18] M. Seelmann-Eggebert, H. Zimmermann, H. Obloh, R. Niebuhr, and B. Wachtendorf, *J. Vac. Sci. Technol. A* **16**, 2008 (1998).

[19] S. Keller, B. P. Keller, Y.-F. Wu, B. Heying, D. Kapolnek, J. S. Speck, U. K. Mishra, and S. P. DenBaars, *Appl. Phys. Lett.* **68**, 1525 (1996).

[20] K. Uchida, A. Watanabe, F. Yano, M. Kouguchi, T. Tanaka, and S. Minagawa, *J. Appl. Phys.* **79**, 3487 (1996).

[21] X. H. Wu, D. Kapolnek, E. J. Tarsa, B. Heying, S. Keller, B. P. Keller, U. K. Mishra, S. P. Den Baars, and J. S. Speck, *Appl. Phys. Lett.* **68**, 1371 (1996).

[22] B. P. Keller, S. Keller, D. Kapolnek, W.-N. Jiang, Y.-F. Wu, H. Masui, X. Wu, B. Heying, J. S. Speck, U. K. Mishra, and S. P. DenBaars, *J. Elec. Mater.* **24**, 1707 (1995).

[23] O. Briot, J. P. Alexis, M. Tchounkeu, and R. L. Aulombard, *Mater. Sci. Eng. B* **43**, 147 (1997).

[24] X. H. Wu, P. Fini, E. J. Tarsa, B. Heying, S. Keller, U. K. Mishra, S. P. DenBaars, and J. S. Speck, *J. Cryst. Growth* **190**, 231 (1998).

[25] D. Kapolnek, S. Keller, R. Vetury, R. D. Underwood, P. Kozodoy, S. P. Den Baars, and U. K. Mishra, Appl. Phys. Lett. **71**, 1204 (1997).

[26] T. S. Zheleva, S. A. Smith, D. B. Thomson, T. Gehrke, K. J. Linthicum, P. Rajagopal, E. Carlson, W. M. Ashmawi, and R. F. Davis, *MRS Internet J. Nitride Semicond. Res.* **4S1**, G3.38 (1999).

[27] A. Osinsky, M. S. Shur, R. Gaska, and Q. Chen, *Electron. Lett.* **34**, 691 (1998).

[28] S. Nakamura, N. Iwasa, M. Senoh, and T. Mukai, *Jpn. J. Appl. Phys.* **31**, 1258 (1992).

[29] Z.Z. Bandić, E.C. Piquette, P.M. Bridger, T.F. Kuech, and T.C. McGill, *Mat. Res. Soc. Symp. Proc.* **483**, 399 (1998).

[30] R. P. Vaudo, V. M. Phanse, M. C. Cattrel, and J. M. Redwing, 2nd International Conference on Nitride Semiconductors, Tokushima, Japan, 25-31 October 1997.

[31] G. Nataf, B. Beaumont, A. Bouille, S. Haffouz, M. Vaille, and P. Gibart, *J. Cryst. Growth* **192**, 73 (1998).

[32] H. M. Ng, D. Doppalapudi, D. Korakakis, R. Singh, and T. D. Moustakas, *J. Cryst. Growth* **190**, 349 (1998).

[33] M. J. Murphy, B. E. Foutz, K. Chu, H. Wu, W. Yeo, W. J. Schaff, O. Ambacher, L. F. Eastman, T. J. Eustis, R. Dmitrov, M. Stutzmann, and W. Rieger *MRS Internet J. Nitride Semicond. Res.* **4S1**, G8.4 (1999).

[34] C. G. Van de Walle, C. Stampfl, and J. Neugebauer, *J. Cryst. Growth* **190**, 505 (1998).

[35] T. H. Myers, L. S. Hirsch, L. T. Romano, and M. R. Richards-Babb, *J. Vac. Sci. Technol. B* **16**, 2261 (1998).

[36] M. W. Wang, J. O. McCaldin, J. F. Swenberg, T. C. McGill, and R. J. Hauenstein, *Appl. Phys. Lett.* **66**, 1974 (1995).

[37] EPI Vacuum Products Group, product literature.

[38] N. Grandjean, J. Massies, P. Vennegues, M. Leroux, F. Demangeot, M. Renucci, and J. Frandon, *J. Appl. Phys.* **83**, 1379 (1998).

[39] S. Fujieda and Y. Matsumoto, *Jpn. J. Appl. Phys.* **30**, L1665, (1991).

[40] M. Moldovan, L. S. Hirsch, A. J. Ptak, C. D. Stinespring, T. H. Myers, and N. C. Giles, *J. Elec. Mater.* **27**, 756 (1998).

[41] R. J. Molnar, R. Singh, and T. D. Moustakas, *J. Elec. Mater.* **24**, 275 (1995).

[42] W. E. Hoke, P. J. Lemonias, and D. G. Weir, *J. Cryst. Growth* **111**, 1024 (1991).

[43] A. J. Ptak, K. S. Ziemer, M. R. Millecchia, C. D. Stinespring, and T. H. Myers, *MRS Internet J. Nitride Semicond. Res.* **4S1**, G3.10 (1999).

[44] SVT Associates, Eden Prairie, MN, product literature.

[45] T. C. Fu, N. Newman, E. Jones, J. S. Chan, X. Liu, M. D. Rubin, N. W. Cheung, and E. R. Weber, *J. Elec. Mater.* **24**, 249 (1995).

[46] H. Amano, M. Iwaya, T. Kashima, M. Katsuragawa, I. Akasaki, J. Han, S. Hearne, J. A. Floro, E. Chason, and J. Figiel, *Jpn. J. Appl. Phys. Pt. 2* **37**, L1540 (1998).

[47] J. M. Van Hove, M. F. Rosamond, R. Hickman II, J. J. Klaassen, C. Polley, A. Wowchak, and P. P. Chow, presented at the 17th North American MBE Conference, Penn State, **G.3** (1998).

[48] A. R. Smith, R. M. Feenstra, D. W. Greve, J. Neugebauer, and J. E. Northrup, Phys. Rev. Lett. **79**, 3934 (1997).

[49] T. Metzger, R. Höpler, E. Born, S. Christiansen, M. Albrecht, H. P. Strunk, O. Ambacher, M. Stutzmann, R. Stömmer, M. Schuster, and H. Göbel, Phys. Stat. Sol. (a) **162**, 529 (1997).

[50] H. M. Ng, D. Doppalapudi, T. D. Moustakas, N. G. Weimann, and L. F. Eastman, *Appl. Phys. Lett.* **73**, 821 (1998).

[51] N. G. Weimann, L. F. Eastman, D. Doppalapudi, H. M. Ng, T. D. Moustakas, *J. Appl. Phys.* **83**, 3656 (1998).

[52] H. M. Ng, D. Doppalapudi, D. Korakakis, R. Singh, and T. D. Moustakas, *J. Cryst. Growth* **190**, 349 (1998).

Chapter 4 Growth Conditions and Film Morphology

4.1 Introduction

Many difficulties arise in the growth of GaN epitaxial layers because of the necessity of using a highly mismatched substrate, such as sapphire or silicon carbide. Although silicon carbide has many advantages over sapphire for GaN growth, including a closer match in lattice parameter and a distinct crystal polarity, c-plane sapphire is more often used for reasons of cost. This significant substrate mismatch makes the fabrication of III-nitride layers of high strucural quality all the more difficult. There is a multitude of reasons why the ability to control GaN surface morphology is desirable. For device structures as well as in most materials studies, high structural quality and flat interfaces are essential. As is the case with other heteroepitaxial systems, we will see in the following sections that the defect microstructure and surface morphology of GaN are highly correlated. Both microstructure and surface morphology are also highly influenced by MBE growth conditions.

Of critical importance in the production of high quality films on sapphire are the conditions of film nucleation and buffer layer deposition. As sapphire has no preferred crystal polarity, great care must be taken to initiate the growth of films that are of the desired polar orientation [1, 2] and that are free of inversion (anti-phase) domains [3]. In MOVPE deposited films, for example, growing on the $(000\bar{1})$N face of GaN has resulted in extremely rough surfaces with large pyramidal features, while growing on the (preferred) (0001)Ga face can result in smooth surfaces and overall higher quality films [4]. Recipes for the MOCVD growth of homopolar (0001) GaN on sapphire have been widely reported [5]. Dissimilarly, for MBE growth using a RF nitrogen plasma source, it has been difficult to force homopolar growth (free of inversion domains)

along the (0001)Ga-face direction, as the growth seems to preferentially proceed along the $(000\bar{1})$N-face [6]. Only recently have there been confirmations of Ga-face growth by RF-MBE using AlN buffer layers [2, 7]. Flat surfaces can be achieved on both polarities by MBE under slightly Ga-rich conditions, but special steps need to be taken to produce films that are free of inversion domains, and there are few reported procedures for doing so [8, 9]. Films grown by MBE on sapphire also tend to be highly columnar in structure with greater than 10^{10} cm^{-2} dislocations.

This chapter describes the effect of the growth conditions, especially the Ga/N beam flux ratio and film nucleation conditions, on the surface morphology of GaN films on sapphire substrates, and attempts to shed some light on the defect formation and microstructure evolution during MBE growth. Specific attention is paid to control of the crystal polarity, its selectability during film nucleation, and the supression of inversion domains. In section 4.5 a possible technique is presented for reduction of extended defects by utilizing the III/V flux ratio to control microstructure evolution.

4.2 Morphology and III/V Flux Ratio

When growing III-nitride films by RF plasma assisted MBE, the effective arrival rate ratio of the group III species to the activated nitrogen species (see Reference [10]) is the most significant factor in determining the resulting film surface morphology [9, 11, 12]. Growth under conditions of a slight excess of Ga has been shown to lead to locally flat GaN surfaces and streaky RHEED patterns while growth under Ga-deficient conditions results in spotty, faceted RHEED images and rough surfaces. Stoichiometric growth conditions are taken to be where the growth mode abruptly transforms from two-dimensional to three-dimensional. Typically, the III/N ratio is controlled during growth by fixing the conditions of RF plasma source power and N_2 flow, thus holding the active nitrogen (N*) flux constant, and varying the group III flux by changing the effusion cell (main cell thermocouple) temperature. This is an efficient technique for optimizing conditions real time during growth by observation of the RHEED pattern for visual feedback. To study the effects of flux ratio on

surface morphology as conditions deviate from optimal, a series of samples was grown following the methods described in chapter 3. Specific conditions are briefly described here.

Gallium nitride layers were grown on c-plane (0001) sapphire substrates by radio frequency plasma assisted molecular beam epitaxy (MBE). For each growth, the substrate was first heated to 800°C and exposed to the nitrogen beam for 30 minutes at 450W RF power and at reduced nitrogen flow. Reflection high-energy electron diffraction (RHEED) patterns were bright streaks after the nitridation stage, indicating the formation of an AlN layer at the surface. A thin GaN or AlN buffer layer was then deposited at a nominal growth rate of 0.15 microns per hour at a plasma source power of 350W. For growth of GaN buffer layers, the III/V ratio was set close to unity, while for growth of AlN buffer layers the Al cell temperature was variably set to 1100°C, 1120°C, or 1130°C representing N-rich, near stoichiometric, and Al-rich growth conditions, respectively. The growth time for the buffer layers was 2-3 minutes. After buffer layer deposition, the samples were soaked under the nitrogen beam for 8 minutes. The main GaN layer was then deposited at a rate of approximately 0.4 microns per hour at a substrate temperature of 800°C.

A series of samples was grown utilizing GaN buffer layers, wherein subsequent growth of the main layer was carried out under N-rich, slightly Ga-rich, or heavily Ga-rich conditions. For GaN layers grown on AlN buffer layers, flux conditions were slightly Ga-rich and constant. The total thickness of these layers was about 1 micron. Additionally, one sample was grown to a thickness of 2 microns using an AlN buffer layer. All films were doped with Si to approximately 10^{17} cm^{-3}. The surface morphology of these layers was studied by atomic force microscopy in Tapping Mode using a Bioscope AFM with a Digital Instruments Nanoscope IIIa controller, and by scanning electron microscopy (SEM) using a JEOL 6400V. High-resolution x-ray diffraction (XRD) measurements were performed using a Philips diffractometer equipped with 4-crystal Ge (440) collimation and 2 crystal Bonse-Hart triple axis detector. GaN polarity was determined by RHEED reconstruction at low temperature [6], and by molten KOH etching [4].

4.2.1 Growth on GaN buffer layers

Figure 4.1 shows a series of AFM surface scans taken from GaN samples grown under nitrogen rich (A), slightly Ga-rich (B) and more highly Ga-rich (C) flux conditions. These samples were grown using a 650°C GaN buffer layer on sapphire, and are all approximately one micron thick. In (A), the rough surface and small, grainy microstructure is evident, while in (B) we see a "brain-like" morphology with larger flat regions separated by shallow ($\sim$ 200 nm) canyons. The surface roughness is approximately 10 nm RMS in this case and the grain size is improved. The scan shown in (C) was taken between Ga droplets, which sparsely covered the surface of this sample. In this case, the surface appears to be quite flat (RMS roughness $2-3$ nm), with a network of pits decorating $0.5-1$ μm grains. The pits are somewhat larger than those seen in AFM analysis of MOCVD-grown films, which were attributed to dislocations at grain boundaries intersecting the surface. In this case, the pits may be related to Ga-droplet formation. For this film the density of the pits is $7 \cdot 10^8$ cm^{-2}, which, if it corresponds to dislocation density, is a very good result comparable to the best MOCVD-grown films.

We see from Figure 4.1 that morphology improves as the Ga/N flux ratio is increased. Ultimately, however, gallium condensation takes place and metallic droplets form at the surface, which is undesirable. Droplets are especially problematic for the growth of alloys, such as Al_xGa_{1-x}Nand $In_xGa_{1-x}N$, since they can lead to compositional nonuniformity. The improvement in surface flatness with Ga-rich conditions observed here differs from results obtained by MOCVD, and by ammonia MBE [13], where the best morphology was seen using an excess of nitrogen. Clearly the details of growth are different in these cases, likely due to the presence of hydrogen and ammonia.

4.2.2 Growth on AlN buffer layers

Samples grown using AlN buffer layers display the same basic behavior vs III/N ratio as do samples grown on GaN buffer layers. Streaky RHEED patterns and lo-

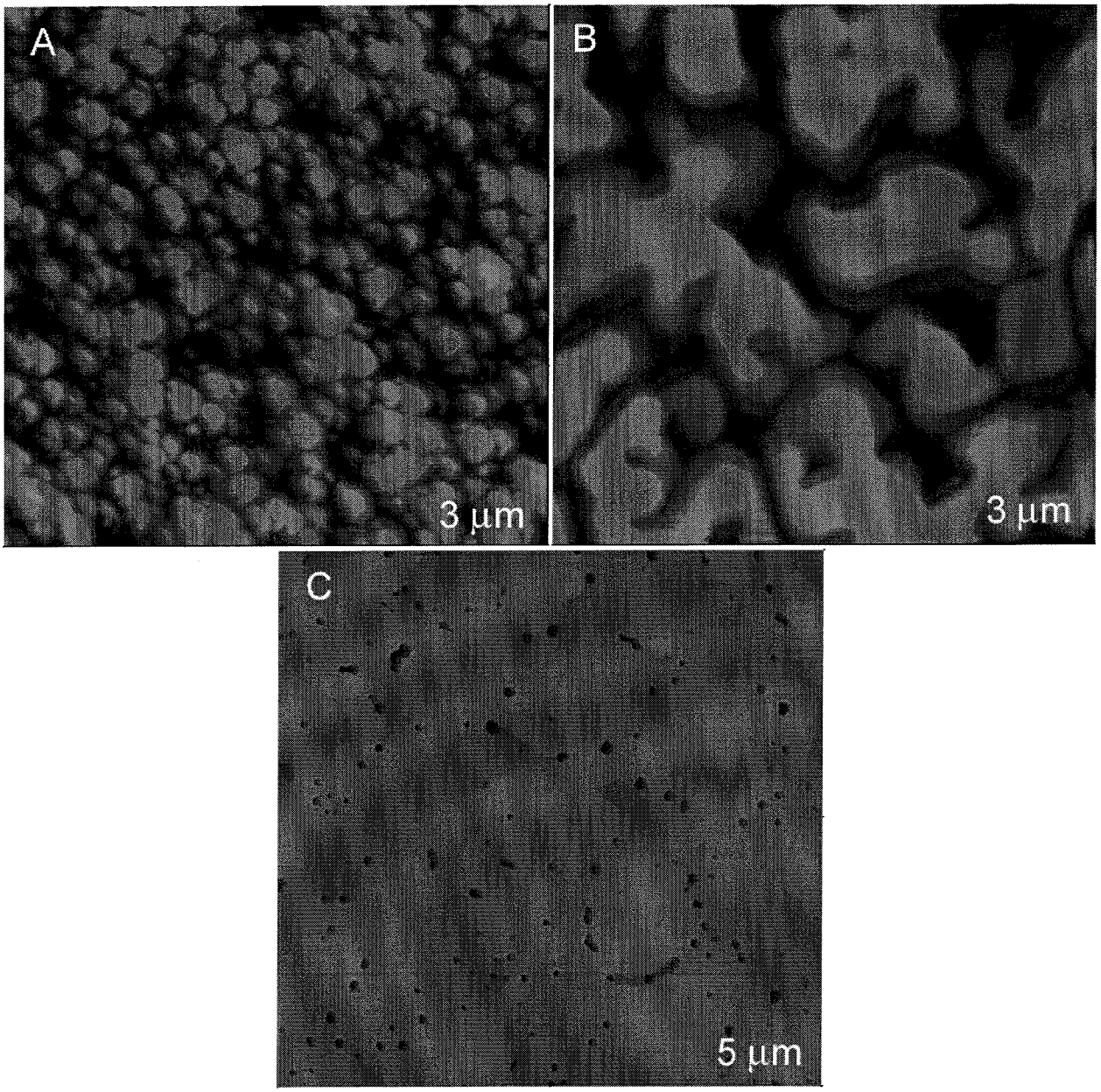

Figure 4.1: AFM micrographs of GaN grown on sapphire using GaN buffer layers. For nitrogen rich growth of the main layer (A) a rough surface and fine-grained microstructure results, while growth under slightly (B) and more heavily Ga-rich (C) conditions leads to larger grain size and flatter surfaces. The surface pictured in (C) is quite flat, with pit defects lying at the coalesced island boundaries. The vertical scale is 100 nm in these images.

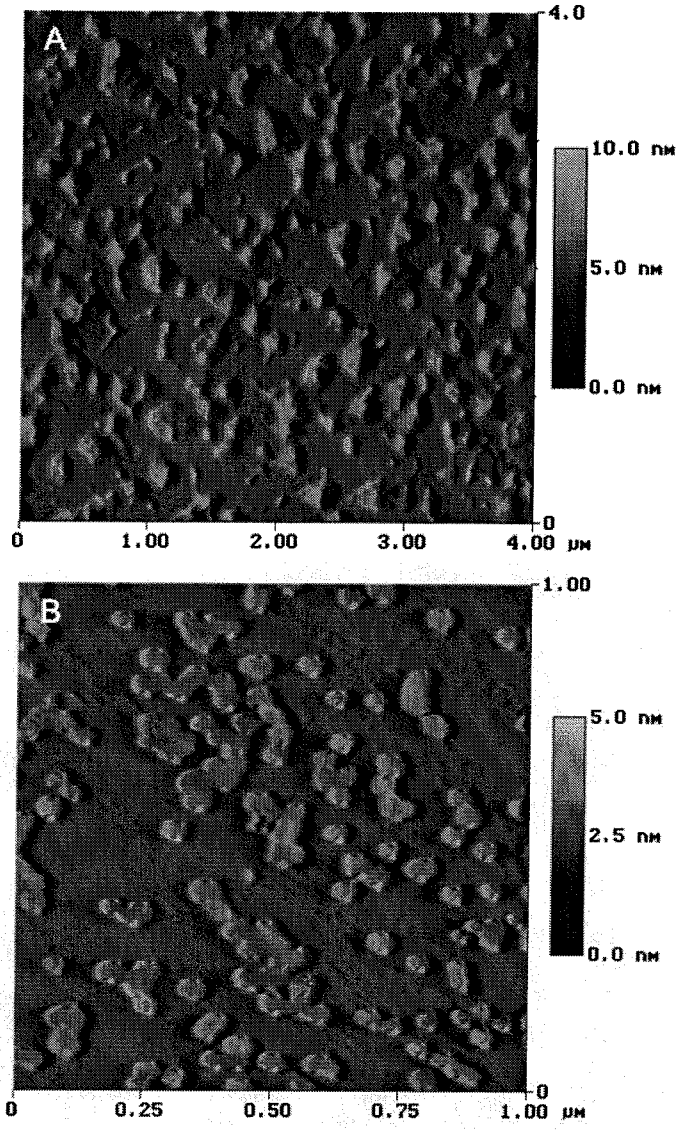

Figure 4.2: AFM scans of the GaN surfaces for A) a sample grown near stoichiometric flux conditions, and B) a sample grown under Ga-rich conditions. The pits present on the flat background are thought to be caused by decreased growth rate at inversion domains.

cally smooth surfaces are obtained using gallium-rich growth conditions. For samples grown near stoichiometric conditions, the RHEED pattern was generally streaky but sometimes displayed a small amount of faceting. Figure 3.4.1A shows the AFM surface scan of such a layer. We see that even though the RHEED image is streaky, the entire surface of the film is not flat. Pits are present on a mostly flat background. These pits are approximately 30 nm deep and $\sim$ 200 nm wide and are attributed to the presence of inversion domains. A more thorough discussion of these pit defects is presented in section 4.5. Note that as the Ga/N ratio is increased (Figure 4.2) the depth of the pits decreases. In fact, very flat surfaces can be produced by growing under Ga-rich conditions on AlN buffer layers on sapphire. The depth of the pits shown in Figure 4.2B is approximately 2 nm, while the RMS surface roughness of the sample is approximately 1 nm.

4.2.3 Highly N-rich growth

While the flattest surfaces can be produced using Ga-rich flux conditions, as the growth conditions become more nitrogen-rich, especially at high growth temperatures, interesting and complicated morphological features can arise. The $\{11\bar{2}0\}$ azimuth RHEED pattern observed during growth for one such film is shown in Figure 4.3A. In general the spotty transmission pattern indicates a wurtzite film with a three dimensional surface. Some streaks can be seen overlaying this pattern both orthogonal and parallel to the sample surface plane. These streaks indicate faceting in the $\{0001\}$ and $\{10\bar{1}0\}$ planes, respectively. The vertical $\{10\bar{1}0\}$ facets (horizontal RHEED streaks) are unusual in the MBE growth of GaN, but indicate the high stability of these crystal surfaces. No horizontal streaks were observed for the $\{10\bar{1}0\}$ azimuthal RHEED image. The SEM plan view scan of a film grown with Ga/N flux ratio of 1:3 is shown in Figure 4.3B. A mesh-like morphology is observed. These GaN fiber structures are somewhat oriented along the $\{11\bar{2}0\}$ crystalline directions, with some degree of misalignment. Equivalently, the side walls of the pits which lie between the fibers are aligned in these directions. The SEM data therefore also indicates the presence

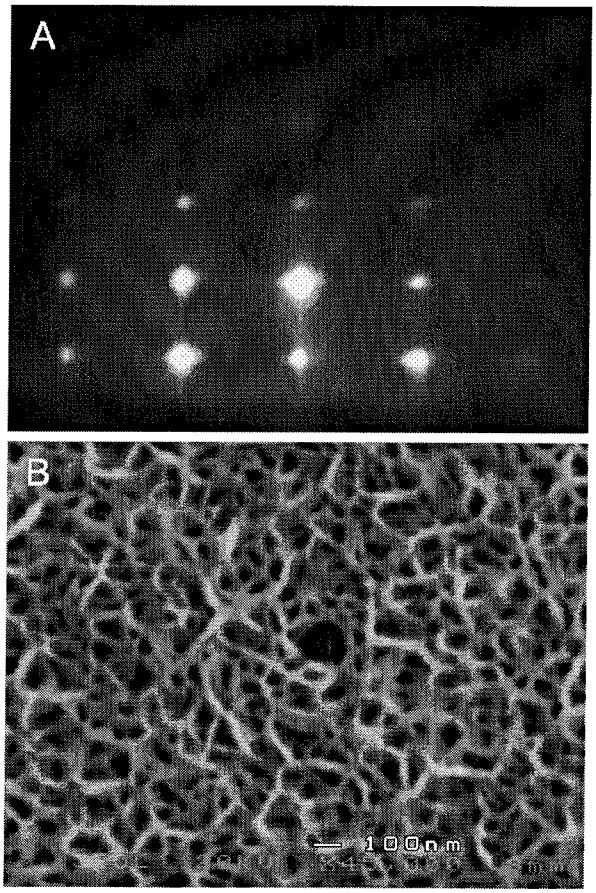

Figure 4.3: A) Shown is the RHEED image of a GaN sample grown under highly N-rich flux conditions. Note the presence of both horizontal and vertical streaks superimposed on the spotty wurtzite transmission pattern. B) The plan view SEM photograph of the same sample presents a complex mesh-like surface morphology. The mesh is somewhat aligned with the $\{11\bar{2}0\}$ GaN directions. The pits have sidewalls that are $\{10\bar{1}0\}$ facets, and may correspond to "opened" threading dislocations.

of $\{10\bar{1}0\}$ facets. The net growth rate of films under these conditions is slow, and the decomposition rate is high. The appearance of facets on the $\{10\bar{1}0\}$ and $\{0001\}$ planes suggests that the decomposition rate is slow on these planes. This variation in growth and decomposition rates for the different crystal directions and for high N/Ga ratios is quite similar to results obtained in lateral epitaxial overgrowth of GaN by MOVPE [14] and HVPE, and also TEM observations of nano-pipes and pits [15]. The morphology seen here can also be explained by the "opening up" of threading dislocations into nano-pits in this highly nitrogen rich and reactive environment. The density of pits in Figure 4.3B is approximately 10^{10} cm^{-2}, which coincides with the density of extended defects in a typical MBE GaN film. This morphology also bears similarity to that reported for GaN annealed in forming gas [2].

4.2.4 Analysis of growth modes

The different growth modes observed for nitrogen-rich vs gallium-rich conditions can be explained by considering the mobility of surface adatoms on the nitrogen- and gallium-terminated surfaces [16]. For Ga/N flux ratios less than one, spotty and sometimes faceted RHEED patterns are observed during growth. It is plausible that the low flux ratio gives rise to a (partly) nitrogen terminated surface which has a high sticking coefficient for Ga atoms, but low surface mobility, and the morphology then evolves by statistical roughening [3]. For a nitrogen atom on a nitrogen terminated surface, likely there is a high rate of dimer (N_2) formation and subsequent rapid desorption. Thus the residence lifetime of nitrogen radicals is likely to be higher on a gallium-terminated GaN surface. This increased lifetime and thus migration distance enhances the probability of bonding at a step edge, and would more easily maintain a flat morphology by either step-flow or layer-by-layer growth. Also, recent calculations [17] have also shown that the energy barrier for hopping from surface site to adjacent site is much smaller for Ga on gallium-terminated than for Ga on nitrogen-terminated surfaces. The gallium atoms are much more mobile on Ga-terminated surfaces, leading to enhanced two-dimensional growth and smoother morphology.

4.2.5 Surfactants

A somewhat related topic to that of the previous section are the possible candidates for surfactants in the growth of GaN, these being magnesium and indium [18]. The most promising of these is perhaps indium, since its vapor pressure is lower than that of Mg, and (unintended) incorporation will not result in doping of the film. Calculations have predicted that the mobility of Ga on an In terminated (0001) surface is significantly higher than it is for a Ga-terminated surface. This increase in surface mobility gives rise to higher quality films and surfaces [18]. In fact, the atomic spacing of indium atoms on the GaN surface (basically the GaN lattice parameter) is close to the spacing for bulk In metal. Thus the relaxed In surface termination should result in very low surface energy, ideal for the role of a surfactant. An additional benefit of using indium in this manner is that it would allow growth in the regime where Ga/N ratio is slightly less than one. Flat morphology and streaky RHEED patterns could thus be obtained under these conditions without fear of Ga condensation and droplet formation at the surface.

4.3 Film nucleation and buffer layer conditions

4.3.1 AlN buffer layers

Samples grown using GaN buffer layers on sapphire were found to be N-polar [7] based on etch tests using molten KOH [4, 19], while films grown using AlN buffer layers were Ga-polar. Both polarities seem to behave similarly in the effects of III/V ratio on surface morphology and growth mode [20, 16]. Additionally, for films grown on AlN buffers, the exact conditions of buffer layer deposition are seen to be highly important. Shown in Figure 4.4 are AFM scans of GaN films grown under identical conditions except for the Al/N flux ratio during growth of the buffer layer. If the AlN buffer is deposited under Al-rich conditions (Figure 4.4A), the RHEED pattern dims and ultimately disappears as aluminum builds up on the surface. The fine-grained microstructure observed is likely formed by nitridation of condensed Al during and

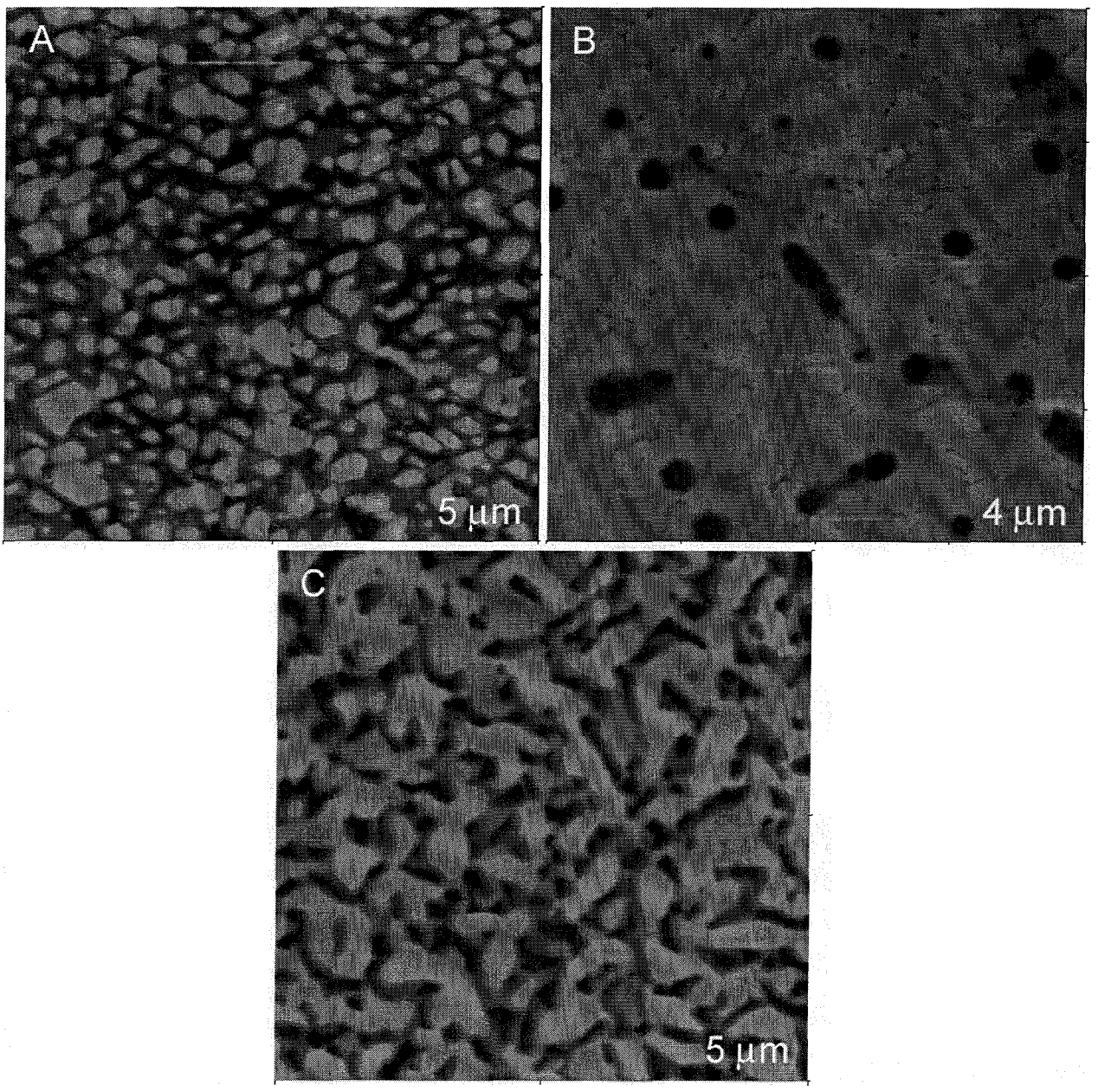

Figure 4.4: AFM micrographs of GaN grown on sapphire using an AlN buffer layer. The aluminum cell temperature was set to (A) 1130°C, (B) 1120°C, and (C) 1100°C during growth of the buffer layers, corresponding to Al-rich, near-stoichiometric, and N-rich conditions, respectively. The GaN layer was grown under the same slightly Ga-rich conditions in all cases. The vertical scale is 100 nm.

after buffer deposition. Figure 4.4B shows the GaN film surface using an AlN buffer layer grown near effective 1-to-1 flux stoichiometry. In this case, the buffer layer RHEED pattern remained very streaky and displayed a faint two-fold reconstruction upon nitrogen soak. The surface appears quite flat but with V-shaped hexagonal pits approximately 200 nm in size. For the case of nitrogen-rich AlN buffer layer deposition, the resulting GaN film surface is shown in Figure 4.4C. Flat regions exist, yet the surface remains rough on the 500 nm lateral scale. Although streaky RHEED patterns were observed during GaN growth for all these samples, only the AlN buffer layers grown under stoichiometric flux conditions showed a streaky RHEED image. We believe that the film-buffer interface is smoothest in this case, and that this is the most relevant condition for the subsequent growth of flat GaN surfaces.

4.4 Surface structures of (0001) GaN

Now let us take a closer look at the specific surface defect structures observed for the films grown using AlN buffer layers. AFM images of a 2 micron thick GaN layer grown on a "stoichiometric" AlN buffer layer are shown in Figures 4.5 and 4.6. We see in Figure 4.5 the same general morphology as in Figure 4.4B. In the AFM Tapping Mode phase image (Figure 4.5B), three types of structures are present on these surfaces which are referred to as large pits, small pits, and "loop" defects. While a detailed study of these defects has not yet been done, we may tentatively associate the small pit defects to the intersection of threading dislocations with the surface [21], as they are similar to pits seen on MOCVD-grown material which was characterized by TEM. The large pits are discussed below, but the nature of the "loop" structures is at this point uncertain. As is shown in Figure 4.6, the large pit defects are not present near the edge of the wafer for this sample. This is due to a degree of temperature nonuniformity across the 2 inch substrate. The substrate temperature is slightly lower toward the edge of the wafer, where the Ga re-evaporation rate is correspondingly reduced. Often, for Ga-rich growth conditions, we have observed the formation of droplets near the substrate perimeter but see none near the center of the wafer.

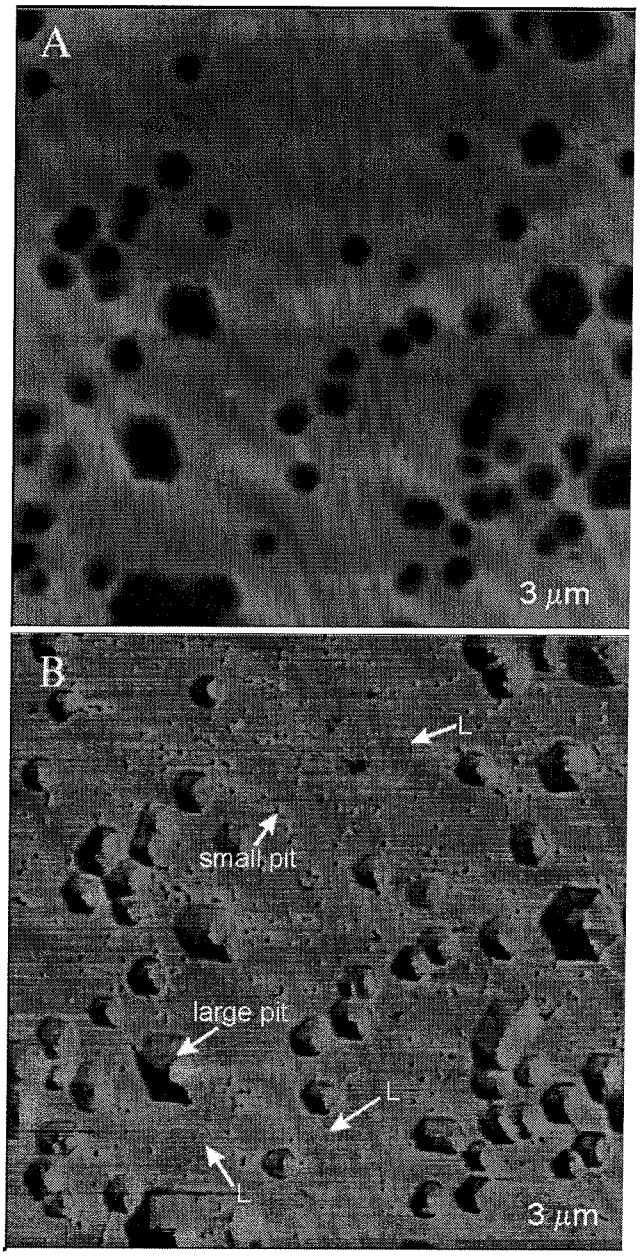

Figure 4.5: Tapping Mode AFM height (A) and phase (B) data taken from the center region of the 2 micron thick GaN sample. Three categories of defects are observed: large hexagonal pits, small pits, and "loop-like" defects (L). The height scale is 100 nm and 25 degrees in A and B respectively.

AFM scans near the edges of samples also tend to display flatter morphology. This morphological nonuniformity is believed to result from the coupled effects of relatively higher substrate temperature and lower effective III/V ratio near the center of the substrate as compared to the edge. The surfaces away from the wafer center, shown in Figure 4.6, are very flat, with RMS roughness less than 1 nm. It is in these flat regions near the substrate edge that the best high electron mobility transistor (HEMT) performance has been observed by other groups [22, 7].

There are several possibilities as to the origin of the large pits seen in Figures 4.2 and 4.5. Let us consider these possibilities in light of the admittedly incomplete experimental evidence that we have. Firstly, they could be remants of island coalescence. That is, as the GaN film nucleates on the sapphire substrate, island nucleation crystallites form, which then grow and coalesce. The pits would then indicate that the film has not yet reached a fully coalescenced condition. This possibility can be discounted because the size and number of the large pits does not seem to scale directly with the thickness of the film, rather the pits seem to maintain their size and thread upwards along the growth direction. Secondly, the pits may be formed by a site blocking mechanism due to gallium droplets building up on the surface. This possibility can likely also be discounted since the number density of pits seems to decrease as gallium flux is increased. Thirdly, the large pits may be due to dislocations which contain a screw component in their Burgers vector, while the small pits are due to pure edge dislocations. While this is possible, the author considers it unlikely because MBE growth takes place very far from thermodynamic equilibrium, and such a differentiation in surface structure due to strain induced by dislocations is not expected, especially when pits observed on HVPE-grown or MOCVD-grown GaN are much more similar in size. Also, if the large pits were due to mixed or screw dislocations, the pits would be expected to be of discrete sizes, which is not observed. Fourthly, the pits may indicate the presence of cubic or amorphous inclusions, but again, no evidence of such was observed in x-ray diffraction analysis. The fifth and most likely possibility for the origin of the large pits is that they are N-polar $(000\bar{1})$ inversion domains in the predominantly (0001) crystal. The pits presumably

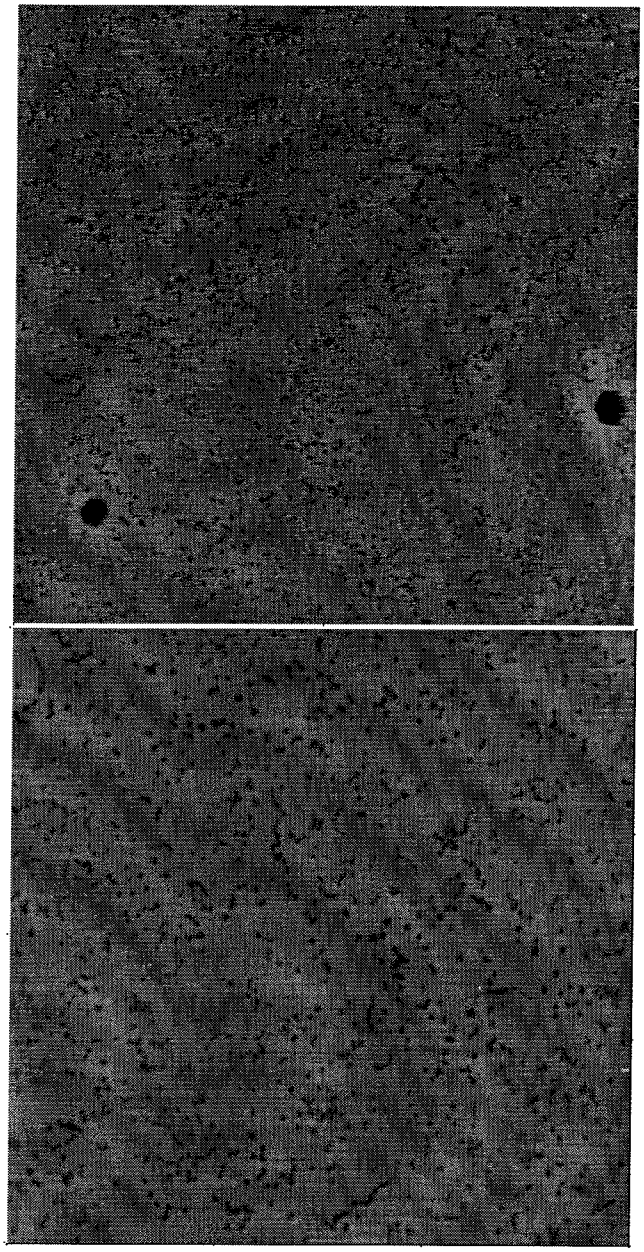

Figure 4.6: AFM scans of two micron thick GaN layer grown using an AlN buffer layer (A) halfway from center to edge, and (B) near the edge of the 2 in. sapphire wafer. The more Ga-rich conditions toward the edge of the substrate serve to reduce (A) and ultimately eliminate (B) the large pit defects, but the small pits and "loop" defects remain. The height scale is 30 nm.

are formed due to slight differences in growth rate between the two crystal polarities.

Myers, *et al.* [3], have observed similar effects for the case of Ga-polar inversion domains in a N-polar matrix, where the inversion domains, having a slightly higher growth rate, formed hillocks. Myers has also shown that as the Ga/N flux ratio is increased from 1:1, the growth rates of the two polarities tend to become equalized, and the height (depth) of the hillocks (pits) is reduced. Very flat films can be grown under these slightly Ga-rich conditions. Figure 4.2B shows such a film, with pits that are approximately 2 nm deep and 40 nm wide. The next logical step, of course, in the analysis of these surface structures is analysis by TEM, which should be able to clarify the nature of the pit defects definitively.

Referring to Figure 4.6B, we see that MBE-grown GaN surfaces can be made quite flat, with RMS roughness less than 1 nm. But we also see that there remains a very high density ($> 10^{11}$ cm^{-2}) of small pits, and thus dislocations in these films. In fact, there seems to be some anti-correlation between the surface morphology and the defect density, the smoothest surfaces having the most dislocations. This makes sence considering that if the surface morphology is maintained as flat as possible throughout growth, the misfit dislocations thread parallel to each other along the growth direction, and have no opportunity to annihilate or to bend into the plane of the film. It is thus possible that the defect density may be reduced by forcing or allowing the surface morphology to become rough, so as to allow the high number of misfit dislocations to deviate from their c-axis propagation. This line of reasoning is carried out in an experiment described in the next section.

4.5 Two stage growth

Some samples were grown by first depositing GaN under nitrogen-rich conditions, followed by growth under Ga-rich (approximately 2:1) fluxes. As above, the RHEED pattern during the first growth stage was spotty with faceting. We expect that this layer is highly defected and heteropolar. At the transition from N-rich growth to Ga-rich growth, the RHEED pattern initially became very dim, but then began to

evolve into a streaky pattern, and continued to improve with growth. Samples were removed after approximately one micron (sample A) and two microns (sample B) of Ga-rich growth. The surfaces of these films exhibit large hexagonal flat-topped mesas observable by SEM and AFM. SEM photographs of these surfaces are shown in Figure 4.7.

After one micron of Ga-rich growth, the mesa structures of Sample A remain mostly isolated. But after an additional micron of growth, we see that these mesas have started to coalesce (Figure 4.7C). At this point, the RHEED pattern is very streaky, showing high contrast (1×1) during growth and (2×1) reconstruction under nitrogen soak. During cool down, clear (2×2) reconstructions can be observed, indicating Ga-polarity. Figure 4.8 shows the cross sectional SEM image of sample B, in a region where several hexagonal islands have merged. It is apparent that columns grow up from the first, N-rich GaN layer, which then grow laterally and coalesce. We speculate that the growth under N-rich conditions exploits the difference in growth rates between the (0001) and $(000\bar{1})$ GaN directions, allowing Ga-face columnar domains to outgrow the N-face regions. Upon commencement of the second layer, lateral growth is facilitated and the Ga-face protrusions overgrow the material of opposite polarity. The highly Ga-rich conditions lead to droplet condensation at the edges of the growing islands, and ultimately form the voids that are present at the interface. This may be similar to the Ga-rich buffer layer technique of references [9] and [23] or to results obtained by Held, Cohen, *et al.* [8], where the formation of inversion domains could be suppressed by utilizing nucleation layers formed by repeatedly nitriding a condensed Ga surface on sapphire. Lateral growth of GaN may lead to a possible reduction in defect density and improved crystal quality, as occurs in MOVPE [14, 24]. TEM or other techniques have not yet been used to count the defects in the two-stage samples. We have, however, observed a considerable improvement in structural quality as measured by x-ray diffraction. Indeed, the asymmetric x-ray peak $(11\bar{2}4)$ FWHM is reduced from greater than 1000 arcsec to as low as 280 arcsec in the two-stage GaN films. Some other traditional characterization techniques, such as Hall and photoluminescence, are made difficult in these samples because of the buried interface.

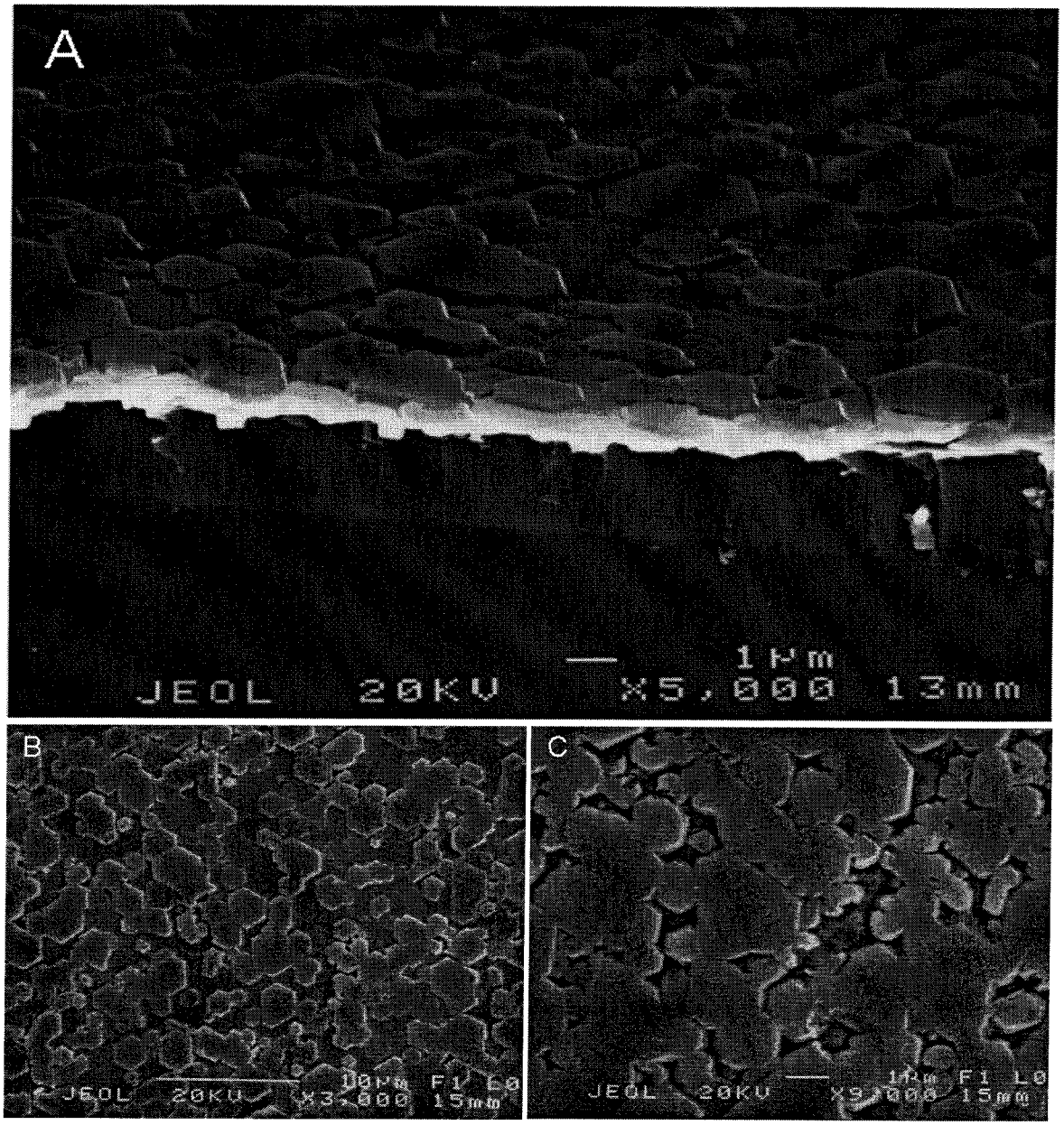

Figure 4.7: SEM images of GaN samples grown first under N-rich conditions, followed by growth under Ga-rich conditions. A) (oblique view) and B) (plan view) show the formation of micron-size flat-topped hexagonal islands for two-stage sample A. After one micron of growth, these islands are still mostly isolated. C) SEM plan view of sample B after two microns of growth under Ga-rich conditions. The hexagonal islands are now beginning to coalesce.

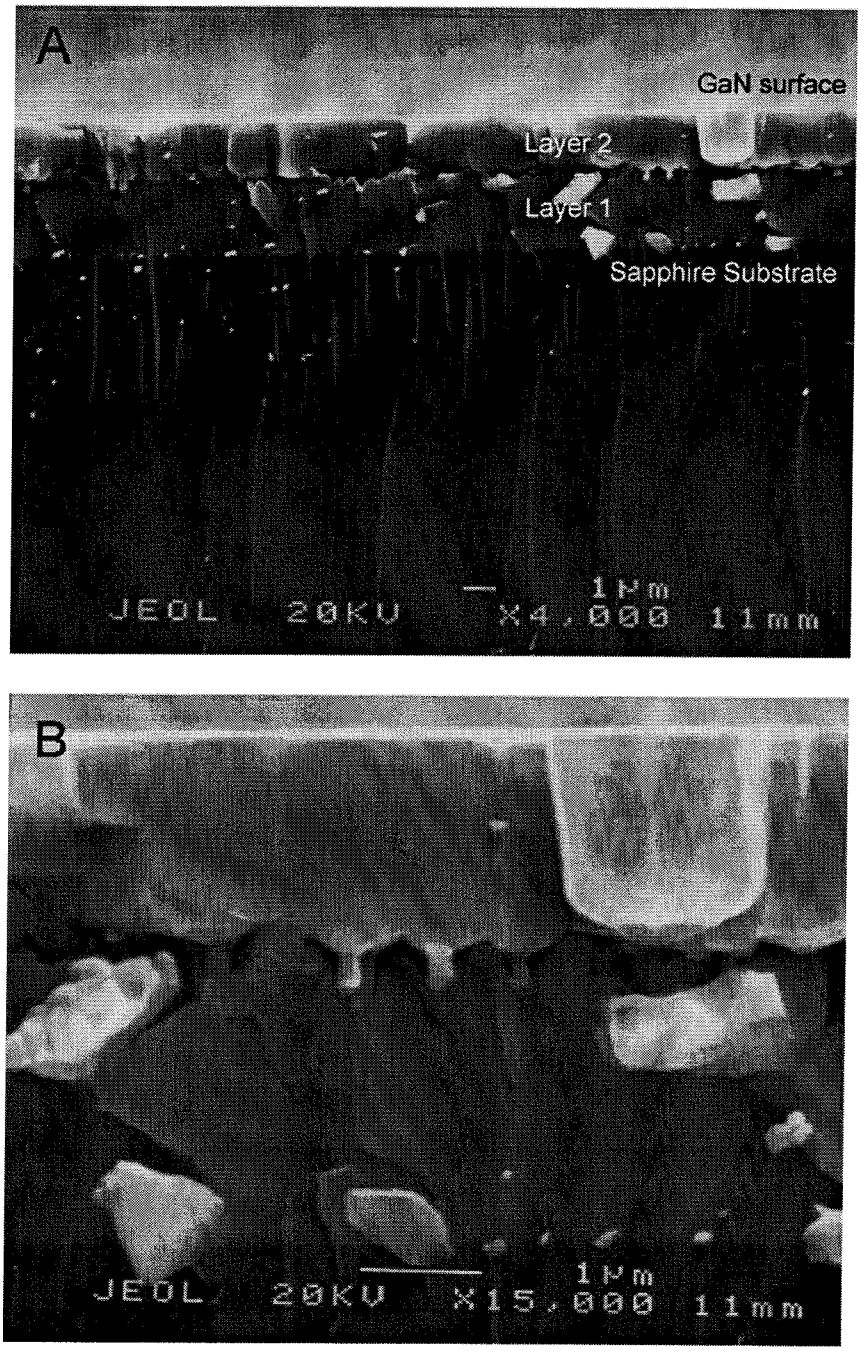

Figure 4.8: A) Cross-sectional SEM view of sample B in a region where islands have coalesced. Note the network of voids and columns at the interface between layer one, grown under N-rich conditions, and layer two, grown under Ga-rich conditions. The presence of voids can be attributed to Ga condensation. It is evident that lateral growth of micron-scale islands proceeds in layer two. B) shows a close-up of A).

4.6 Summary and conclusion

Gallium nitride was grown on sapphire (0001) substrates by RF-MBE. The surface morphology was characterized by RHEED, SEM, and AFM. It was found that generally flat films can be grown using slightly Ga-rich flux conditions, but some contain pits indicating the presence of inversion domains. The growth and decomposition rates for various crystal directions are seen to be dependent on the flux conditions. Specifically, under N-rich conditions the $\{11\bar{2}0\}$ decomposition rates are higher than for the $\{10\bar{1}0\}$ and $\{0001\}$ directions, which can form stable facets. This is similar to growth by MOVPE. Near stoichiometric flux conditions, the (0001) growth rate is slightly higher than the $(000\bar{1})$ growth rate. As growth becomes more Ga-rich, the (0001) and $(000\bar{1})$ growth rates become more equal, up to the point of Ga condensation, where droplets may form. For samples grown by first depositing GaN under N-rich conditions, followed by growth under Ga-rich conditions, lateral growth and coalescence of micron-scale islands can occur over an interface of networked columns and voids, leading to structurally superior surface layers.

The surface morphology of GaN was studied by AFM for a variety of growth conditions. For growth on GaN buffer layers, the films were observed to be N-polar and strongly dependent on III/V flux ratio. The flattest surfaces were obtained by growing as Ga-rich as possible, although Ga droplets tend to form if the III/V ratio is too high. Films grown on AlN buffer layers were observed to be Ga-polar, with the surface morphology strongly dependent on the conditions of buffer layer deposition. Near-stoichiometric buffer growth conditions appear to support the flattest surfaces in this case, likely because these conditions result in the smoothest buffer layer interfaces. Three defect types are typically observed in GaN films on AlN buffers, including large and small pits and "loop" defects. It is possible to produce surfaces free from large pit defects by growing thicker films under more Ga-rich conditions. In such cases the surface roughness can be reduced to less than 1 nm.

Bibliography

[1] For a more detailed description of GaN crystal polarity, see for example, J. L. Rouviere, J. L. Weyher, M. Seelmann-Eggebert, and S. Porowski, *Appl. Phys. Lett.* **73**, 668 (1998).

[2] E. S. Hellman, *MRS Internet J. Nitride Semicond. Res.* **3**, 11 (1998).

[3] T. H. Myers, L. S. Hirsch, L. T. Romano, and M. R. Richards-Babb, *J. Vac. Sci. Technol. B* **16**, 2261 (1998).

[4] M. Seelmann-Eggebert, J. L. Weyher, H. Obloh, H. Zimmermann, A. Rar, and S. Porowski., *Appl. Phys. Lett.* **71**, 2635 (1997).

[5] O. Briot, J. P. Alexis, M. Tchounkeu, and R. L. Aulombard, *Mater. Sci. Eng. B* **43**, 147 (1997).

[6] A. R. Smith, R. M. Feenstra, D. W. Greve, M.-S. Shin, M. Skowronski, J. Neugebauer, and J. E. Northrup, *Appl. Phys. Lett.* **72**, 2114 (1998).

[7] M. J. Murphy, T. J. Eustis, H. Wu, W. Yeo, W. J. Schaff, O. Ambacher, J. Smart, J. R. Shealy, and L. F. Eastman, *J. Vac. Sci. Technol. B* **in press**.

[8] R. Held, D. E. Crawford, A. M. Johnson, A. M. Dabiran, and P. I. Cohen, *Surf. Rev. Lett.* **5**, 913 (1998).

[9] S. L. Buczkowski, Z. Yu, M. Richards-Babb, N. C. Giles, L. T. Romano, and T. H. Myers, *Mat. Res. Soc. Symp. Proc.* **449**, 197 (1997).

[10] A. J. Ptak, K. S. Ziemer, M. R. Millecchia, C. D. Stinespring, and T. H. Myers, *MRS Internet J. Nitride Semicond. Res.* **4S1**, G3.10 (1999).

[11] T. D. Moustakas, T. Lei. and R. J. Molnar, *Physica B* **185**, 36 (1993).

[12] H. Riechert, R. Averbeck, A. Graber, M. Schienle, U. Strauss, and H. Tews, *Mat. Res. Soc. Symp. Proc.* **449**, 149 (1997).

[13] N. Grandjean, J. Massies, P. Vennegues, M. Leroux, F. Demangeot, M. Renucci, and J. Frandon, *J. Appl. Phys.* **83**, 1379 (1998).

[14] D. Kapolnek, S. Keller, R. Vetury, R. D. Underwood, P. Kozodoy, S. P. Den Baars, and U. K. Mishra, *Appl. Phys. Lett.* **71**, 1204 (1997).

[15] J. L. Rouviere, M. Arlery, R. Niebuhr, K. H. Bachem, and O. Briot, *Mater. Sci. Eng. B* **43**, 161 (1997).

[16] E. J. Tarsa, B. Heying, X. H. Wu, P. Fini, S. P. DenBaars, and J. S. Speck, *J. Appl. Phys.* **82**, 5472 (1997).

[17] T. Zywietz, J. Neugebauer, M. Scheffler, J. Northrup, and C. G. Van de Walle, *MRS Internet J. Nitride Semicond. Res.* **3**, 26 (1998).

[18] F. Widmann, B. Daudin, G. Feuillet, N. Pelekanos, and J. L. Rouviere, *Appl. Phys. Lett.* **73**, 2642 (1998).

[19] J. M. Van Hove, M. F. Rosamond, R. Hickman II, J. J. Klaassen, C. Polley, A. Wowchak, and P. P. Chow, presented at the 17th North American MBE Conference, Penn State, **G.3** (1998).

[20] L. T. Romano and T. H. Myers, *Appl. Phys. Lett.* **71**, 3486 (1997).

[21] P. M. Bridger, Z. Z. Bandic, E. C. Piquette, and T. C. McGill, *Appl. Phys. Lett.* **73**, 3438 (1998).

[22] M. J. Murphy, Cornell University, private communication.

[23] M. Richards-Babb, S. L. Buczkowski, Z. Yu, and T. H. Myers, *Mat. Res. Soc. Symp. Proc.* **395**, 237 (1996).

[24] J. T. Kobayashi, N. P. Kobayashi, and P. D. Dapkus, *J. Elec. Mater.* **26**, 1114 (1997).

Chapter 5 Gallium Nitride and AlGaN Based High Power Devices

5.1 Introduction

The high critical field for electric breakdown and good carrier transport properties of GaN and SiC have sparked significant interest for applications of these materials in high power, microwave, and high temperature electronics. While both of these compounds can support large electric fields before breakdown, the III-nitrides have several additional advantages over SiC, including the availability of cheap and efficient HVPE growth technology for thick standoff layers and the possibility of GaN/AlGaN heterojunctions [1, 2]. The nitride materials system also benefits from significant technology base support from the optoelectronics industry. Our research has aimed at utilizing the favorable properties of the nitrides to demonstrate high power GaN and AlGaN Schottky diodes and thyristors. To this end we have attempted to lay out the important factors of device design and determine how the design of diodes and thyristors is modified because of the unique properties of the nitrides. We have also experimentally verified the expected value of breakdown field in diode devices and measured the minority carrier diffusion lengths of GaN.

5.2 Nitride materials properties pertinent to high power device design

Two important parameters for high power devices are the electric field at avalanche breakdown (critical field) and the thermal conductivity, as shown in Figure 5.1 and listed in Table 5.1. The critical field determines the minimum depletion layer

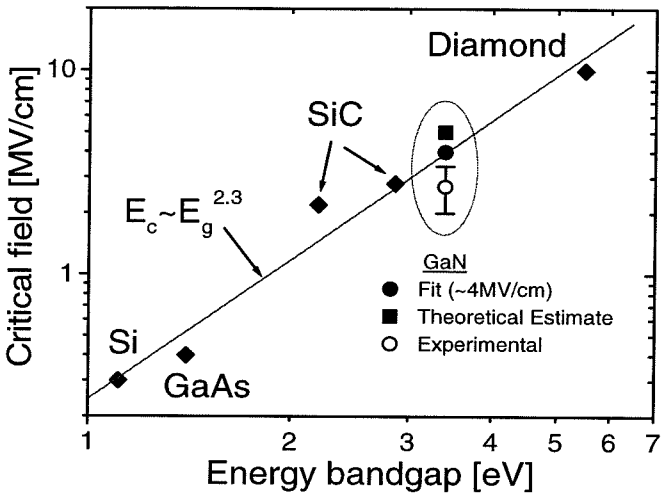

Figure 5.1: The critical field for electric breakdown is shown as a function of energy bandgap. The estimate for GaN based on scaling is marked with a circle ($\sim$ 4MV/cm), the theoretical estimate with a square ($\sim$ 5MV/cm). We have verified that the GaN critical field is at minimum 2.7 ± 0.5 MV/cm (open circle).

Table 5.1: Comparison of the breakdown fields and thermal conductivities of GaN, SiC, Si, and diamond.

Material	Band gap [eV]	Critical Field [MV/cm]	Thermal Conductivity [W/cmK]
Diamond	5.5	10	20
GaN	3.4	$3-5$	1.8 (4.1†)
$6H$-SiC	2.9	2.8	5
$3C$-SiC	2.2	2.2	5
Si	1.1	0.2	1.5

†Theoretical estimate for pure material.

thickness required to support a given reverse voltage, and consequently determines the device ohmic series resistance and thus ON-state voltage. Figure 5.1 shows the critical breakdown field as a function of energy bandgap for Si, GaAs, SiC, GaN and diamond. For many materials, the observed critical field approximately follows a power law dependence as a function of the energy bandgap [2, 3]. Using this scaling property, we can estimate a critical field of 4 MV/cm may be possible for wurtzite GaN, which has $E_g = 3.4$ eV. It makes intuitive sense that the breakdown field should increase with bandgap, since the breakdown mechanism is by impact ionization and generation of electron-hole pairs. The threshold energy to form such a pair is basically the band gap (slightly larger to conserve momentum), energy which a carrier gains as it is accelerated by the electric field over a distance roughly equal to its mean free path, which is determined by scattering from optical phonons and from point and extended defects. A more precise estimate of the breakdown field for GaN can be made when considering band structure to define carrier dispersion. A calculation based on Monte-Carlo derived ionization coefficients for GaN is presented below in section 5.3, which predicts that values for the critical field as high as 5 MV/cm may be possible, depending on the geometry of the device [4].

Since power devices operate at large currents and high voltages, large dissipated power results, and efficient conduction of the resultant heat is important to keep the operating temperature of the device low. The thermal conductivities of Si, SiC, GaN and diamond are listed for comparison in Table 5.1. The potential of diamond for high power applications is clear, provided that a number of technical problems can be overcome, such as efficient n- and p-type doping and development of ohmic contacts. The experimental thermal conductivity of GaN, 1.3-1.7 W/(cm·K), is significantly lower than the theoretically calculated value of 4 W/(cm·K) [5]. However, the measurements were made on less than structurally perfect material, so it is possible that the thermal conductivity may be somewhat higher.

Besides critical field and thermal conductivity, important parameters for design and performance of high power devices are minority carrier diffusion lengths and lifetimes. Minority carrier (both electron and hole) diffusion lengths and lifetimes are

important for bipolar devices, for example, as they directly influence the sensitivity of UV photodetectors [6], the current gain of bipolar transistors [7] and the forward voltage drop of thyristors [2, 7, 8]. Presented in section 5.5 are results of measurements of minority carrier diffusion lengths by electron beam induced currents (EBIC). Carrier lifetimes are inferred from these measurements. The influence of structural defects on the minority carrier properties and the implications for bipolar devices are also discussed below.

5.3 Design of high power diodes and thyristors

5.3.1 High voltage standoff layers

To obtain high OFF-state blocking voltage capability, devices are designed to "stand off" the high voltage across a depleted region. For ideal planar devices, such as diodes and thyristors, the depletion layer is considered to be boundless in two dimensions perpendicular to the applied fields and currents. In this case device design can be done in one dimension, and the relationships between voltage drop, electric field, and charge are easily found for static conditions using Poisson's equation. Ultimately, we desire to know how much voltage can be supported across a given layer. There are two conditions that limit this voltage. If the layer is not thick enough, or the doping concentration too low, then the layer will deplete all the way through. This scenario is termed "punch-through" and the voltage is limited by the thickness of the layer. The other limiting factor is avalanche breakdown, where carriers are accelerated by the electric field and impact ionization creates electron-hole pairs, which are then accelerated in a positive feedback loop. The avalanche-limited breakdown voltage can be calculated for a uniformly doped GaN layer using the ionization integral

$$\int_0^{x_{sc}} \alpha(E(x))dx = 1 \tag{5.1}$$

where x_{sc} is the width of the space-charged layer and $E(x)$ is the electric field as a function of position. Ionization coefficients α for electrons and holes in GaN were

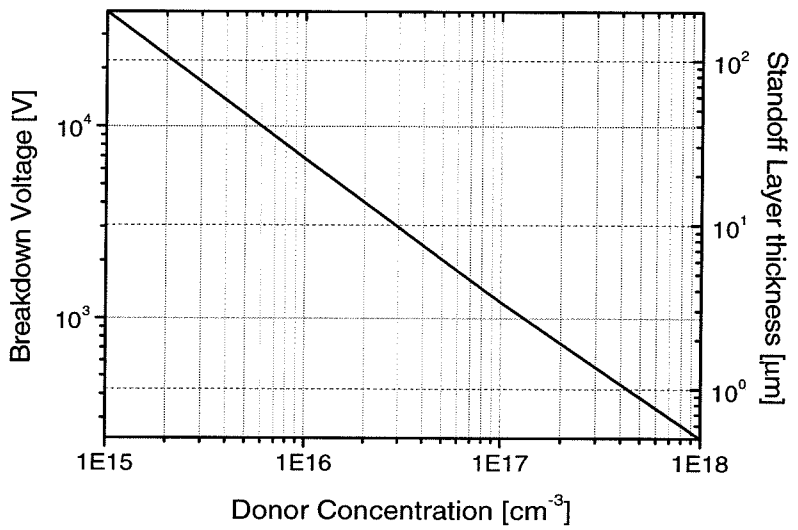

Figure 5.2: The optimum thickness and doping of a GaN standoff layer can be determined for a given voltage specification. The breakdown voltage shown here was calculated using the ionization integral with coefficients taken from Reference [9]. The required layer thickness is at minimum the depletion layer thickness at breakdown. For example, 5 KV Schottky rectifiers can be fabricated using 18 μm thick GaN layers with a doping concentration of approximately $1.3 \cdot 10^{16}\,\mathrm{cm}^{-3}$.

obtained from Reference [9] by fitting calculated values of α at large values of electric field, and are taken to be: $\alpha = 2.9 \cdot 10^8 \cdot \exp(-32.7[\mathrm{MV/cm}]/\mathrm{E})$. The results of this calculation are shown in Figure 5.2. These results can be used to design the standoff layer thickness and doping of diodes and thyristors. For example, 5 KV Schottky rectifiers can theoretically be fabricated using 18 μm thick GaN layers with a doping concentration of approximately $1.5 \cdot 10^{16}\,\mathrm{cm}^{-3}$. At the point of reverse breakdown, the electric field is $5 \cdot 10^6\,\mathrm{V/cm}$, which we can accept as the theoretical maximum value of the critical field. However, the particular device geometry will slightly affect the value of the critical field for electric breakdown.

The advantages of high critical field for power devices are many. As shown in Table 5.2, standoff layer thickness can be made much thinner for a given voltage specification, and the doping concentration can be increased as compared to, *e.g.*, silicon. For these reasons, the series resistance of the device can be made much smaller,

Table 5.2: Comparison of GaN, SiC, and Si as standoff layer material, designed to withstand 5000 V. We see the obvious advantages of GaN for high voltage applications. The standoff layer thickness can be made relatively smaller and the doping relatively higher than in other candidate materials, resulting in reduced series resistance and higher efficiency. The $Al_xGa_{1-x}N$ alloys should offer even higher performance.

Material	Band gap [eV]	Doping [cm^{-3}]	W [μm]
GaN	3.4	$1.5 \cdot 10^{16}$	18
6*H*-SiC	2.9	$2.3 \cdot 10^{15}$	50
3*C*-SiC	2.2	$5.3 \cdot 10^{14}$	100
Si	1.1	$1.3 \cdot 10^{13}$	650

thus also dissipated power, so efficiency is increased as critical field is increased. This is one of the major reasons why the wide band gap semiconductors show such good promise for high power applications.

The minority carrier diffusion lengths and lifetimes also affect many device properties, including the allowable current density, device operating frequency and temperature, the forward resistance for bipolar devices, and switching characteristics of thyristors. More details are presented in References [2, 10] and summarized below.

5.3.2 Power dissipation and thermal breakdown

Without considering carrier modulation effects (see section 5.7), the power dissipated by a bipolar device has components both in the ON and OFF state. Assuming 50% duty cycle, the power dissipated is given by $P_D = 1/2A(V_{ON}J_{ON} + R_{ON}J_{ON}^2 + J_sV_B)$ where V_{ON}, J_{ON} and R_{ON} are threshold voltage, current density and differential series resistance in the ON state, and J_s is reverse leakage (saturation) current density. The device resistance is given by $R_{ON} = W/(qN_d\mu_n)$. The forward drop voltage in the thyristor is inversely proportional to the hole lifetime in the standoff layer and directly proportional to the square of the standoff layer thickness, or $V_{ON} \propto W^2/\tau_h$ [7]. Note that both R_{ON} and V_{ON} are lower when thickness W is lower, which is a case for the high bandgap materials.

The maximum current density is limited by the ability of the device (and its

housing) to dissipate power while keeping the device operating temperature lower than the maximum allowed. The temperature difference between the device and ambient under steady state conditions is determined by the product of the total thermal resistivity and the total power dissipated by the device:

$$\Delta T = T_m - T_0 = (d/\kappa A + \theta_{ca})P_D. \tag{5.2}$$

The total device to ambient thermal resistivity is a sum of the resistivities of the device ($d/\kappa A$) and case to ambient (θ_{ca}) thermal resistivities. Figure 5.3A shows the dependence of the device temperature as a function of current density (obtained from Equation 5.2) for several hole lifetimes in the range between 2 and 20 ns, assuming 50% duty cycle. We can see that maximum current density at a particular hole lifetime is limited by thermal breakdown, when power cannot be efficiently dissipated.

5.3.3 Operating frequency

The maximum operating frequency of the thyristor is limited by the time required to switch the device from the ON to the OFF state, which requires charges in the standoff layer to be recombined, and depends on the hole lifetime. Figure 5.3B shows the maximum operating frequency of a 20 μm $Al_{0.2}Ga_{0.8}N$ thyristor as a function of the hole lifetime. Much higher operating frequencies can be expected for the Schottky rectifier because it is a unipolar device and not limited by recombination times.

5.4 High voltage GaN Schottky diodes

In order to verify the potential and demonstrate the promising abilities of GaN for high power devices, Schottky diodes were fabricated on GaN layers and characterized by current-voltage analysis. There have been many reports of GaN Schottky diodes using a variety of elemental metals including Pd and Pt [11, 12], Au, Cr, and Ni [13, 14], and Mo and W [15], but these reports focus on physics and metallurgy of the contacts rather than electric breakdown in the GaN material. More details on the

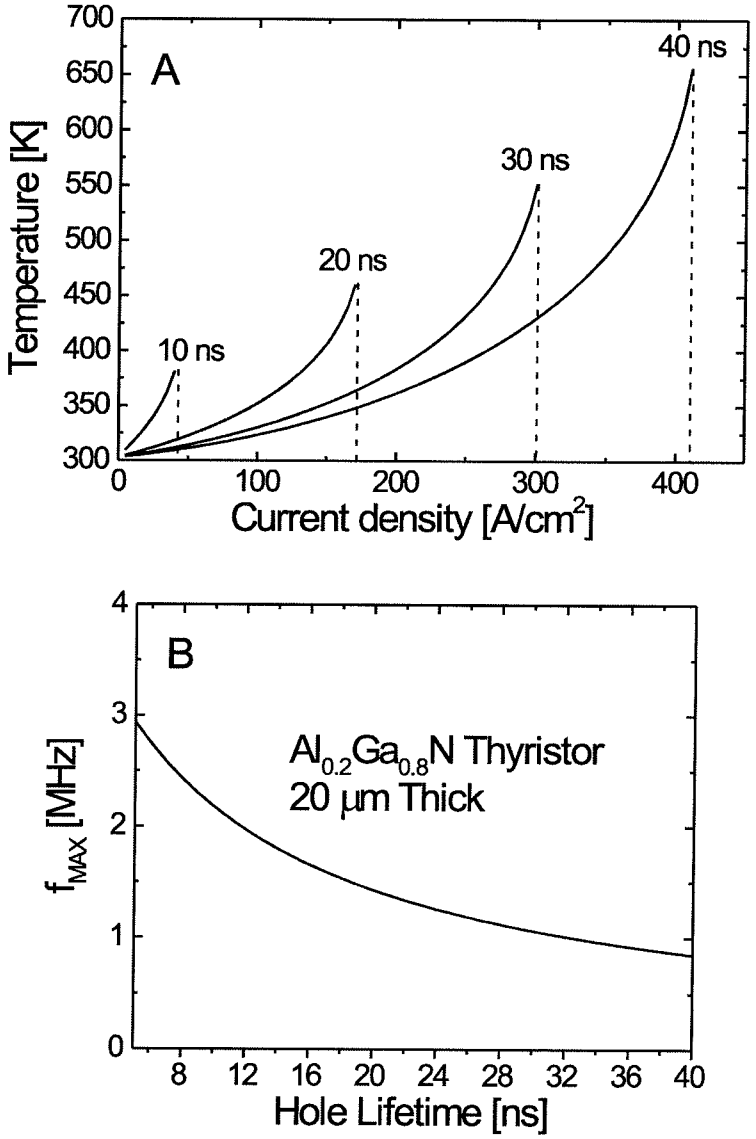

Figure 5.3: A) Temperature of the device as a function of current density, for different values of minority carrier lifetime. The ambient temperature is taken to be 300 K. B) Maximum operating frequency of the thyristor, limited by recombination time for a 20 μm AlGaN thyristor.

metal-GaN contact technology can be found in Reference [16] and in chapter 6. In this section, the fabrication of Schottky diodes on $1\,\mu$m thick MBE layers, as well as on $8-10\,\mu$m thick HVPE-grown GaN layers is described, with focus on the measurement of critical field.

5.4.1 Diodes on HVPE GaN

The thicker $8-10\,\mu$m layers were grown by HVPE on sapphire. As is the case with HVPE epilayers of this kind, the electron concentration changes with the distance from the GaN/sapphire interface. Hall measurements on a series of HVPE GaN films of varying thickness ranging from 0.07 to 9.2 μm, fit to a two layer model [17, 18, 19, 20] indicate that the HVPE GaN films consisted of a low conductivity, low electron concentration, thick top layer on a very thin ($<$ 100 nm), highly conductive, high electron concentration (degenerate) bottom interface layer. The electron concentrations and mobilities in the thin interface layer and thick upper layer were found to be $2\cdot10^{20}\,\mathrm{cm}^{-3}$ and $35\,\mathrm{cm}^2/\mathrm{Vs}$, and $2\cdot10^{16}\,\mathrm{cm}^{-3}$ and $265\,\mathrm{cm}^2/\mathrm{Vs}$ respectively. The interface layer is therefore approximately three orders of magnitude more conductive than the thick upper layer. Capacitance-voltage (C-V) measurements performed on the $9.2\,\mu$m thick samples indicated a the net donor concentration near the film surface of $(2\pm1)\cdot10^{16}\ \mathrm{cm}^{-3}$, consistent with the two layer model. (For more details concerning the highly conductive interface layer, see Reference [4].) The importance of this conductive interfacial layer will be described below.

Several device and contact geometries were fabricated, including lateral, mesa, and metal overlapping oxide devices as shown in Figure 5.4. Preferred would have been to make a back ohmic contact to the GaN film, as this would more closely approximate the planar geometry, but back contacts to GaN are not available at this time due to substrate issues. Fortunately, the highly conductive layer described above goes a long way towards approximating a planar geometry, which is crutial for field control and current density uniformity.

Prior to metal deposition, the GaN surfaces were cleaned with organic solvents,

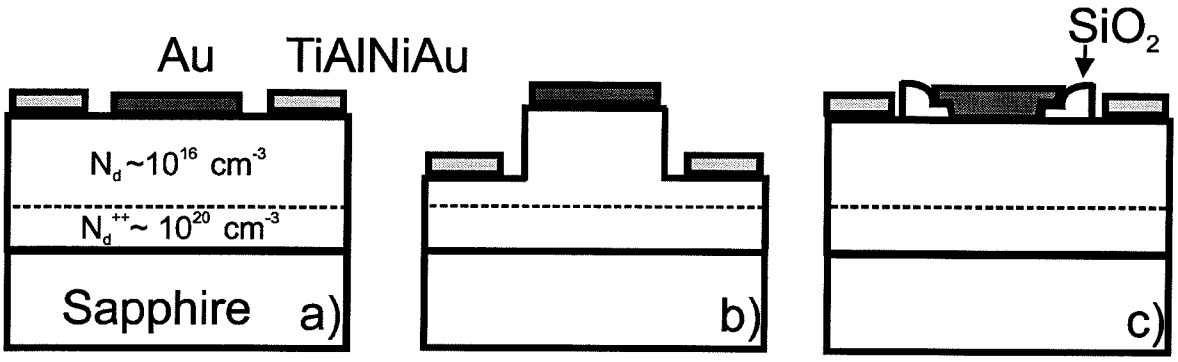

Figure 5.4: Different device geometries for GaN Schottky diode rectifiers. The thicknesses of the layers of different electron concentration are not drawn to scale. a) Lateral contact Schottky rectifier, b) mesa device, which offers lower resistivity since ohmic contacts are deposited closer to the high conductivity interface layer, and c) Lateral diodes processed with metal overlapping SiO_2.

dipped in HF:H_2O (1:10), rinsed in deionized water, and blown dry with nitrogen gas. Following cleaning, gold (1500Å) was sputter deposited and patterned to produce Schottky contacts following the procedure described in chapter 6. Ti/Al/Ni/Au (150Å/1500Å/100Å/1000Å) was deposited to produce ohmic contacts. On some devices, large area Au metallization was used as a low resistivity contact instead. The mesa edge termination was produced by chemically assisted ion beam etching, using Xe ions accelerated with 1000 V, and 25 sccm of Cl_2 flow [2, 10]. For the oxide overlap devices, SiO_2 was sputtered using a SiO_2 RF magnetron target and 10 sccm of O_2 flow, and then patterned using wet etch lithography. Current-voltage (I-V) measurements were taken with a Keithley 237 high voltage source unit and with a HP 4156A precision semiconductor parameter analyzer. The Keithley 237 was used for high voltage measurements while the HP 4156A was used to determine the Schottky barrier height and for I-V measurements up to 100 V.

Current-voltage (I-V) characteristics for the fabricated devices are shown in Figures 5.5 and 5.6. The reverse breakdown voltages observed were in the range between 250 V and 450 V and exceeded 450 V in several devices. The variation in the device breakdown voltage may be attributed to non-uniformities in the electron concentration and to processing. The Au Schottky barrier heights obtained from the I-V measurements varied between 1.1 eV and 0.8 eV. The ideality factor of the diodes

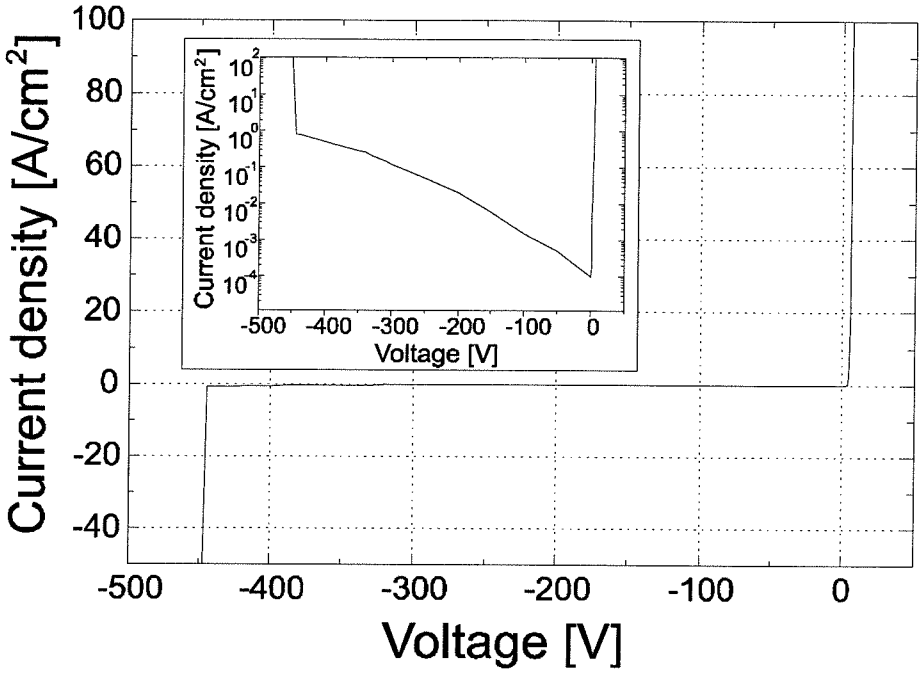

Figure 5.5: *I-V* curve taken with Keithley 237 high voltage source measure unit for the high voltage rectifier displaying large standoff voltage. Scan by Z. Bandić.

ranged between 1.6 and 4. In the case of the lateral diode, the ON-state voltage was 5 V for a current density of 100 A/cm^2. Large ON-state voltages are a consequence of both the large ohmic contact resistances and the low electron concentration of the upper layer. The series resistance of the device is significantly affected by the presence of the highly conductive interface layer. This layer "shorts" the conduction path, so that the series resistance consists mainly of the ohmic contact resistance, the resistance of the $8 - 10\,\mu$m thick layer between ohmic contact and the highly conductive layer, and the resistance of the $8 - 10\,\mu$m thick layer between the highly conductive layer and the Schottky contact. Without the highly conductive interface layer, the device series resistance would be determined by the distance between ohmic and Schottky contacts, which was not observed to be the case.

To reduce the series resistance we etched $5\,\mu$m of the $8 - 10\,\mu$m top layer and deposited ohmic contacts closer to the more conductive interface layer (Figure 5.4b). This reduced the ON-state voltage from 5 V to 4.2 V at a forward current density of 100 A/cm^2. However, as can be observed from Figure 5.6, the reverse leakage current

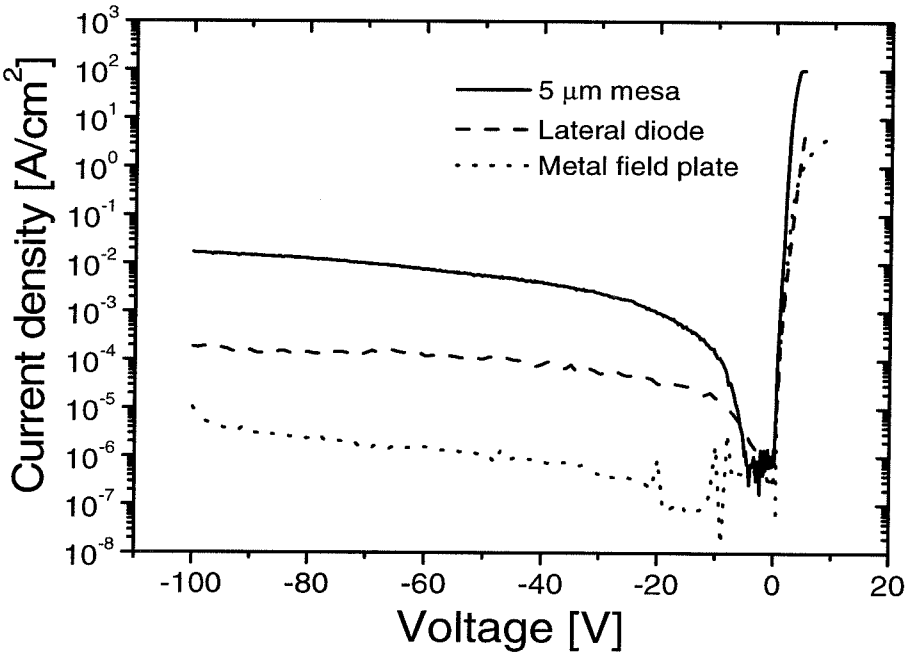

Figure 5.6: Current-voltage curves for the three device geometries discussed above. In all three data sets the Schottky contacts were squares with 100 μm sides. The metal overlapping oxide (metal field plate) geometry allows the least leakage current, less than 10^{-5} Amps per cm^2. (I-V measurements by Z. Bandić.)

increased to approximately $10^{-2}\,\mathrm{A/cm^2}$, probably due to the etch damage of the mesa walls.

The electric field crowding at the edges and corners of the Schottky contact (departures from the ideal planar device) will reduce the effective barrier height as measured by I-V and increase the reverse leakage current. This can also lead to premature breakdown due to nonuniform current spreading and excessive heating of the device, as shown in Figure 5.7. To improve the Schottky contacts, we fabricated metal overlap contacts using SiO_2 as an insulator [8]. The edge of the Schottky contact overlaps sputtered SiO_2, thereby reducing electric field crowding at edges and corners. In this case, as can be observed from Figure 5.6, measured saturation current at a reverse bias of 100 V was approximately $10^{-5}\,\mathrm{A/cm^2}$, an improvement of two orders of magnitude when compared to the saturation current density of diodes with lateral contacts.

Using the formula for a punch-through diode [8], $V_{PT} = E_{CR}W - qN_dW^2/2\epsilon_0\epsilon_r$, and substituting measured values, we find from the experimental results the critical field for electric breakdown to be $(2.2 \pm 0.7) \cdot 10^6\,\mathrm{V/cm}$. This is in close agreement with what was presented in section 5.2 and with recent experimental and theoretical predictions [9, 21]. Since our devices suffered from premature corner and edge breakdown (Figure 5.7), and since device geometries were not fully optimized, it can be concluded that this value of critical field is only a lower limit.

One of the most important consequences of this study is the experimental demonstration of a high critical field for electric breakdown in GaN. The demonstrated high critical field indicates the feasability of GaN as a material for a variety of unipolar and bipolar devices [2, 10]. Furthermore, assuming that the critical field for electric breakdown approximately scales as the square of the bandgap, even higher critical fields can be expected for AlGaN. Although ON-state voltages demonstrated in this work are rather high, estimates based on the Richardson equation show that the ON-state voltage for a current density of $100\,\mathrm{A/cm^2}$ can be as low as $1 - 2\,\mathrm{V}$. However, it is necessary to improve Schottky contact edge terminations, reduce ohmic contact resistances and achieve more precise control over doping.

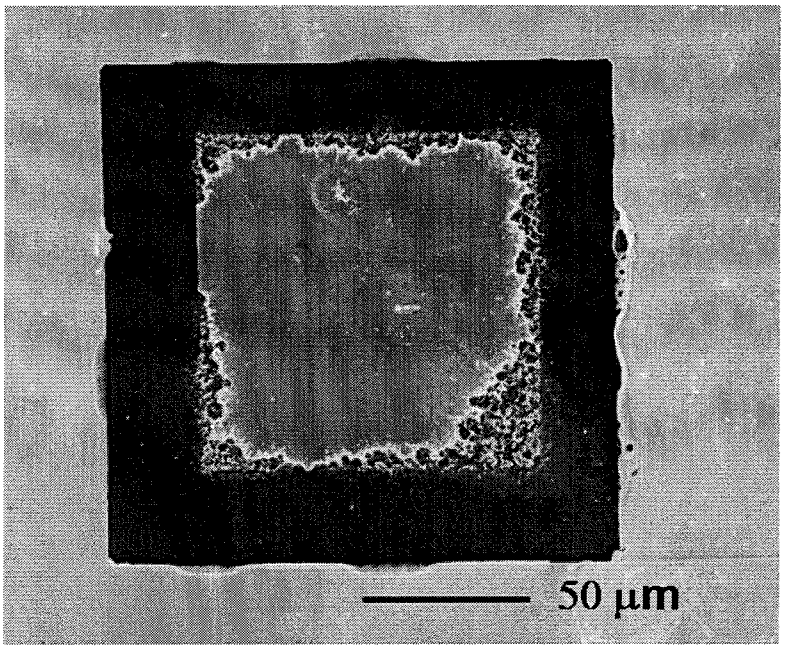

Figure 5.7: SEM photo of the Schottky contact of a diode after breakdown. The melted Au at its edges and corners indicates premature corner and edge breakdown.

5.4.2 Schottky diodes on MBE-grown GaN

Schottky diodes were also fabricated using a MBE-grown layer structure of 1.2 μm undoped GaN over 1 μm of n-GaN:Si doped to $\sim 5 \cdot 10^{18}$ cm^{-3}, the surface of which is shown in Figure 3.5A. Square Au pads were used as rectifying contacts and a large area grid electrode was used for ohmic contact. The current voltage curve for a typical device is shown in Figure 5.8. We see that reverse breakdown does not occur until almost 40V. Assuming that this voltage lies primarily across the semi-insulating layer and treating the device as a punch-through diode [7], an estimate of the critical field is approximately 0.35×10^6 V/cm for a planar junction. However, as mentioned above, the square Au pads used as Schottky contacts suffer greatly from field crowding effects at the edges and corners where the equipotentials become spherical [8]. It is not unreasonable to assume that in these regions the electric field is at least ten times the value stated above and that reverse voltage is limited by breakdown at the edges. Nevertheless, the MBE-grown diodes supported far less voltage than the HVPE grown devices. This discrepancy can simply be attributed to the much higher defect density (up to 1000 times higher) in the MBE GaN. Also of note is that the MBE diodes could

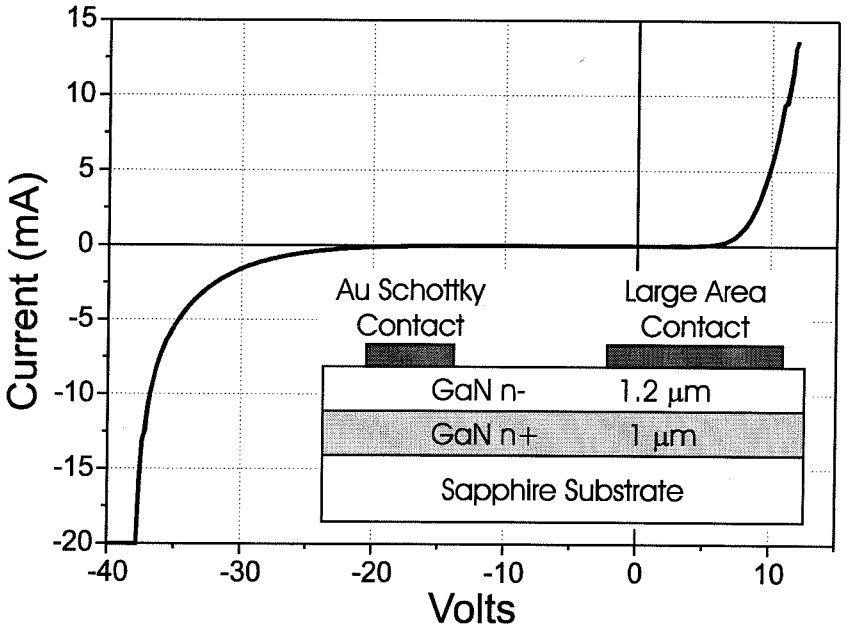

Figure 5.8: Current-Voltage curve for Schottky diode Au/n$^-$-GaN/n^+-GaN structure. Avalanche multiplication causes breakdown at nearly 40 Volts in reverse bias, and supports an electric field of at least $3 \cdot 10^5$ V/cm. The forward voltage drop can be reduced by improving the ohmic contact and reducing the film defect density, as edge dislocations can induce space charge regions which almost completely deplete the film.

withstand large forward currents without damage. For 90 μm square pads, reliable operation was observed at forward currents up to 20 kA/cm^2, at which point the Au metallization melted.

The forward portion of the I-V curve for the MBE-grown diodes is rather non-ideal. The turn-on voltage is quite high, over 5 V. While non-optimum ohmic contacts, as well as native oxide at the Schottky-semiconductor interface, can impede current flow in this region, it is suspected that other effects are at play here as well, involving edge dislocations in the films [23, 22]. Edge dislocations in GaN have been shown to be electron traps (discussed further in section 5.6.3). The charged dislocations then deplete the regions surrounding them, and if the dislocation density is high enough, can effectively deplete the entire film. This can easily be the case if donor densities are low enough. In the case of the MBE-grown Schottky diode, the edge dislocation density is believed to be as high as 10^{11} cm^{-2} while the donor density is less than 1×10^{16} /cm^3. These conditions are suspected to give rise to a completely depleted film, so the forward current for the device shown in Figure 5.8 is suspected to be severely space charge limited.

5.5 Electron beam induced current measurements

Since minority carrier diffusion lengths and lifetimes play such an important role in high power devices, we endeavored to measure these values for GaN using electron beam induced current (EBIC) measurements implemented in a scanning electron microscope (SEM). These measurements were carried out by Z. Bandić [24, 25].

5.5.1 Device preparation

The samples used were either unintentionally doped (UID), n-type, or p-type doped GaN grown by MOCVD, MBE or HVPE on sapphire. Unintentionally doped samples were n-type as grown. Intentionally doped n-type samples were doped with Si, while p-type samples were doped with Mg. EBIC measurements were carried out on Schottky diodes fabricated from these GaN films. Prior to device processing, the

GaN surface was cleaned with organic solvents, and then dipped in $HF : H_2O(1:5)$. Contact metals were sputtered (see chapter 6) and patterned to produce Schottky contacts as well as large-area ohmic contacts. In the case of UID and n-type GaN, Au was used as a Schottky contact, while Ti/Al was used as an ohmic contact. For p-type GaN, a Ni/Au metalization scheme was used for the ohmic contact, while Ti/Au was used for the Schottky contact. The samples to be measured were fixed to a 24-pin die package, wire-bonded with Au wires, and transfered to the SEM.

5.5.2 Measurement setup

EBIC measurements on these samples were carried out in a JEOL 6400V scanning electron microscope, using either GW Electronics pre-amplifier model 103B, followed by GW Electronics Specimen Current Amplifier model 31, or Keithley 486 picoammeter. The experimental setup is shown in the schematic of Figure 5.9. When high voltage electrons are injected into the semiconductor, electron-hole pairs are generated. Due to the large concentration of holes in p-type samples (or electrons in UID or n-type samples) compared to the generated electron-hole concentration, only minority carriers are effectively generated, assuming low beam currents. The circuit is closed with an ohmic contact on the semiconductor surface, and minority carriers which diffuse into the depletion region near the Schottky contact generate an induced current. The current follows the relation $I = kx^{\alpha}exp(-x/L_m)$ where α ranges from $-1/2$ in case of negligible surface recombination to $-3/2$ in case of large surface recombination. L_m is the minority carrier diffusion length and x is the distance between the Schottky contact and the injection spot [26]. The minority carrier diffusion length is obtained by fitting the measured $I(x)$ dependence to the theoretical equation. We assume small surface recombination corresponding to $\alpha = -1/2$ since the GaN samples analyzed here have good photoluminescence efficiency. Even if infinite surface recombination is assumed, the quantitative values do not change more than 20-25%, since this expression is dominated by the exponential term. The electron beam current was kept low enough so that effectively only minority carriers were injected. The

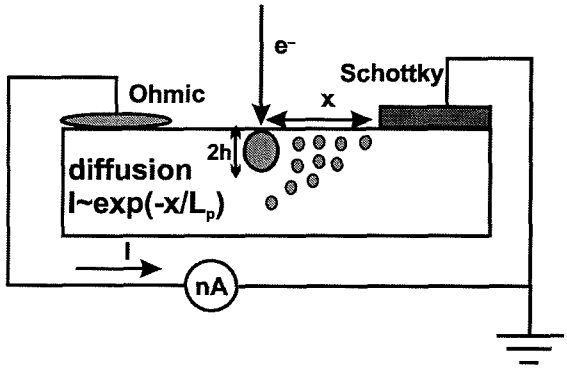

Figure 5.9: Experimental setup for EBIC measurement. Injected minority carriers diffuse to the Schottky contact, inducing current flow in the circuit.

data was collected at distances x larger than the electron range in the material and larger than twice the diffusion length, so that the approximate expression above for the induced current is correct [26]. The minority carrier lifetime, τ_m, can then be obtained from the Einstein relationship $L_m^2 = D_m \tau_m$, where the diffusivity, D_m, can be calculated from the minority carrier mobility using $D_m = (kT/q) \cdot \mu_m$.

5.5.3 EBIC results

Typical examples of the line scan profiles of the EBIC as a function of distance from the edge of the Schottky contact in the case of MOCVD-grown UID and p-type GaN is shown in Figures 5.10a and 5.10c respectively. The EBIC line scan profiles are shown superimposed on the secondary electron images of the edge of the Schottky contact. Corresponding AFM images are shown in Figures 5.10b and 5.10d. Calculated minority carrier diffusion lengths, obtained after averaging over the range of beam currents and different measurement positions on the sample, are $(0.28 \pm 0.02)\,\mu$m for holes, and $(0.20 \pm 0.05)\,\mu$m for electrons. A typical data set used to extract the diffusion length, in the case of electrons as minority carriers, is shown in Figure 5.11. We obtained diffusivities of $D_p = 0.12\,\mathrm{cm}^2/\mathrm{s}$ and $D_n = 2.6\ \mathrm{cm}^2/s$, for holes and electrons respectively, from Hall measurements of the mobility. Using these values, we estimated a hole lifetime as a minority carrier of approximately 7 ns, and an electron lifetime as a minority carrier of approximately 0.1 ns. A summary of our

Table 5.3: Summary of the EBIC measurements. The hole diffusion lengths in each row of the table are an average over a range of beam currents and different measurement positions on the samples.

Sample	n [cm^{-3}]	Diffusion length [μm]	Dislocation density [cm^{-2}]
n-MOCVD	10^{17}	0.28 ± 0.02	$(2-5) \cdot 10^9$
n-MBE	10^{16}	0.22 ± 0.03	$5 \cdot 10^9$
n-HVPE	10^{16}	$1-2$	10^8
n-MOCVD	10^{17}	0.20 ± 0.05	$5 \cdot 10^9$

Table 5.4: Summary of the measured, estimated and calculated hole diffusion lengths and lifetimes from the published literature.

Material	Diffusion length [μm]	Lifetime [ns]	Reference
GaN		$8-10$	[33]
InGaN/GaN MQW		$15-20$	[31]
GaN	0.1		[6]
InGaN/GaN MQW		$1-3$	[30]
GaN	≤ 0.25		[34]
GaN	0.05		[28]
GaN	$1.2-3.4$	15	[29]
GaN	$1.7-2.5$		[35]

results for GaN samples, including samples grown by MBE and HVPE is shown in Table 5.3. HVPE-grown samples had smallest dislocation density of approximately 10^8 cm^{-2} as observed by AFM [27], and the measured diffusion lengths were highest, in the $1-2\,\mu$m range.

Measurements and calculations of minority carrier (hole) diffusion lengths and lifetimes obtained from the published literature are shown in Table 5.4, for the case of GaN and InGaN/GaN multiple quantum wells (MQW). We can observe variation in measured (or estimated) diffusion lengths in the range between $0.05\,\mu$m [28], and $3.4\,\mu$m [29]. The variation in hole lifetime is smaller, and ranges from 1 ns [30], to 20 ns [31]. Variation in these values is attributed to the variation in structural properties of GaN.

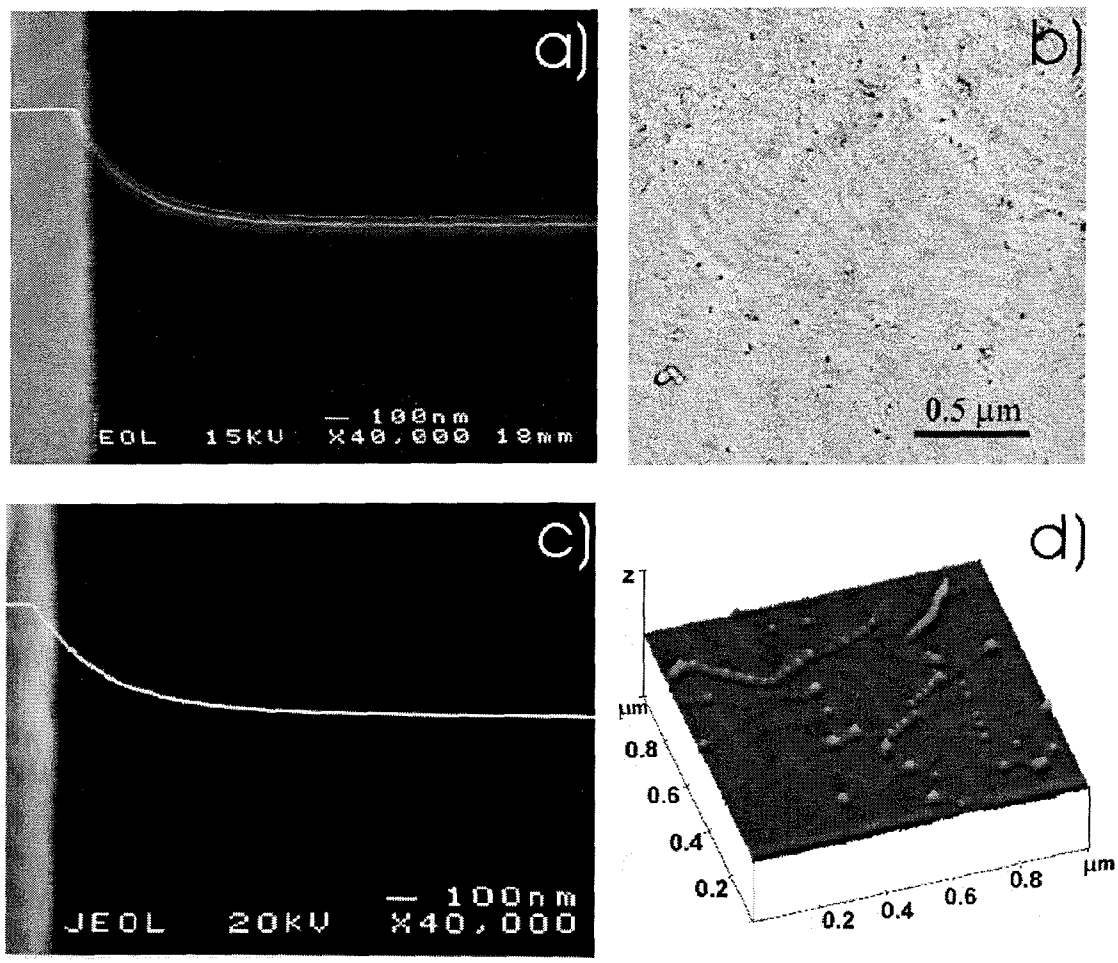

Figure 5.10: a) Line scan profile of induced current (EBIC) superimposed on the secondary electron image of the edge of the Au Schottky contact, for the MOCVD grown UID GaN. The electron beam voltage and current were 15 KV and 0.4 nA respectively. b) Filtered AFM tapping mode phase image of the MOCVD-grown UID sample shown in a). Small pits at the boundaries of nearly defect-free crystalline grains indicate that the grain boundaries are decorated with linear dislocations. The grains range from 0.3–0.5 μm in size. c) The line scan profile of induced current near the Ti/Al contact for the MOCVD-grown p-type GaN sample. The electron beam voltage and current are 20KV and 0.5nA in this case. d) AFM scan of the p-type MOCVD sample shown in c) which clearly shows the dislocation-induced pits at the grain boundaries. The range of grain sizes in this sample is 0.2–0.6 μm. (EBIC scans by Z. Bandić. AFM by P. Bridger.)

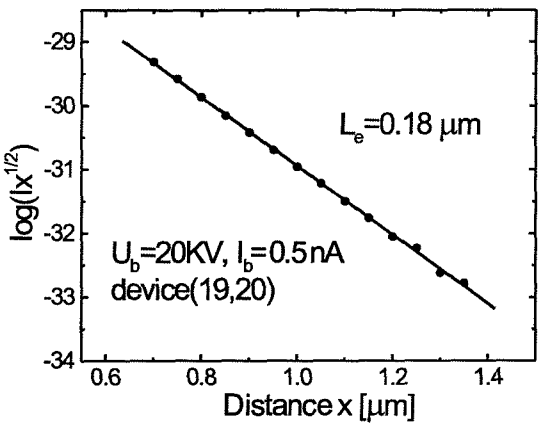

Figure 5.11: Typical data used to extract electron minority carrier diffusion length. (Z. Bandić.)

5.6 Correlation of minority carrier lifetimes with structural defects

5.6.1 Experimental observations

The samples analyzed by EBIC were also observed with atomic force microscopy (AFM), which is useful in determining the defect structure of the films. As with the MBE-grown films presented in chapter 3, small pits were observed on the surfaces of the HVPE and MOCVD samples also [36]. It was considered that the dislocations might be limiting the minority carrier diffusion lengths observed, in a fashon similar to the effect of mobility reduction by charged dislocations. In this case, the dislocations may act as recombination centers. On most of the AFM images, we observed that the dislocation-induced pits are located at boundaries between otherwise defect-free grains. From the AFM images in Figures 5.10b and 5.10d we see that the measured diffusion lengths (in the range of $0.2 - 0.3\,\mu$m) are smaller than the average defect-free grain size, which ranges between $0.3\,\mu$m and $0.5\,\mu$m. If recombination does occur at linear dislocations [34], it would limit minority carrier diffusion to sub-grain-size length, in agreement with our experimental observation. Indeed, the samples with the fewest dislocations (and largest mean grain size), the HVPE-grown samples, were measured to have by far the largest hole diffusion lengths. The HVPE samples (AFM

not shown) were observed to have a dislocation density of approximately $10^8\,\mathrm{cm}^{-2}$, and a hole diffusion length of $1-2\,\mu$m. This trend seems to support the proposition that dislocations act as recombination centers.

5.6.2 Model for minority carrier lifetime limited by dislocation density

If recombination is the limiting mechanism for minority carrier diffusion length and lifetime, then an analytical model can be derived which connects the minority transport properties with the structural properties of the film. Models of this type have been previously derived in the case of GaP [37]. If dislocations are assumed to be distributed in a hexagonal array, then the dislocation density can be expressed as $N_{dd} = 1/(\pi r_s^2)$, where $2r_s$ is the distance between two first-neighbor dislocations (see Figure 5.12b). Dislocations are assumed to have a finite core diameter $2r_0$. The minority carrier concentration (holes, for example) is obtained by solving the two-dimensional Poisson equation for the minority carrier concentration p: $D_p\nabla^2 p = \partial p/\partial t$, with the boundary conditions: *(i)* $p|_{r=r_0} = 0$, and *(ii)* $\partial p/\partial r|_{r=r_s} = 0$. Boundary condition *(i)* reflects an infinite recombination velocity at the dislocation, while condition *(ii)* is an approximation to the periodic boundary condition [37]. After solving the Poisson equation in cylindrical geometry, the minority carrier lifetime τ_{scat} is obtained: [37]

$$\tau_{scat} = \frac{1}{2\pi D_p N_{dd}}\left(ln\frac{1}{r_0\sqrt{\pi N_{dd}}} - 0.57\right) \tag{5.3}$$

If the minority carrier lifetime without considering the effect of dislocations is given by τ_0, then the total minority carrier lifetime can be written $\tau_p^{-1} = \tau_0^{-1} + \tau_{scat}^{-1}$. Hole lifetime and corresponding diffusion length, obtained from the model, are shown in Figure 5.12a as a function of dislocation density. In this calculation, we used the measured value for hole diffusivity $D_p = 0.12\,\mathrm{cm}^2/\mathrm{s}$ obtained from MOCVD samples, and used a dislocation core radius of $r_0 = 30$ nm which is typically observed by AFM.

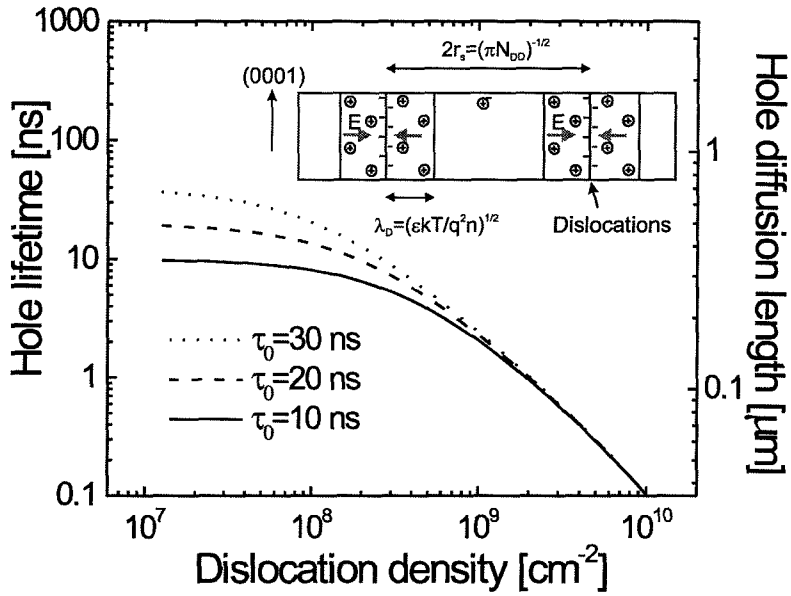

Figure 5.12: Hole lifetime and diffusion length is plotted as a function of dislocation density, assuming a uniform distribution of dislocations (see inset). The data assumes a diffusivity of 0.012 cm^2/s as estimated from Hall mobility measurements of MOCVD samples. The non-restricted hole lifetime τ_0 (no dislocations) is used as an parameter in the plot. The inset is a cross sectional side view diagram showing negatively charged dislocations in a GaN layer with surrounding space charge regions.

Clearly, this model predicts that decreasing the dislocation density, and therefore improving the structural quality, should improve minority carrier lifetime. This is in qualitative agreement with the experimentally observed increase in hole diffusion length for samples which have smaller dislocation density.

5.6.3 Linear dislocations as recombination centers

As was discussed in section 3.6.1, dislocations with an edge component can act as deep acceptor traps [22, 23, 38]. The edge dislocations then become negatively charged and induce a space charge region around themselves (see inset of Figure 5.12) with a radius approximately equal to the Debye length, $\lambda_D = \sqrt{\epsilon_0 \epsilon_r k_B T/e^2 n}$, where k_B is the Boltzmann constant, T is the temperature and n is the electron concentration. The negative charge creates an electric field oriented towards the dislocation. Therefore, holes as minority carriers would be attracted by this electric field, and could recombine with the trapped electrons at the linear dislocation. The hole diffusion length will

then be limited by the free space between dislocations given by $2r_s = 2/\sqrt{\pi N_{dd}}$, and by the Debye length which defines the region of electric field which attracts holes to the recombination center:

$$L_p \sim 2r_s - \lambda_D = \frac{2}{\sqrt{\pi N_{dd}}} - 2\sqrt{\frac{\epsilon_0 \epsilon_r k_B T}{e^2 n}} \tag{5.4}$$

The hole diffusion length would thus depend on both dislocation density and electron concentration in n-GaN.

5.7 Implications of minority carrier diffusion lengths and lifetimes on performance of bipolar devices

Minority carrier lifetimes and diffusion lengths significantly influence design and performance of bipolar devices. In this section, the influence of hole lifetime on the forward voltage drop in GaN-based p-n-p-n thyristor switches is considered.

When a thyristor (p-n-p-n structure) is in the ON-state, the free electron and hole concentrations in the intermediary (middle) p and n layers are comparable to or greater than the donor and acceptor concentrations in those layers. In this case, the middle layers behave in a similar fashon to the insulating layer in a p-i-n structure. The forward voltage drop can then be estimated using an analysis similar to that for a p-i-n diode [7, 8]. Of the two intermediary layers, the voltage drop will be predominantly across the thicker n-type standoff layer in a thyristor, and will be approximately proportional to the reciprocal of minority carrier lifetime in the standoff layer. The voltage drop is also directly proportional to the square of the standoff layer thickness: $V_{ON} \propto W^2/\tau_p$ [7]. As the standoff layer thickness becomes significantly larger than the hole diffusion length, the ON-state voltage increases more rapidly with the decrease in the lifetime [8]. The dependence of the ON-state voltage in the case of the thyristor based on a GaN standoff layer is shown in Figure 5.13A

as a function of device breakdown voltage and hole lifetime. Since the minority carrier diffusion lengths are relatively small for wide band gap materials, wee see that V_{ON} increases with thickness W. Figure 5.13B shows the dependence of the ON-state voltage as a function of temperature and hole lifetime for a 3 kV thyristor which uses a 9.8 μm thick GaN layer. The calculations assume an electron mobility of $960 \cdot (T/300)^{-1.84}\,\mathrm{cm}^2/\mathrm{Vs}$ [39], and assume an electron to hole mobility ratio of ~ 10. The measured values for hole diffusion length (by EBIC) given in Table 5.3 and Table 5.4 indicate that reasonably low forward drop can be expected for devices with voltage specifications below 5 kV.

5.8 Summary and conclusion

Utilizing the favorable materials properties of GaN and $Al_xGa_{1-x}N$ in the context of high power switches and rectifier devices, the design parameters of standoff layers in Schottky diodes and thyristors were derived. Based on an analysis of Monte-Carlo-derived impact ionization coefficients for GaN, it was found that the critical field for electric breakdown can be as high as 5×10^6 V/cm in GaN and even higher in $Al_xGa_{1-x}N$. Due to the higher breakdown fields, standoff (depletion) layer thicknesses can be made much smaller, as compared to Si-based power devices, for the same voltage specification. The doping concentrations could likewise be increased. The thinner layers, in combination with the higher doping, leads to much reduced ON-state series resistance for a given device. For these basic reasons, it is estimated that 5 kV GaN diodes and thyristors can be made using only 18 μm thick layers, with a doping concentration of $\sim 1.3 \cdot 10^{16}$ cm^{-3}.

To test and verify the high breakdown field capability of GaN, Schottky diodes were fabricated using 8-10 μm thick GaN layers grown by HVPE. The gold Schottky diodes withstood $450 - 750$ V in reverse bias, corresponding to breakdown field of $(2.2-2.7)\cdot 10^6$ V/cm in an ideal planar geometry device. The lateral geometry used in this case, however, with lack of suitable edge termination, resulted in field crowding at the edges of the Schottky electrode. Because of this, these devices displayed premature

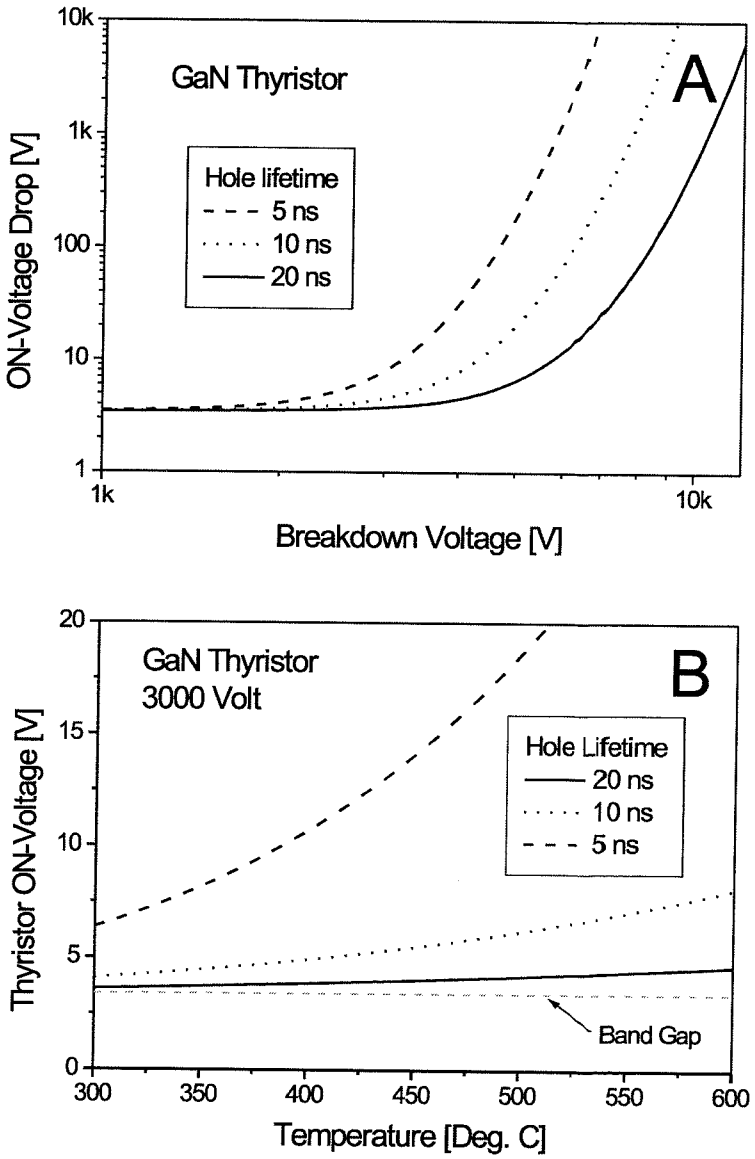

Figure 5.13: A) ON-state voltage for a GaN thyristor as a function of maximum reverse voltage capability. As the standoff layer thicknesses (which depend on voltage rating) become larger than the hole diffusion length, the ON-state voltage increases dramatically. B) ON-state voltage as a function of temperature and hole lifetime for a 3 kV GaN thyristor with 9.8 μm thick standoff layer. Small forward drop for high voltage thyristors requires long diffusion lengths and minority carrier lifetimes.

edge breakdown, so the 2.7 MV/cm value should be taken as a lower limit. Some processing attempts at edge termination geometries were carried out, but no increase in standoff voltage could be obtained, although reverse leakage (saturation) current varied greatly with the processed device geometry, achieving minimum reverse current density of 10^{-5} A/cm^2 at reverse bias of 100 V with metal overlapping oxide Schottky contacts. To really achieve high quality devices, guard ring structures are required which have characteristic dimensions on the micron scale and diffused dopant ring profiles, which is a difficult undertaking. The forward voltage at a current density of 100 A/cm^2 was 4.2 V, somewhat higher than was estimated from the film resistivity, likely due to poor ohmic contacts on the very lowly doped material.

Other nitride materials properties besides breakdown field are of interest for design of high power devices. The minority carrier lifetime and diffusion length govern many facets of device operation, including allowable current density before thermal breakdown, device operating frequency, the forward resistance of bipolar devices, and the switching characteristics of two terminal thyristors. The minority carrier transport properties of the III-nitrides had never been measured, so we performed electron beam induced current (EBIC) measurements to determine them. EBIC of both n-type and p-type GaN were investigated, revealing electron diffusion lengths of $0.2 - 2\,\mu$m depending on sample quality, and hole diffusion length of $0.28 \pm 0.02\,\mu$m. Minority carrier lifetimes estimated from these diffusion lengths using the Einstein relation are approximately 7 ns and 0.1 ns for holes and electrons, respectively. A simple model was presented to possibly explain the limitation of diffusion lengths in GaN by recombination at dislocations. It was suggested that edge dislocations likely enhance recombination because they can behave as electron traps. The free holes are attracted by the space charge region surrounding the dislocations, which extends on the order of the Debye length.

Bibliography

[1] N. R. Perkins, M. N. Horton, Z. Z. Bandić, T. C. McGill, and T. F. Kuech, *Mat. Res. Soc. Symp. Proc.* **395**, 243 (1996).

[2] Z.Z. Bandić, E. C. Piquette, P. M. Bridger, R. A. Beach, T. F. Kuech, and T. C. McGill, *Solid–State Electron.* **42**, 2289 (1998).

[3] T. P. Chow and R. Tyagi, *IEEE Trans. Electron Devices* **41**, 1481 (1994).

[4] Z. Z. Bandić, P. M. Bridger, E. C. Piquette, and T. C. McGill, *Appl. Phys. Lett.* **74**(9), 1266 (1999).

[5] A. Witek, *Diam. Relat. Mater.* **7**, 962 (1998).

[6] X. Zhang, P. Kung, D. Walker, J. Piotrowski, A. Rogalski, A. Saxler, and M. Razeghi, *Appl. Phys. Lett.* **67**, 2028 (1995).

[7] S. Sze, Semiconductor Devices (John Wiley & Sons, New York, 1981).

[8] B. J. Baliga, Power Semiconductor Devices (PWS, Boston, 1996).

[9] J. Kolnik, I. H. Ogusman, K. F. Brennan, R. Wang, and P. P. Ruden, *J. Appl. Phys.* **82**, 726 (1997).

[10] Z. Z. Bandić, P. M. Bridger, E. C. Piquette, T. F. Kuech, and T. C. McGill, *Mat. Res. Soc. Symp. Proc.* **483**, 399 (1998).

[11] L. Wang, M. I. Nathan, T. H. Lim, M. A. Khan, and Q. Chen, *Appl. Phys. Lett.* **68**, 1267 (1996).

[12] S. N. Mohammad, Z. Fan, A. E. Botchkarev, W. Kim, O. Aktas, A. Salvador, and H. Morkoç, *Electron. Lett.* **32**, 598 (1996).

[13] E. V. Kalinina, N. I. Kuznetsov, V. A. Dmitriev, K. G. Irvine, and C. H. Carter, Jr., *J. Elec. Mater.* **25**, 831 (1998).

[14] P. Hacke, T. Detchprohm, K. Hiramatsu, and N. Sawaki, *Appl. Phys. Lett.* **63**, 2676 (1993).

[15] E. C. Piquette, Z. Z. Bandić, and T. C. McGill, *Mat. Res. Soc. Symp. Proc.* **482**, 1089 (1998).

[16] Q. Z. Liu and S. S. Lau, *Solid–State Electron.* **42**, 677 (1998) and references cited therein.

[17] R. P. Vaudo, V. M. Phanse, M. C. Cattrel and J. M. Redwing, 2nd International Conference on Nitride Semiconductors, Tokushima, Japan (1997).

[18] D. C. Look, *Electrical Characterization of GaAs Materials and Devices* (Wiley, New York, 1989).

[19] D. C. Look and R. J. Molnar, *Appl. Phys. Lett.* **70**, 3377 (1997).

[20] W. Götz, J. Walker, L. T. Romano, N. M. Johnson, and R. J. Molnar, *Mat. Res. Soc. Symp. Proc.* **449**, 525 (1997).

[21] N. Dyakonova, A. Dickens, M. Shur, R. Gaska, and J. W. Yang, *Appl. Phys. Lett.* **72**, 2562 (1998).

[22] H. M. Ng, D. Doppalapudi, T. D. Moustakas, N. G. Weimann, and L. F. Eastman, *Appl. Phys. Lett.* **73**, 821 (1998).

[23] N. G. Weimann, L. F. Eastman, D. Doppalapudi, H. M. Ng, T. D. Moustakas, *J. Appl. Phys.* **83**, 3656 (1998).

[24] Z. Z. Bandić, P. M. Bridger, E. C. Piquette, and T. C. McGill, *Appl. Phys. Lett.* **72**, 3166 (1998).

[25] Z. Z. Bandić, P. M. Bridger, E. C. Piquette, and T. C. McGill, *Appl. Phys. Lett.* **73**, 3276 (1998).

[26] H. K. Kuiken and C. Vanopdorp, *J. Appl. Phys.* **57**, 2077 (1985).

[27] P. M. Bridger, Z. Z. Bandic, E. C. Piquette, and T. C. McGill, *Appl. Phys. Lett.* **73**, 3438 (1998).

[28] T. Sugahara, H. Sato, M. S. Hao, Y. Naoi, S. Kurai, S. Tottori, K. Yamashita, K. Nishino, L. T. Romano, S. Sakai, *Jpn. J. Appl. Phys. Pt. 2* **37**, L398 (1998).

[29] L. Chernyak, A. Osinsky, H. Temkin, J. W. Yang, Q. Chen, and M. Asif Khan, *Appl. Phys. Lett.* **69**, 2531 (1996).

[30] X. Zhang, D. H. Rich, J. T. Kobayashi, N. P. Kobayashi, and P. D. Dapkus, *Appl. Phys. Lett.* **73**, 1430 (1998).

[31] R. J. Radtke, U. Waghmare, H. Ehrenreich, and C. H. Grein, *Appl. Phys. Lett.* **73**, 2087 (1998).

[32] C. Sasaoka, H. Sunakawa, A. Kimura, M. Nido, A. Usui, A. Sakai, *J. Cryst. Growth* **190**, 61 (1998).

[33] F. Binet, J. Y. Duboz, E. Rosencher, F. Scholz, and V. Härle, *Appl. Phys. Lett.* **69**, 1202 (1996).

[34] S. J. Rosner, E. C. Carr, M. J. Ludowise, G. Girolami, and H. I. Erikson, *Appl. Phys. Lett.* **70**, 420 (1997).

[35] J. W. Yang, C. J. Sun, Q. Chen, M. Z. Anwar, M. Asif Khan, S. A. Nikishin, G. A. Seryogin, A. V. Osinsky, L. Chernyak, H. Temkin, Chimin Hu, and S. Mahajan, *Appl. Phys. Lett.* **69**, 3566 (1996).

[36] F. A. Ponce, MRS Bull. **22**, 51 (1997).

[37] W. R. Harding, I. D. Blenkinsop, and D. R. Wright, *Electron. Lett.* **12**, 502 (1976).

[38] G. L. Pearson, W. T. Read, and F. J. Morin, *Phys. Rev.* **93**, 666 (1954).

[39] M. S. Shur, A. Khan, B. Gelmont, R. J. Trew, M. W. Shin, *Inst. Phys. Conf. Ser.* **141**, 419 (1995).

Chapter 6 Metallic Contacts to Gallium Nitride

6.1 Introduction

Gallium nitride is becoming an established semiconductor material for wide band gap optoelectronic devices, and continues to show promise as a candidate for high power, high temperature, and high frequency applications. The characteristics of ohmic and Schottky metallic contacts play an important role in the performance of these devices. Progress continues to be made in reduction of specific contact resistance (R_c) of ohmic contacts to both p- and n-type GaN, although further understanding and better reproducibility remain desirable. Additionally, high temperature and high power devices require Schottky contacts with well defined and stable barriers, low forward resistance, and high reverse breakdown fields.

Contact resistances below $10^{-4}\,\Omega \cdot \mathrm{cm}^2$ are needed for laser diodes (LDs) and efficient semiconductor power devices. Very low specific contact resistivities have been reported using TiAl metallization, usually annealed, and often requiring special GaN surface treatment such as pre-annealing [1], RIE processing [2], or ion implantation [3]. Laser diodes have also been successfully fabricated using these contacts as n- electrodes [4]. There has been considerable speculation about the exact role played by Ti in the formation of these contacts. It is believed that a thin ($\sim 200\,\text{Å}$) layer of Ti aids in reduction of the native oxide of GaN to facilitate Al contact to the fresh surface [5]. Also proposed is the formation of a TiN layer at the interface which results in N vacancies near the surface of GaN and thus locally high donor concentration [6]. More recent work has focused on the formation of $TiAl_3$ alloys in annealed contacts [7]. High power and high temperature devices require contacts that are thermally and chemically stable, and refractory metals such as tungsten have been studied as initial

candidates for these applications. It is our hope here to elucidate on these issues from the viewpoint of sputtering surface treatments, as well as to explore the parameter space of metal type and interface preparation rather than attempt the achievement of ultra low values of R_c.

We have conducted a sweeping study of various metal contacts to GaN, including Al, TiAl, Cr, Mo, W, Au, Sb, Ce, and Mg, which were applied with varying surface sputtering treatment techniques. Many of these metals were found to result in linear or almost linear pad-to-pad current-voltage characteristics, and for these, specific contact resistance was measured by the circular transmission line method (CTLM) [8, 9]. For those metals that produced highly rectifying contacts, the Schottky barrier heights and ideality factors were measured.

6.2 Sputtered Ohmic contacts to *n*-GaN

6.2.1 Experiment

The gallium nitride layers used for this study were grown by molecular beam epitaxy (MBE) on c-plane sapphire substrates employing a low temperature (650°C) AlN buffer layer according to the methods of chapter 3. The backs of the substrates were coated with Mo to facilitate radiative heating, and substrate temperature was held at 800°C during growth under slightly metal-rich conditions. The growth rate was $0.35\,\mu$m/h and the final film thickness was nominally $1\,\mu$m. Two types of samples were studied that differed in electron concentration. High resistivity samples were unintentionally doped to approximately 10^{15}cm^{-3} as measured by Van der Pauw Hall technique, and lower resistivity samples were doped by co-evaporation of Si during growth to $n = 9.2 \cdot 10^{17}$ cm^{-3}. Although more highly doped material is expected to produce less resistive contacts, the more insulating samples focused on here were used to render a large degree of differentiation in contact properties caused by various sample preparations.

Contact samples were prepared by cleaning the GaN films in organic solvents

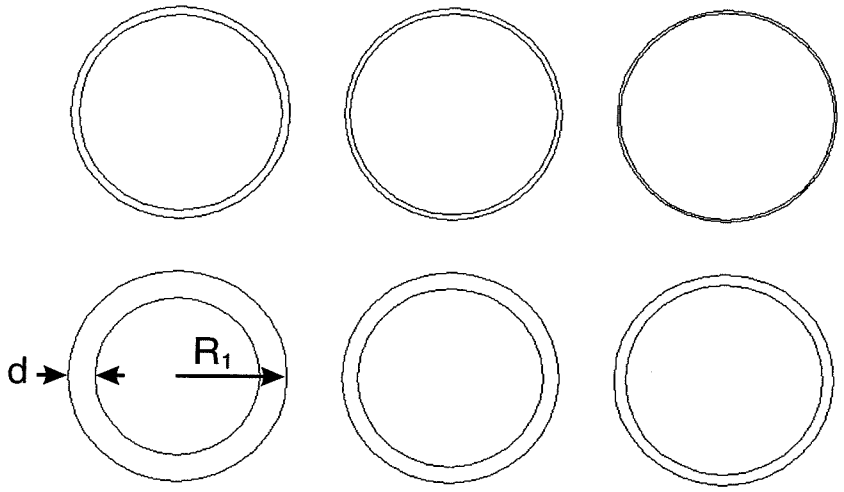

Figure 6.1: Schematic diagram of the circular contact layout used for contact resistance measurements. The outer radius R_1 is fixed at 200 μm. The inner contact radius varies so that the gap spacing d is 50, 30, 20, 15, 10, and 5 μm.

followed by HF:H_2O_2 solution which removed the backside metallization from the sapphire substrates. Metals under study were deposited and patterned by liftoff photolithography to form CTLM patterns as shown in Fig 6.1. The use of CTLM structures is advantageous because no etching of GaN is required for feature isolation. The circular gap between metal pads had a constant outer radius R_1 of 200 μm with a varying gap spacing d of 50, 30, 20, 15, 10, and 5 μm. The spacing of these pads and the precise knowledge of d are essential in avoiding systematically low R_c values caused by overdevelopment in the photolithographic processing. We used SEM and optical microscopy to measure and verify the gap spacings for all samples in this study. In addition to measurements taken with this geometry, several samples were also redundantly measured using a CTLM pattern similar to that above, but of half scale, with outer circle radius 100 μm and gaps of 25, 15, 10, 7.5, 5, and 2.5 μm, as a means of verification. Specific contact resistance values for the two patterns matched to within statistical error (less than 1%).

All metals were deposited in a vacuum chamber of base pressure $\sim 10^{-8}$ torr which is equipped with three DC coupled magnetron targets and one RF coupled

magnetron target to facilitate plasma sputtering deposition. Additionally, bias may be applied to the electrically isolated substrate holder to ignite an RF plasma in the vicinity of the sample. This local plasma can be used as a means of sample surface treatment (pre-sputtering). Prior to contact deposition, the surface of the GaN was pre-sputtered at either 30 Watts, 50 Watts, or 100 Watts RF for 30 seconds in either Ar or N_2 gas with a flow rate of 160 sccm and a system pressure of nominally $2 \cdot 10^{-3}$ torr. Metal thickness was observed during deposition by quartz crystal monitor. For the high resistivity GaN samples (sample H, $n \sim 10^{15}\text{cm}^{-3}$), approximately 1500 Å of Al, Ti/Al (200 Å / 1300 Å), Cr, W, and Mo were deposited on different pieces. For the lower resistivity samples (sample L, $n = 9.2 \cdot 10^{17}\text{cm}^{-3}$), Al, Ti/Al, Cr, W, Mo, Sb, Mg, Ce, and Au were deposited. The pre-sputtering conditions for each sample are summarized in Table 6.1.

After lithographic processing, current was measured as a function of voltage over the range (-5 V, 5 V) using a Hewlett Packard 4156A Precision Semiconductor Parameter Analyzer. Up to six measurements were taken for each value of the gap spacing for each sample. The samples were then annealed at $\sim 700°\text{C}$ for 30 seconds in flowing Ar using a rapid thermal process (RTA) and the current-voltage curves were taken again.

6.2.2 Ohmic contact results and discussion

The current-voltage (I-V) curves varied in linearity. Examples of representative I-V traces are shown in Figure 6.2. To quantify the degree of linearity and rectification, we defined the arbitrary figure of merit

$$\text{LM} = \frac{\text{dI/dV}|_{\text{V=0}}}{\text{dI/dV}|_{\text{V=5}}} = \frac{\text{Differential resistance at 5 Volts}}{\text{Differential resistance at 0 Volts}} \tag{6.1}$$

LM usually ranges from zero to one and increases for samples of more linear I-V curves.

To find specific contact resistance (R_c) the total resistance (derived from the slope

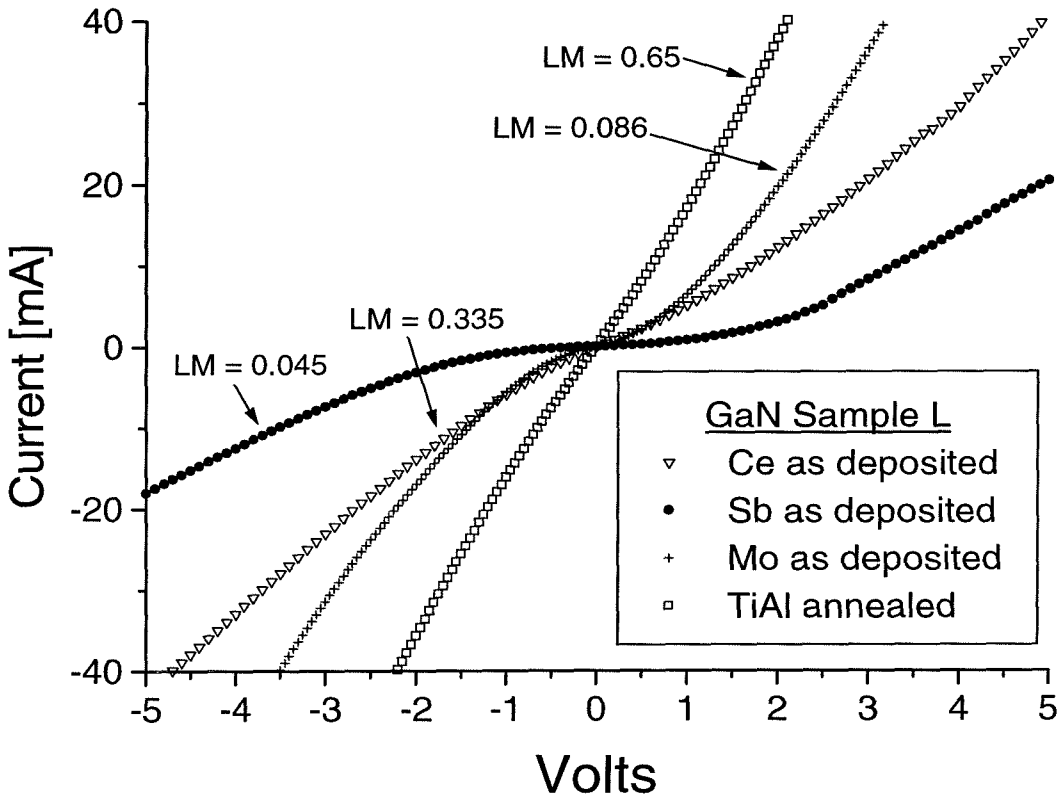

Figure 6.2: Current-voltage characteristics for various metals on GaN sample L, $d = 5\,\mu$m. The linearity factor (LM, Equation 6.1) is the ratio of the slope of these curves at zero bias divided by the slope at 5 Volts. LM is used as a measure of the linearity of metal contacts.

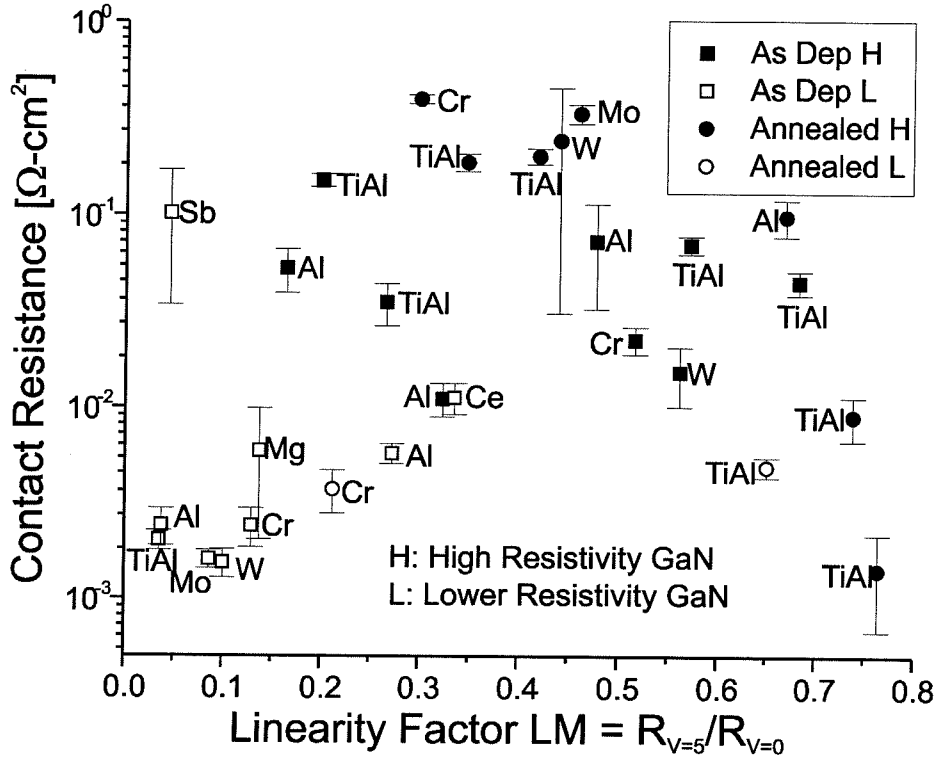

Figure 6.3: Contact resistance is plotted versus the linearity figure LM for various metals and surface treatments.

of the I-V at 5 V) was plotted versus the gap width d and fit with the equation [8]

$$R = \frac{R_s}{2\pi}\left[\ln\left(\frac{R_1}{R_1 - d}\right) + L_T\left(\frac{1}{R_1 - d} + \frac{1}{R_1}\right)\right] \tag{6.2}$$

to find the transfer length L_T and sample sheet resistance R_s. R_c can then be calculated using the formula $R_c = L_T^2 R_s$ [$\Omega \cdot \mathrm{cm}^2$].

A summary of results encompassing all investigated metals and pre-sputtering treatments is presented in Table 6.1, and represents a distillation of **over 750 I-V measurements.** A graphic representation of the data is shown in Figure 6.3. In general, contacts to sample H are more resistive than those to sample L. The data for sample H also show a general trend that the lowest R_c contacts are also the most linear. The clustering of annealed TiAl data points in the lower right section of Figure 6.3 indicates that these are the premium contacts of this study. Shown in Figure 6.4A are resistance data for TiAl contacts to GaN sample H after a variety

As Deposited Contacts					Annealed	
Sample	Metal	Sputter Treatment	R_c	LM	R_c	LM
H	Al	None	$7.3 \cdot 10^{-2}$	0.48	$9.8 \cdot 10^{-2}$	0.67
H	Al	Ar, 50W, 30 sec.	$1.1 \cdot 10^{-2}$	0.32		
H	Al	Ar, 100W, 30 sec.	$5.3 \cdot 10^{-2}$	0.16		
H	TiAl	None	$4.5 \cdot 10^{-2}$	0.68	$9.0 \cdot 10^{-3}$	0.74
H	TiAl	Ar, 50W, 30 sec.	$3.5 \cdot 10^{-2}$	0.27	$1.9 \cdot 10^{-1}$	0.35
H	TiAl	Ar, 100W, 30 sec.	$1.5 \cdot 10^{-1}$	0.20	$2.0 \cdot 10^{-1}$	0.42
H	TiAl	N_2, 50W, 30 sec.	$7.0 \cdot 10^{-2}$	0.57	$1.4 \cdot 10^{-3}$	0.76
H	Cr	Ar, 30W, 30 sec.	$2.2 \cdot 10^{-2}$	0.52	$4.0 \cdot 10^{-1}$	0.30
H	W	Ar, 30W, 30 sec.	$1.5 \cdot 10^{-2}$	0.56	$2.4 \cdot 10^{-1}$	0.44
H	Mo	Ar, 30W, 30 sec.	$2.2 \cdot 10^{-2}$	0.69	$3.3 \cdot 10^{-1}$	0.46
L	Al	None	$5.7 \cdot 10^{-3}$	0.27		
L	Al	Ar, 50W, 30 sec.	$2.4 \cdot 10^{-3}$	0.04		
L	TiAl	None	rectifying		$4.9 \cdot 10^{-3}$	0.65
L	TiAl	Ar, 50W, 30 sec.	$2.0 \cdot 10^{-3}$	0.04		
L	Cr	Ar, 30W, 30 sec.	$2.4 \cdot 10^{-3}$	0.13	$3.7 \cdot 10^{-3}$	0.21
L	W	Ar, 30W, 30 sec.	$1.5 \cdot 10^{-3}$	0.10	rectifying	
L	Mo	Ar, 30W, 30 sec.	$1.6 \cdot 10^{-3}$	0.09	rectifying	
L	Sb	Ar, 30W, 30 sec.	$1.0 \cdot 10^{-1}$	0.05		
L	Mg	Ar, 30W, 30 sec.	$5.9 \cdot 10^{-3}$	0.14		
L	Ce	Ar, 30W, 30 sec.	$1.1 \cdot 10^{-2}$	0.34		

Table 6.1: Summary of sputtered contact study.

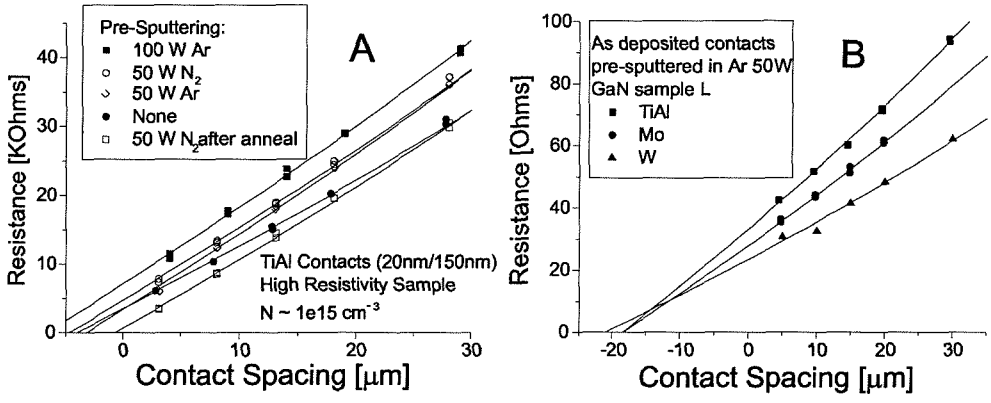

Figure 6.4: Resistance as a function of gap spacing for A) TiAl contacts to high resistivity n-GaN, and B) TiAl, Mo, and W contacts on lower resistivity GaN. For TiAl, the lowest contact resistance is for the annealed sample, while the sample that was pre-sputtered at 100 Watts RF shows highest R_c, presumably due to plasma damage. Solid lines are a fit to the data using equation 6.2.

of surface pre-sputtering treatments. The lowest value for R_c as well as the highest value of LM is obtained by pre-sputtering the surface in N_2 under 50 Watts plasma power, followed by a post-deposition anneal. The most resistive contacts were those pre-sputtered at 100 Watts, which was true for all metals. These results suggest that lattice damage occurs at this power level that hinders linear ohmic formation. It is also interesting to note that the samples that were pre-sputtered in Ar gas tended to have fairly low R_c as deposited, but degraded upon annealing.

Pre-sputtering is often referred to as sputter-cleaning, and one may hope that any native GaN oxide and surface contaminants would be removed by this processing. Remarkably, many of the best ohmic contact results in the literature are attributed to defects induced by annealing [10] or RIE treatments. Since high power pre-sputtering resulted in an increase in R_c, it appears that any damage caused by such treatment is of a different nature. XPS studies have been reported [11] that indicate pre-sputtering in Ar changes the surface stoichiometry of GaN films, making them Ga rich, while sputtering in N_2 does not change the stoichiometry. This production of N vacancies by Ar sputtering seems to aid in ohmic contact formation for as-deposited samples, as is shown by the relatively low R_c for unannealed TiAl and the Group VIB metals Mo, W, and Cr in Table 6.1. However, R_c for TiAl deposited on an Ar sputtered surface

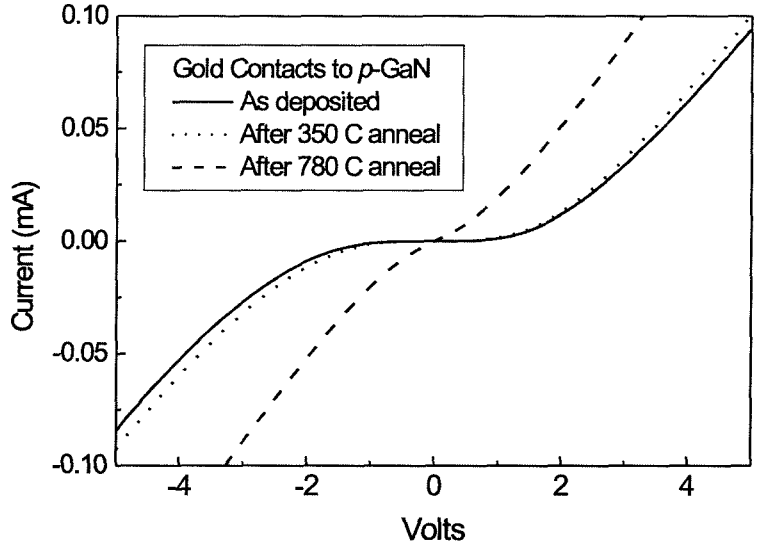

Figure 6.5: Effect of annealing on Au contacts to p-GaN.

was not observed to decrease upon annealing, as it does with N_2-treated and non-sputtered samples. This suggests that Ar sputter treatments may hinder somewhat the sintering action of the TiAl contacts.

6.3 Gold contacts to p-GaN

A limited study of ohmic contacts to p-type GaN was conducted, wherein square gold pads were patterned on MOCVD-grown Mg-doped GaN layers. The pad-to-pad current-voltage characteristic was then recorded for as-deposited and annealed samples. The annealing was done using a resistive strip heater in flowing argon. The results are shown in Figure 6.5 for annealing temperatures up to 780°C. The contacts remained largely rectifying for all anneal temperatures, although the contacts showed some improvement after the annealing treatment at 780°C.

6.4 Schottky contacts to n-GaN

For those samples where contacts were highly rectifying, the Schottky barrier height (ϕ_b) and ideality factor n were measured by analyzing the forward bias region of

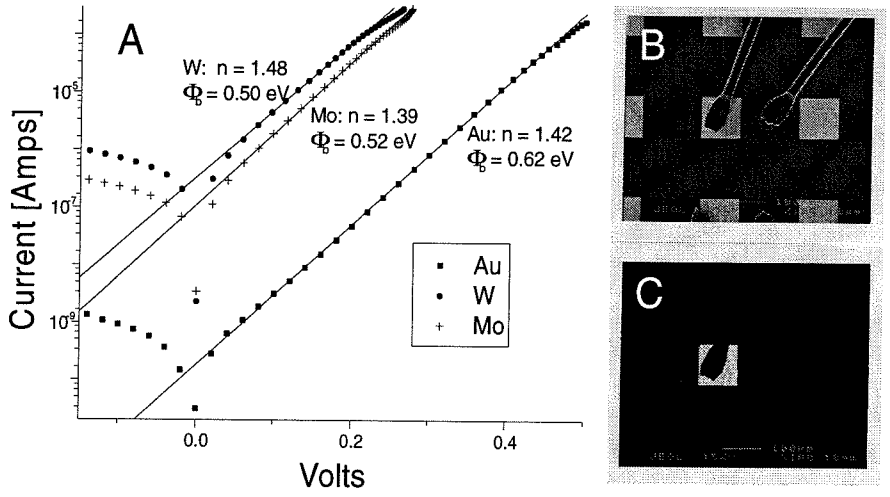

Figure 6.6: A) Current-voltage curves for Schottky diodes formed from as deposited Au, and annealed Mo and W. B) SEM scan of Au diodes with C) the same picture in EBIC mode. The EBIC scan is used to determine the effective area of the contacts.

the I-V curves. Figure 6.6 shows a plot of $\log(I)$ vs V for as-deposited Au, and annealed Mo and W. The plot is linear over the region from $\sim 3kT/q$ to over 0.2 Volts, which was fit to yield the values for I_0 and n for each diode according to the equation $\ln(I) = \ln(I_0) + qV/nkT$ where $I_0 = SA^*T^2 \exp^{-q\phi_b/kT}$. The device area S is taken here to be the geometrical area of the contacts, and the theoretical value of $A^* = 24$ A/cm^{2}K^2 was used for effective Richardson constant, which is considerably larger than most expermentally determined values. Thus, the barrier heights reported here should be taken as maximum values for this material. The variation observed in barrier height also gives evidence that the Fermi level is unpinned at the GaN surface.

The high voltage gold Schottky diodes of chapter 5 were also analyzed to determine barrier height and ideality factor. Results for the lateral geometry circular pad diodes are shown in Figure 6.7. By plotting the barrier height as a function of ideality factor, one can use a fit to this data to extrapolate for an ideality factor of $n = 1.01$, which corresponds to a nominal, "ideal" barrier height. (The ideality factor of 1.01 is used rather than 1.00 to account for image force lowering effects.) From this data, the nominal gold barrier height on n-GaN, as measured by I-V analysis, was found to be approximately 1.1 eV.

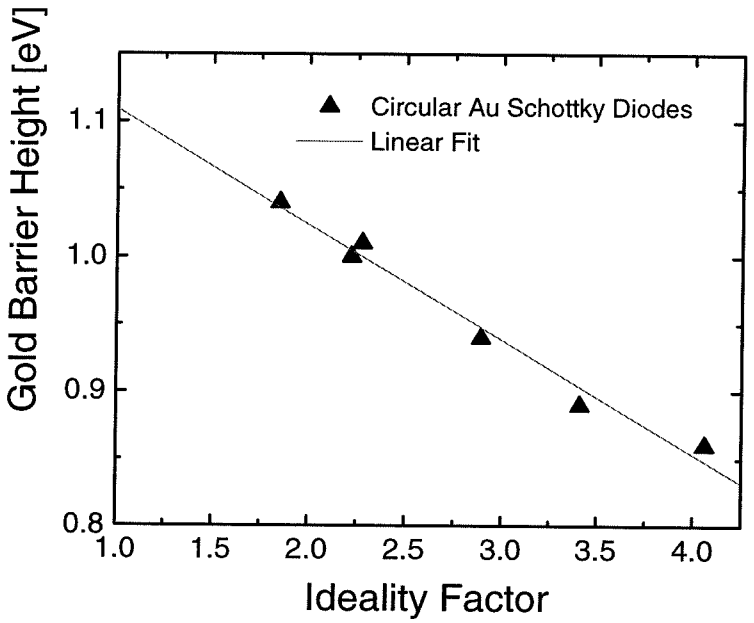

Figure 6.7: The gold Schottky barrier height is plotted as a function of ideality factor for the circular GaN diodes described in section 5.4. Extrapolation of the gold barrier height to an ideality factor of 1.01 yields a value of approximately 1.1 eV.

6.5 Summary and conclusion

Sputter deposited metal contacts to n-GaN were characterized by current-voltage analysis and contact resistances were measured by the circular geometry transmission line method. Contact resistance was observed to be dependent on surface pre-sputtering treatments, specifically the plasma power and gas used, GaN doping, and post-deposition annealing as summarized in Table 6.1. The lowest values for R_c as well as the highest values of linearity are obtained for TiAl by pre-sputtering in N_2 under 50 Watts plasma power followed by a post-deposition anneal. Gold as an ohmic contact to p-GaN was studied as a function of annealing temperature and showed I-V curves which became less rectifying as anneal temperature was increased.

Schottky barriers to n-GaN were analyzed using the forward bias region of current-voltage curves. The gold Schottky barrier height was found to range from 0.62 to 1.07 depending on the origin and quality of the GaN sample. A nominal value for the gold Schottky barrier height of 1.1 eV was estimated for an ideality factor of 1.01.

Bibliography

[1] L. F. Lester, J. M. Brown, J. C. Ramer, L. Zhang, S. D. Hersee and J. C. Zolper, *Appl. Phys. Lett.* **69**, 2737 (1996).

[2] Z. Fan, S. N. Mohammad. W. Kim, Ö. Aktas, A. E. Botchkarev, K. Suzue, H. Morkoç, K. Duxstad and E. E. Haller, *J. Elec. Mater.* **25**, 1703 (1996).

[3] J. Burm, K. Chu, W. A. Davis, W. J. Schaff, L. F. Eastman and T. J. Eustis, *Appl. Phys. Lett.* **70**, 464 (1997).

[4] S. Nakamura, M. Senoh, S. Nagahama, M. Iwara, T. Yamada, T. Marsushita, H. Kiyoku and Y. Sugimoto, *Jpn. J. Appl. Phys.* **35**, L74 (1996).

[5] B. P. Luther, S. E. Mohney, T. N. Jackson, M. Asif Khan, Q. Chen and J. W. Yang, *Appl. Phys. Lett.* **70**, 57 (1997).

[6] M. E. Lin, Z. Ma, F. Y. Huang, Z. F. Fan, L. H. Allen and H. Morkoç, *Appl. Phys. Lett.* **64**, 1003 (1994).

[7] S. Ruvimov, Z. Liliental-Weber, J. Washburn, D. Qiao, S. S. Lau, and Paul K. Chu, *Appl. Phys. Lett.* **73**, 2582 (1998).

[8] G. S. Marlow and M. B. Das, *Solid–State Electron.* **25**(2), 91 (1982).

[9] G. K. Reeves, *Solid–State Electron.* **23**, 487 (1980).

[10] J. S. Chan, N. W. Cheung, L. Schloss, E. Jones, W. S. Wong, N. Newman, X. Liu, E. R. Weber, A. Gassman and M. D. Rubin, *Appl. Phys. Lett.* **68** 2702 (1996).

[11] H. Ishikawa, S. Kobayashi, Y. Koide, S. Yamasaki, S. Nagai, J. Umezaki, M. Koike and M. Murakami, *J. Appl. Phys.* **81** (3), 1315 (1997).

Part II

Zinc Sulfide/Gallium Nitride Light Emitting Heterostructures

Chapter 7 Zinc Sulfide/Gallium Nitride Light Emitting *p-n* Diodes

7.1 Introduction

Zinc sulfide, with its wide direct bandgap of approximately 3.7 eV at room temperature, has long been known as a versatile and efficient visible light emitting compound. It has been extensively used as a phosphor, and continues to show promise in semiconductor light emitting devices, such as ZnS based flat panel displays [1, 2, 3], light emitting diodes [4, 5], and semiconductor lasers [6]. However, difficulties in producing high quality doped material, particularly *p*-type, have otherwise reduced the utility of the sulfide materials system.

Without *p*-type ZnS, the obvious light emitting structure, a *p-n* diode, cannot be made. Instead, investigators have used other means to produce minority carrier population and radiative recombination in ZnS. In the traditional role as a powder phosphor, the excitation is by electron bombardment and cathodoluminescence, for instance in a cathode ray tube (CRT). Other more modern techniques for producing flat panel displays [1, 2] involve accelerating conduction band electrons in a high electric field to produce holes by impact ionization or induce luminescence through excitation of atomic transitions. In this case, referred to as an AC thin film electroluminescent device (ACTFEL), the device structure is as shown in Figure 7.2. Electrons, from traps at the ZnS/insulator interfaces, are accelerated by a large alternating voltage, "sloshing" back and forth with every cycle and generating holes which recombine with electrons at luminescent centers. Typical luminescence "activators" are substitutional copper and silver atoms at Zn sites, in which case they act as deep acceptors, or atoms such as manganese which utilize an atomic excited state transition. The energy levels of the Cu and Ag within the band gap result in

green or blue luminescence, while Mn gives a broad amber response. For the ACT-FEL devices, typical voltage applied is 100 – 150 volts, at frequencies of 60 Hz to 5 kHz. Although this technique has been somewhat successful in production of small flat panel displays, the high voltage AC drivers that are required increase production costs and system complexity. Obviously, if *p-n* ZnS LEDs were available, they would have many advantages over the AC devices, since they would operate without the requirement of AC drivers and at much lower voltages (typically the band gap, 3.7 eV).

Since *p*-type doping of ZnS has proven extremely difficult [7], one might next turn to a heterostructure device in which holes could be injected from a dissimilar material into the *n*-type ZnS which would be the active light emitting region. One of the criteria for any such material is that it can be doped *p*-type and that its valence band lies lower in energy than the ZnS valence band, so there would be no barrier for hole injection. Figure 7.1 is a McCaldin diagram showing the energy gap, band alignment, and dopability of a number of possible candidate materials [8]. Although it is heavily lattice mismatched ($\sim$ 20%), the only material that fulfills our criterion is GaN, which has recently been produced *p*-type [9, 10, 11]. The possibility of using GaN as a hole injector into ZnS and other light emitting semiconductor materials was originally proposed by McCaldin, *et al.* [12] This chapter describes the operational principles and presents the major technical issues governing the operation of a *n*-ZnS/*p*-GaN hight emitting heterostructure device. In addition, chapter 8 describes work done on the growth of ZnS on GaN (0001) and sapphire (0001) substrates by molecular beam epitaxy (MBE) in an attempt to fabricate prototype ZnS:(Al,Ag)/GaN:Mg blue LEDs and to characterize this potentially interesting system as well as to gain insight into highly lattice mismatched systems in general.

7.2 General motivation

GaN/Zn(Cd)S heterostructures are attractive for both discrete diodes in the blue and green region of visible spectrum and for integrated electroluminescent displays. Dis-

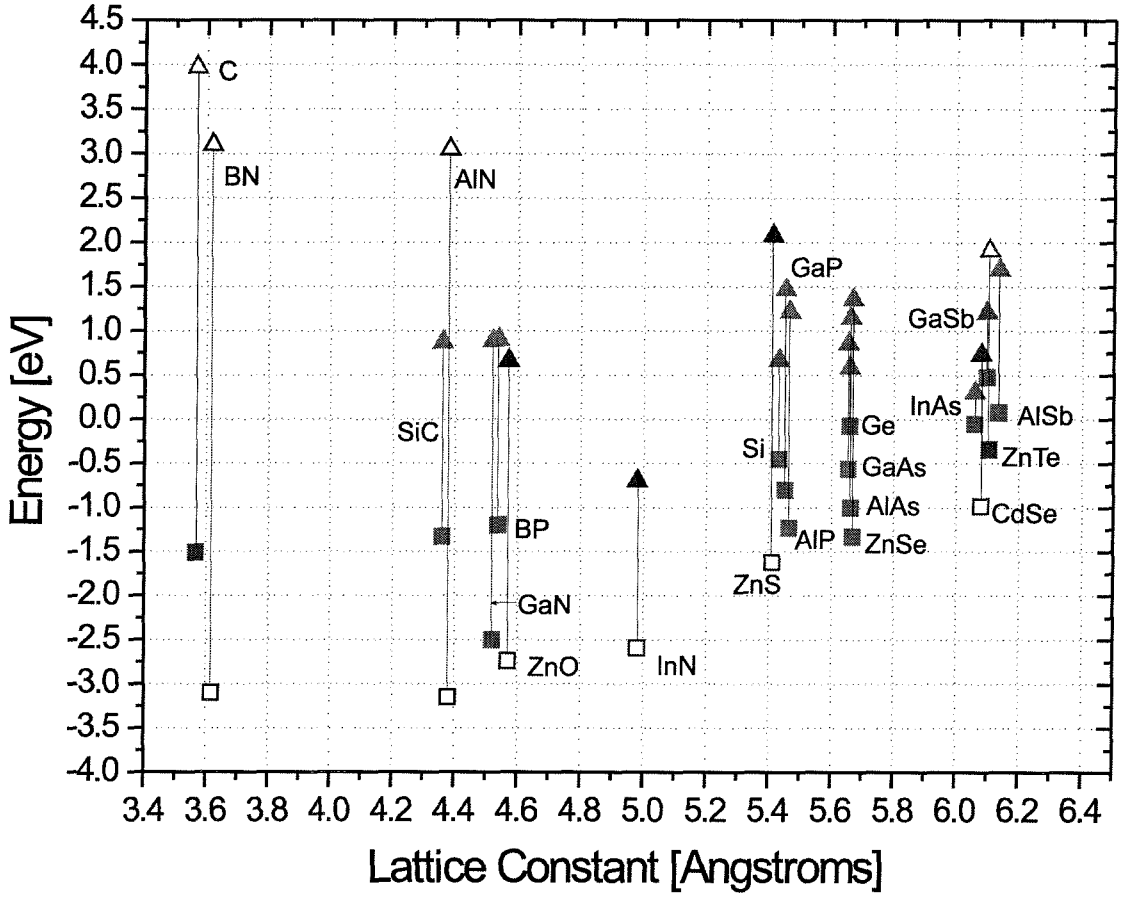

Figure 7.1: McCaldin diagram showing lattice constants, energy gaps, band lineups, and dopability for a variety of semiconductors. A solid square indicates p-dopability while a solid triangle indicates n-dopability. Gallium nitride is the only p-dopable material with a valence band below that of ZnS.

crete diodes have significant potential as traffic lights and other applications where InGaN-based light emitters are now making inroads. Integrated DC electroluminescent displays seem extremely attractive not only for laptop computer monitors, but also for small head mounted displays which may be used for military and personal mobile computing applications. Rapid developments in the Internet and communications industry, as well as trends in electronics and storage miniaturization (such as 1 inch 340 MB hard disks [13]) should bring a variety of mobile, palm-top size electronics devices, and each one of them will need to have a moderate size color display.

The crucial advantage of direct current electroluminescent (DCEL) displays, compared to other technologies such as passive and active matrix liquid crystal displays [14], and ACTFEL displays [14, 15], is reduction in power consumption. Liquid crystal displays generate color pixels employing red, green or blue filters and a pair of polarizers which determine intensity transmission from the back light (see Figure 7.3) [14]. In this way a considerable amount of energy is wasted, because the back light has to be on continuously during display operation, and only a small fraction of generated light energy is transmitted. ACTFEL displays require voltages of approximately $100 - 150$ V to generate light by impact excitation of a light emitting center by high energy electrons, typically in ZnS powder (see Figure 7.2) [15]. Although ACTFEL displays utilize the ZnS materials system, the high voltages required and the overall power consumption are far from completely satisfactory, expecially for portable and mobile computing applications. In the case of DCEL displays based on ZnS, voltages required to turn-on individual diodes are approximately $3 - 5$ V, while at the same time current densities are smaller or comparable to ACTFEL devices. This reduction in voltage and current could potentially result in a decrease in power consumption by a factor of 10 to 100.

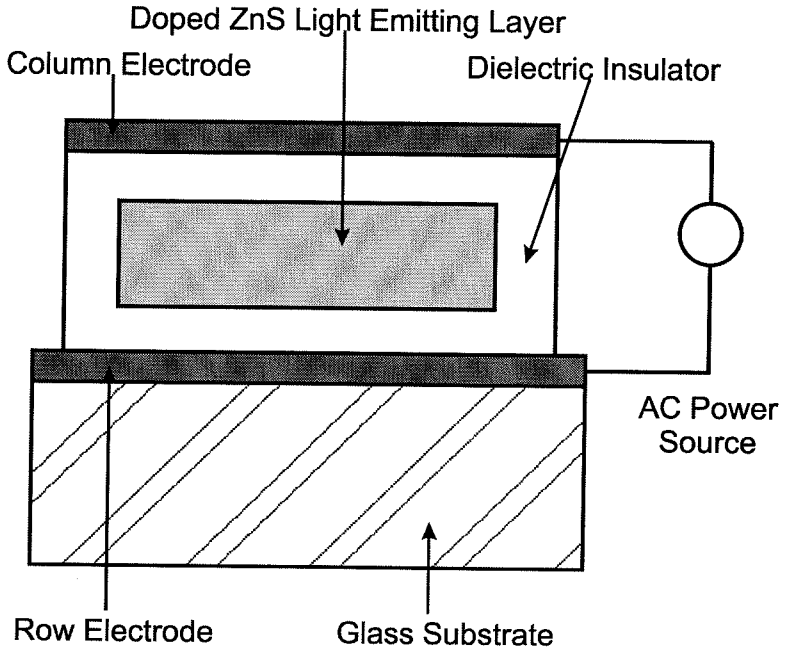

Figure 7.2: Cross section of an ACTFEL device. A large AC voltage driving signal causes high alternating electric fields within the phosphor layer, resulting in impact excitation of light emitting centers. For example, Cu and Ag act as green and blue luminescence centers, respectively, in ZnS (see Table 7.1).

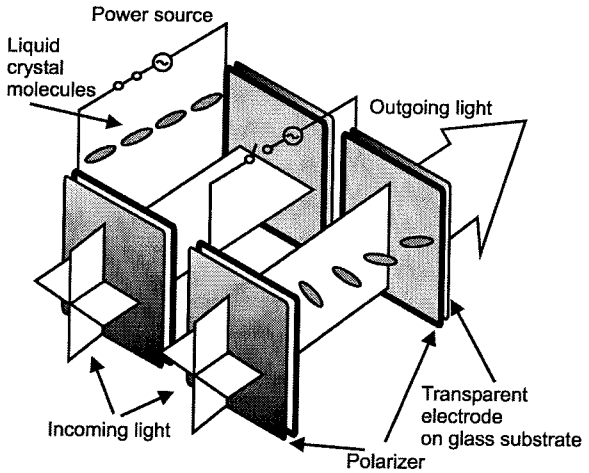

Figure 7.3: Schematic of a liquid crystal display [14]. The orientation of liquid crystal molecules is very sensitive to the externally applied electric field. Each single pixel is formed by an optically tunable shutter that is controlled by a locally applied electric field and is sandwiched between a pair of polarizers. The light image is produced by addressing top and bottom line electrodes of the cell.

Table 7.1: Possible luminescent centers in ZnS. Wavelengths are for room temperature.

ZnS phosphor (wurtzite)	DAP emission wavelength [nm] high energy "blue"	low energy "green"	Reference
ZnS:Ag,Al	388	435	[16][17]
ZnS:Ag,Al(zb)	380	450	this work
ZnS:Ag,Cl	388	435	[16]
ZnS:Cu,Al	460	527	[16][17]
ZnS:Cu,Cl	443	520	[16]
Self-activated emission	zinc-blende	wurtzite	
ZnS:Cl	456	451	[16]
ZnS:Al	470	463	[16],[17]
ZnS:Al	420	–	this work
Atomic transitions	color	Lum [cd/m^2]	Eff.	
ZnS:Mn (60 Hz)	amber	300	5	[18]
ZnS:Mn (2.5 kHz)	amber	3500		[2]
ZnS:Sm,Cl	red	12	0.08	[18]
ZnS:Tb	green	90	0.6	[18]
ZnS:Tb,F (5 kHz)	green	1700		[2]
Alternative phosphors for blue				
ZnS:Tm,F	blue	0.2	< 0.01	[18]
SrS:Ce	blue	100	0.8	[1] [18]
SrS:Ce,Cl (5 kHz)	blue	1100		[2]
$CaGa_2S_4$:Ce	blue	10	0.04	[1][18]

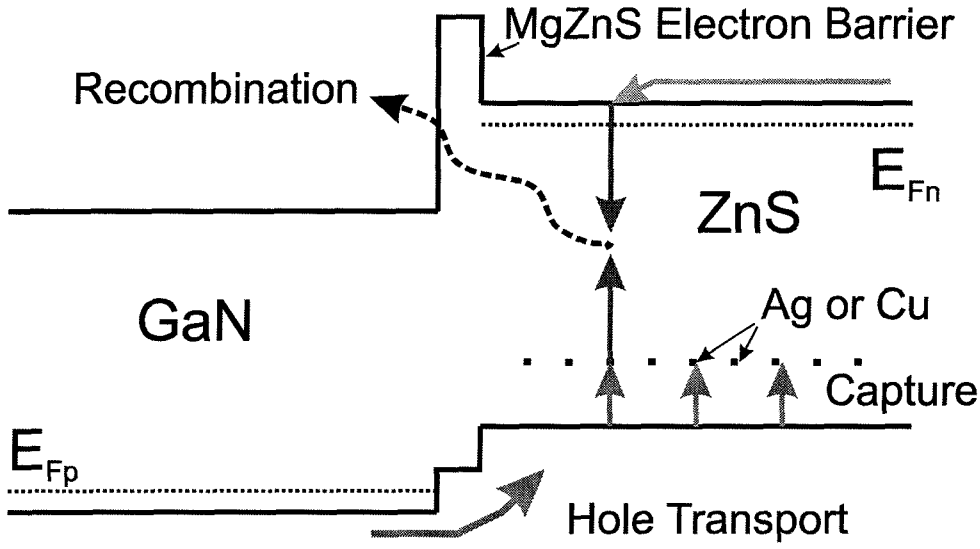

Figure 7.4: Flat band diagram of the p^+-GaN/n-ZnS LED heterostructure. Since the valence band edge of GaN lies below that of ZnS, there is no barrier to injection of holes from the GaN into the ZnS. As this is a Type II staggered band alignment, there is also no barrier for transport of electrons into the GaN layer. As hole transport is what is desired, one solution is the inclusion of a MgZnS electron blocking layer. When holes are transported into the ZnS layer, they become strongly bound to the deep acceptor centers (Ag for blue, Cu for green) and recombine with electrons in the n-type ZnS layer via a donor-acceptor pair transition.

7.3 Principle of operation of p-GaN/n-ZnS light emitting diodes

The flat band energy diagram for a p^+-GaN/n-ZnS heterostructure is shown in Figure 7.4. The GaN valence band edge E_v is expected to lie approximately $0.75 - 1$ eV below the valence band of ZnS. This represents a staggered type II band alignment, and there is no barrier for transport of holes from p-GaN to n-ZnS. Neither is there a barrier for electron transport from the ZnS into the GaN. Under these conditions, the relative magnitudes of electron and hole current across the interface will control where the majority of recombination takes place and thus the characteristics of device operation. Since hole transport across the interface is what is desired, one solution is the inclusion of a MgZnS electron blocking layer between the GaN layer and ZnS layer. Preliminary drift-diffusion modeling calculations for both the basic ZnS/GaN structure as well as the electron blocking layer structure have been carried out by

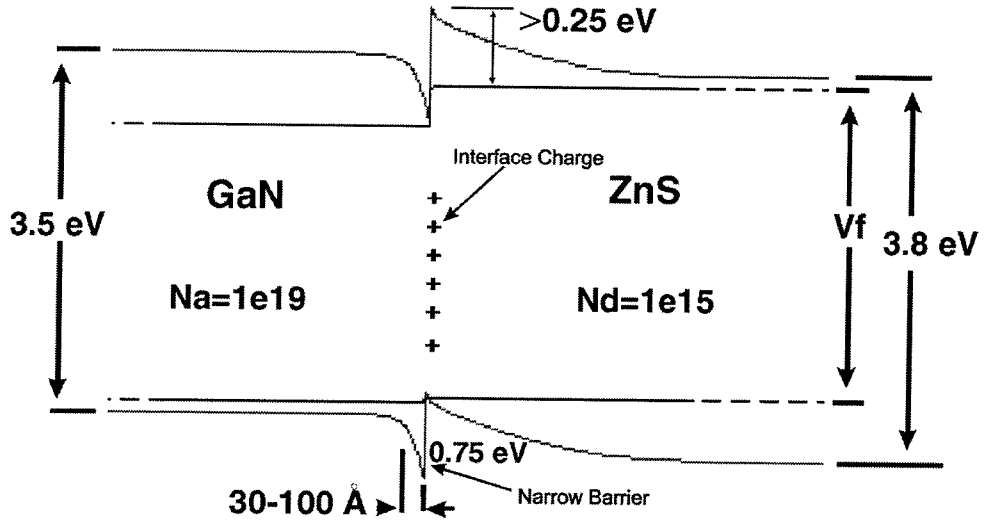

Figure 7.5: Shown is a schematic band diagram of the basic ZnS/GaN LED structure under approximately 3 V forward bias. For hole injection to occur from the GaN layer into the ZnS layer, tunneling should occur through the narrow barrier in the valence band. To make the valence band barrier as narrow as possible, the acceptor concentration in the GaN layer should be as high as possible. Typical Mg concentrations achievable in p-type GaN are of the order of 10^{20} cm^{-3}. The donor concentration in the ZnS layer adjacent to the junction should be much lower than the GaN acceptor concentration, in order to set up a wide barrier for electrons in the ZnS conduction band, hindering transport from the ZnS layer into the GaN layer.

McCaldin and Wang, and reported in Reference [12].

While the device modeling results indicate that the MgZnS electron blocking layer is successful in limiting the recombination to the sulfide layer, the basic ZnS/GaN structure can also be designed such that hole transport and recombination in the sulfide layer are favored. A diagram of the single heterostructure device under forward bias is shown in Figure 7.5. Referring to the figure, if the Mg doping concentration in the GaN layer adjacent to the interface is high, then the depletion layer in the p-GaN will be very narrow. This is easily the case, since typical acceptor levels in p-type GaN are approximately 10^{20} cm^{-3}. The barrier in the valence band will therefore be 50-100Å wide, allowing considerable tunneling of holes. If the doping concentration in the ZnS layer, on the other hand, is relatively lower, then the conduction band barrier will be very broad, and electrons will be hindered from transporting over into

the GaN layer, provided the conduction band barrier height remains large compared to kT. Therefore, hole current across the interface might be expected to dominate for a narrow range of forward bias (near 3 V) via hole tunneling. For higher forward biases, both electron and hole tunneling are expected to contribute to the total current across the junction; the electroluminescence spectrum would be contaminated by emission from the p-GaN layer in this case.

The ZnS layer is doped with a deep acceptor center ("activator") which tunes the luminescence wavelength. (A list of activator centers is presented in Table 7.1.) The ZnS layer is also doped with Al or Cl, shallow donors, to provide n-type conduction. When holes are transported into the ZnS layer, they become strongly bound to the deep acceptor centers (*e.g.*, Ag for blue, Cu for green) and recombine with electrons via a donor-acceptor pair transition. The concept is the same for all desired colors and wavelengths, depending only on the activator dopant. The device can also be made using a GaN/ZnS/ZnCdS structure. The lower band gap of ZnCdS allows luminescence to be achieved in the red and throughout the visible spectrum using Ag or Cu.

In the next chapter, efforts in the growth and fabrication of ZnS/GaN heterjunction light emitting devices are presented.

Bibliography

[1] C.N. King, *J. Vac. Sci. Technol. A* **14**, 1729 (1996).

[2] J. L. Castellano, *Handbook of Display Technology* (Academic Press, San Diego CA, 1992), Chapter 6.

[3] Y. Sato, N. Takahashi, and S. Sato, *Jpn. J. Appl. Phys.* **235**, L838 (1996).

[4] S. Yamaga, Physica B **185**, 500 (1993).

[5] T. Yokogawa and T. Narusawa, *Appl. Phys. Lett.* **61**, 291 (1992).

[6] B. J. Wu, L. H. Kuo, J. M. Depuydt, G. M. Haugen, M. A. Haase, and L. Salamancariba, *Appl. Phys. Lett.* **68**, 379 (1996).

[7] T. Yasuda, T. Yasui, and Y. Segawa, *J. Cryst. Growth* **159**, 447 (1996).

[8] M. W. Wang, J. O. McCaldin, J. F. Swenberg, T. C. McGill, and R. J. Hauenstein, *Appl. Phys. Lett.* **66**, 1974 (1995).

[9] S. Nakamura, N. Iwasa, M. Senoh, and T. Mukai, *Jpn. J. Appl. Phys.* **31**, 1258 (1992).

[10] H. Amano, M. Kito, K. Hiramatsu, and I. Akasaki, *Jpn. J. Appl. Phys.* **28**, L2112 (1989).

[11] C. Yuan, T. Salagaj, A. Gurary, P. Zawadzki, C. S. Chern, W. Kroll, and R. A. Stall, *J. Electrochem. Soc.* **142**, L163 (1995).

[12] J. O. McCaldin, M. W. Wang, and T. C. McGill, *J. Cryst. Growth* **159**, 502 (1996).

[13] announced at http : //www.storage.ibm.com/hardsoft/diskdrdl/micro/.

[14] Materials for Flat-Panel Displays, *MRS Bulletin* **21**, (1996).

[15] Y.A. Ono, *Electroluminescent Displays*, World Scientific, Singapore (1995).

[16] *Physics and Chemistry of II-VI Compounds*, edited by M. Aven and J.S. Prener (North-Holland, Amsterdam, 1967).

[17] W. Van Gool, Thesis, University of Amsterdam, January (1961).

[18] Materials used in Electroluminescent Displays, *MRS Bulletin* **21**, (1996).

Chapter 8 MBE Growth of ZnS and Fabrication of ZnS/GaN Light Emitters

8.1 Introduction

This chapter describes the growth of ZnS layers by molecular beam epitaxy and presents preliminary results for ZnS:(Al,Ag)/GaN:Mg blue light emitting diodes.

8.2 Molecular beam epitaxial growth of ZnS

While there have been many reports of ZnS grown by MBE on near lattice matched substrates such as Si [1, 2], GaP [3, 4, 5], and GaAs [6, 7, 8], with lattice mismatches of 0.4%, 0.8%, and 4%, respectively, little has been reported of epitaxial growth on the highly mismatched substrates GaN (~+20% mismatch) or Al_2O_3 (~-20% mismatch). The very large lattice mismatch makes it unlikely that the ZnS epilayer will grow coherently strained for more than one monolayer. More likely relaxation in the layers closest to the interface will result in dangling bonds and numerous misfit dislocations. In fact misfit dislocations in combination with tilting and 3D relaxation in a mosaic microstructrue are likely the most energetically preferred strain relaxation mechanisms [9]. On the other hand, GaN and ZnS are known to be good light emitters even when the defect density is high, so one might hope that this interface may allow sufficient hole transport to be a technologically useful junction even though it is likely to be heavily defected.

8.2.1 MBE system used for ZnS growth

Details about the ZnS growth procedures were originally presented in [10] and [11]. ZnS epilayers were grown in a modified Perkin-Elmer 430 molecular beam epitaxy

system. Essentially, the setup is similar to that shown in chapter 3, Figure 3.2. This system was equipped with a valved cracking source for sulfur (99.9999 % purity (6N)), standard 60 cc capacity Knudsen cell sources for elemental Zn (6N purity), Cd (6N), Al (6N), Ag (6N), $ZnCl_2$ (6N), and an autotuned radio frequency nitrogen (N_2 source gas purity 99.9995 % (5N5)) plasma source (Oxford Applied Research MPD21). Monitoring and *in situ* characterization was done with 10 keV RHEED gun and phosphor screen (Perkin Elmer), ionization gauge flux monitor, and RGA mass spectrometer (UTI 100C). The growth chamber maintains a base pressure during growth of 3×10^{-10} torr with liquid nitrogen cryopaneling fully cooled. Samples were either bonded with In to molybdenum holder blocks, or secured to similar blocks with Mo or Si clips. We found that In bonding provided better temperature uniformity and reproducibility than the use of clips. Temperatures were measured by thermocouple in direct contact with the back of the molybdenum holder block.

8.2.2 Sulfur in an MBE chamber: special considerations

Sulfur is a very peculiar material, dissimilar in many ways from the more common source materials used for molecular beam epitaxy. Of primary concern to growth is the vapor pressure of the material, its reactivity with components and other materials within the chamber, as well as operator safety concerns during system vents.

Valved cracker source

Sulfur has a very high vapor pressure for a solid, about 15 orders of magnitude higher than, for example, gallium. In fact, the vapor pressure of sulfur at room temperature is on the order of 10^{-6} torr. Thus if sulfur were used in a standard effusion cell and kept at an idle temperature of 20°C, it would be impossible to achieve high vacuum conditions within the MBE chamber. Also, the vapor pressure is too low for wall deposits to be quickly pumped away, as gas phase sources can be. This problem can be overcome by either using a ZnS compound source material for sulfur, or by the use of a valved cell. The valved thermal cracking cell that was used here solves this as well

as other problems. Species that desorb and evaporate from bulk sulfur in a vacuum tend to be long polymeric chains [12], or S_6 ring structures. The high temperature (typically 300-900°C) cracking tube breaks up these larger species into S or S_2, which are much more suitable for uniform growth of II-sulfide compounds. In this study, the sulfur cracking zone temperature was held at 700°C except where noted.

Sulfur reactivity with chamber components

Another concern when using sulfur inside an MBE system is the reaction and corrosion of sulfur with metal components and filaments. Fortunately, most stainless steel components such as the chamber walls, and filaments which are made of refractory metals such as tungsten or tantalum, have some resistance to corrosion by sulfidization. One component that is quickly corroded, however, are the copper gaskets commonly used to seal vacuum flanges. The Perkin-Elmer MBE chamber used in this study has literally dozens of flanges which require copper gasket seals. It was one of the major tasks in preparation for the growth of II-sulfides to rebuild the entire system, replacing every copper gasket with a gold-plated gasket. One micron (about 40 millionths of an inch) of high purity electro-plated gold on standard OFHC copper gaskets [13] was sufficient to inhibit corrosion of the gaskets.

Safety concerns

Great care must be taken when dealing with the toxic substances used for III-V and II-VI growth. Of particular danger are arsenic and arsine, used for growth of III-As compounds, and the heavy metals Hg, Cd, Te, and Se used in growth of II-VI materials. Sulfur must also be included on this list of hazardous substances. Although solid sulfur is relatively benign, the gaseous species hydrogen sulfide (H_2S) and sulfur oxide (SO_x) can be quite toxic for prolonged exposure in all but trace concentrations. When venting a vacuum system which has contained sulfur, preventive care must be taken to avoid inhalation of these gases. A powerful "rotten egg" smell can normally be detected when one is in the presence of H_2S or SO_x, but the nose quickly becomes desensitized if one remains in the contaminated area. A desensitized individual is

in increased personal danger since they no longer have any olfactory reflex telling him or her to leave the area. For these reasons, a gas sensor with a visual and auditory alarm capable of detecting H_2S and SO_x should be used while venting the sulfide MBE chamber. Additionally, gas masks with appropriate filters and "elephant trunk" ventilation systems should be used.

8.2.3 Growth procedure for ZnS films

Substrates

To develop and calibrate our ZnS growth capability, many samples were grown on sapphire (Al_2O_3) substrates. Sapphire was chosen because it is roughly twenty times less expensive than GaN epilayers grown by MOCVD, but has the common feature of being highly stable and presenting a large lattice constant misfit to ZnS. After the basics of growth were established on Al_2O_3, some growths were also carried out on GaAs substrates as well as both n- and p-type GaN.

Sapphire (0001) substrates were sourced from Union Carbide Crystal Products and GaAs (001) substrates were sourced from AXT (American Xtal Technology). The GaN substrates consisted of a 3 μm thick epilayer grown by metalorganic chemical vapor deposition (MOCVD) on c-plane sapphire (Emcore Corp. and Advanced Technology Materials (ATMI)). Van der Pauw Hall measurements performed on the p-type GaN layers indicated conductivity of $5\,\Omega$cm, a free hole concentration of $\sim 2 \times 10^{17}\text{cm}^{-3}$, and a Hall mobility of 7 $\text{cm}^2/(\text{V-s})$. Substrates were degreased in organic solvents and loaded into the MBE vacuum system. Before epilayer growth, the samples were transferred *in situ* between the growth chamber and an x-ray photoemission spectoscopy (XPS) analysis chamber. XPS analysis on the GaN layers revealed carbon surface contamination of atmospheric origin. It was found that the carbon could be removed by exposing the sample to an RF nitrogen soak at a substrate temperature of 500°C for approximately 20 minutes (Figure 8.1). The plasma operated at a chamber pressure of 1×10^{-6} torr and 200 Watts RF power. This treatment also visibly improved the RHEED pattern of the GaN, making the unre-

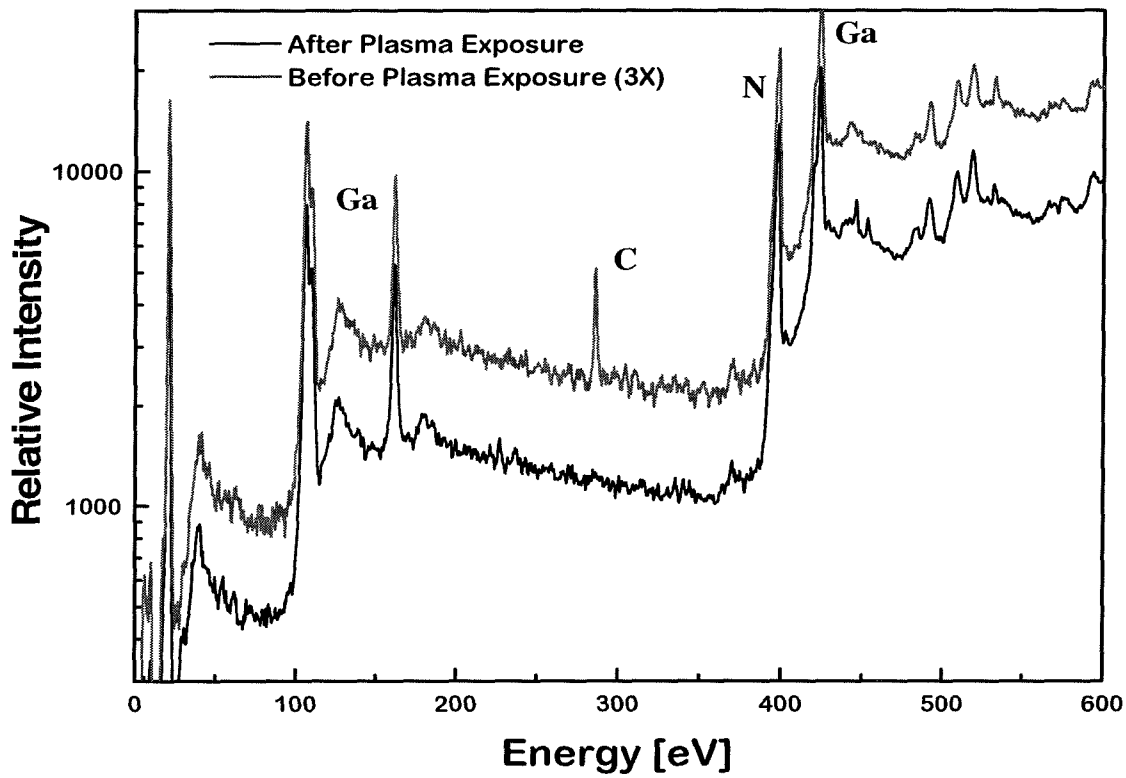

Figure 8.1: X-ray photoemission spectrum of GaN before and after exposure to *in situ* RF nitrogen plasma.

constructed streaks brighter and more distinct. Contamination could be reduced, but not eliminated, by thermal cleaning alone.

The sapphire substrates were thermally treated at 500°C for 30 minutes prior to growth, after which sharp RHEED streaks were manifest. We found that etching of substrates made no noticeable difference.

Growth orientation and RHEED observations

Prior to MBE growth all substrates showed sharp RHEED streaks. After opening the source shutters the RHEED pattern quickly became spotty for most films (Figure 8.2), indicating that growth proceeds in the 3D (Volmer-Weber) [14] mode, and remained spotty throughout the growth. Streaky patterns in the RHEED image were not observed for any growth condition, covering the range of substrate temperatures between 150°C - 400°C and source flux beam equivalent pressures (BEPs) of $(0.3 - 2.0) \times 10^{-7}$ torr. The spotty RHEED pattern also indicated that the ZnS crystalline orientation followed the template of the underlying substrate, and that the films are single crystalline or composed of mosaic crystallites which are aligned with the underlying substrate lattice. The ZnS films grown on hexagonal GaN (0001) and sapphire (0001) substrates were of the zincblende structure with (111) orientation, while films grown on GaAs (001) substrates were zincblende with (001) orientation. Most films displayed twinning in the (111) growth plane (Figure 8.2B) which is commonly observed for growth on a (111) oriented substrate [8, 3], although this twinning was absent and replaced by $(11\bar{1})$ twins for some films grown with a lower sulfur cracking temperature of 300°C (Figure 8.2C). Films grown at the higher temperature of 400°C showed no visible twinning (Figure 8.2A) [15] and show superior surface morphology, although they suffer from extremely low growth rates (Figure 8.3). Ring-like patterns were observed for films grown at very low temperatures or with poor surface preparation, indicating polycrystalline growth. The RHEED image also indicated that the zincblende ZnS grows at a 30 degrees rotated orientation to the sapphire substrate lattice. That is, the (111) faces of ZnS parallel the (0001) faces of Al_2O_3 and the $[1\bar{1}0]$ azimuth points along the $[10\bar{1}0]$ direction (Miller-Bravais notation) of

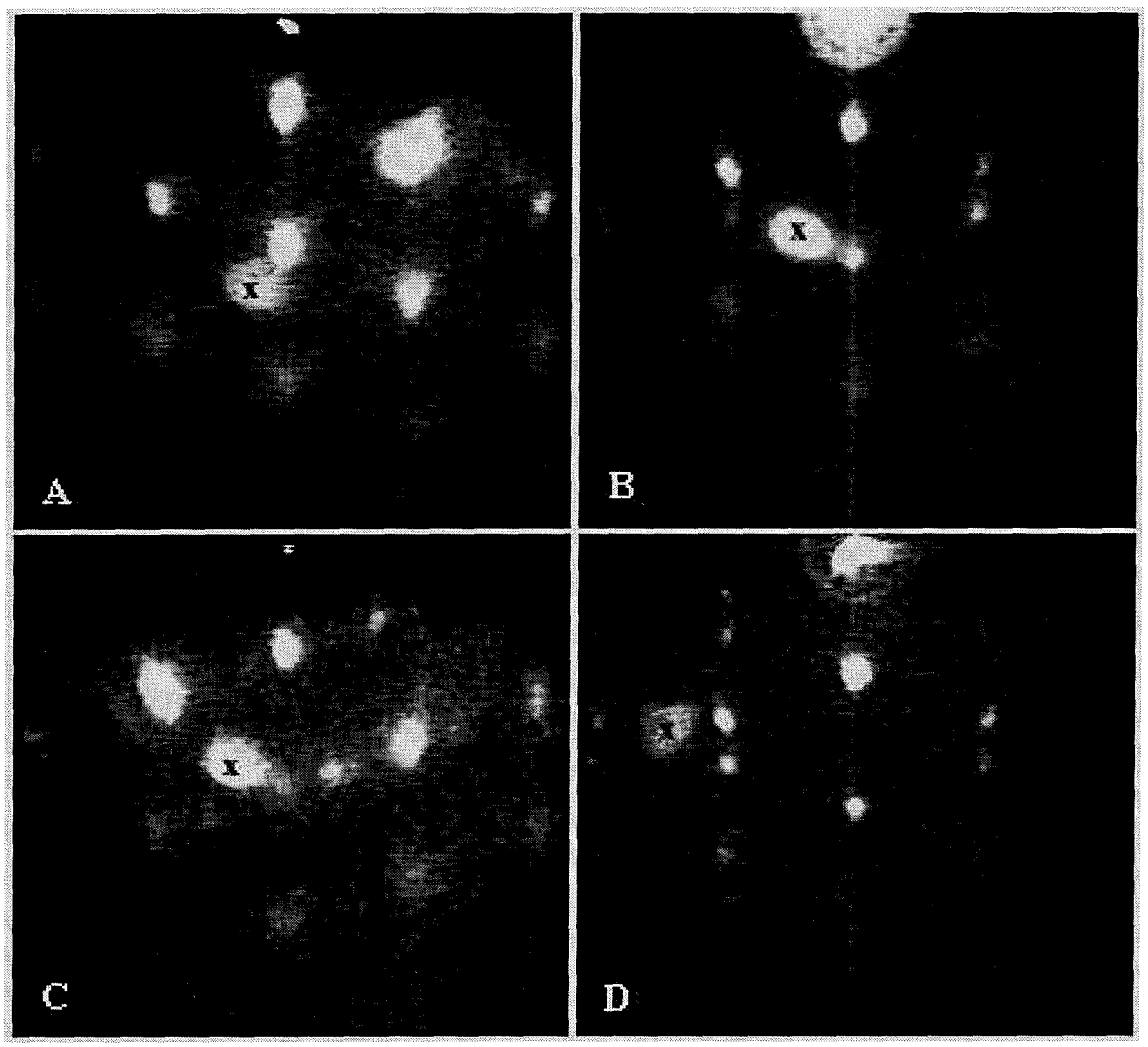

Figure 8.2: 10keV RHEED images ($(1\bar{1}0)$ azimuth) of ZnS on sapphire (A) grown at 400°C with no visible twin spots, (B) grown at 250°C with sulfur cracking zone temperature of 700°C and showing (111) twins, (C) grown at 250°C with cracking zone at 300°C showing $(11\bar{1})$ twins, and (D) ZnS:Al,Ag grown on GaN ((111) twinned). The smudge common to all pictures is due to a defect in the phosphor screen (x).

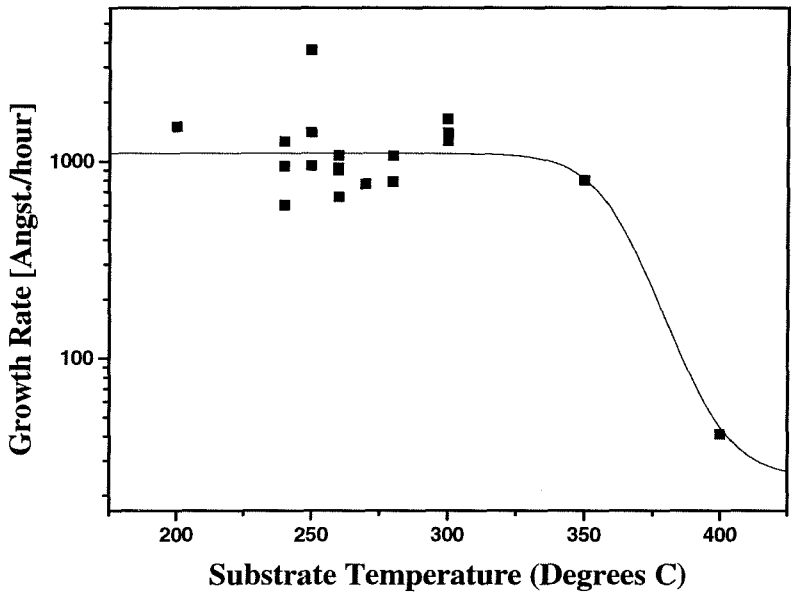

Figure 8.3: Temperature dependence of the growth rate of ZnS on sapphire (0001). The line is meant to guide the eye.

the Al_2O_3. GaN has also been observed to grow in this 30 degrees oriented state on sapphire (0001). The ZnS films were not rotated with respect to the GaN and GaAs substrates.

8.3 Optical and structural characterization of ZnS thin films

After the MBE-grown ZnS layers were removed from the vacuum system, they were characterized by a variety of means. Film thicknesses were measured by depth profiler and by spectroscopic ellipsometry, and growth rates were calculated assuming a constant rate throughout the growth period. Figure 8.3 shows the calculated rates as a function of growth temperature. Rates of up to 0.4 μm per hour were observed for the lower growth temperatures, with rapidly diminishing rates for temperatures above 350°C. This trend is in agreement with other work [3, 1, 8]. A typical film thickness was 600 nm.

8.3.1 Structural properties of MBE-grown ZnS films

The structural quality of the ZnS films was evaluated using high resolution x-ray diffraction analysis and SEM in electron channeling pattern mode. The high resolution x-ray diffraction analysis was performed using a four crystal (Ge (220)) diffractometer and Cu Kα x-rays. Results show that diffraction peak widths are significantly broadened by misfit dislocations and by the presense of mosaic crystalline domains which are slightly tilted and rotated from one another. Such mosaic films are commonly observed in other materials systems where large lattice mismatch exists, such as Si on Al_2O_3 and GaAs on Si. The full width at half maximum (FWHM) of (111) peaks were consistently close to 270 arcsec for $\omega/2\theta$ scans, invariable with growth conditions. X-ray rocking curves (ω scans) showed peak widths of up to several degrees, depending on growth temperature, film thickness, and doping (Figure 8.4). The FWHM of ω scans provides an indication of the degree of mosaic tilting that is present in the film. Undoped samples grown at 400°C showed the best as grown rocking curve FWHM of approximately 60 arcminutes. Further improvement in crystalline quality was obtained by post-annealing at 1000°C in a high pressure sulfur environment, the results of which are presented in section 8.4 [16].

Some films were characterized by scanning electron microscopy (SEM) operating in electron channeling pattern (ECP) mode. The ECP scans are useful as an indication of crystal symmetry, quality, and orientation. Channeling patterns were not visible for as grown films grown at substrate temperatures below 400°C, which indicates that the structural quality of these films is poor. A typical electron channeling image for a post-annealed sample (see section 8.4.2) is shown in Figure 8.10. As confirmed by RHEED observations, the scan shows that the zincblende ZnS grows at a 30 degrees rotated orientation to the sapphire substrate lattice. The degree of detail visible in the ECP indicates good crystal quality.

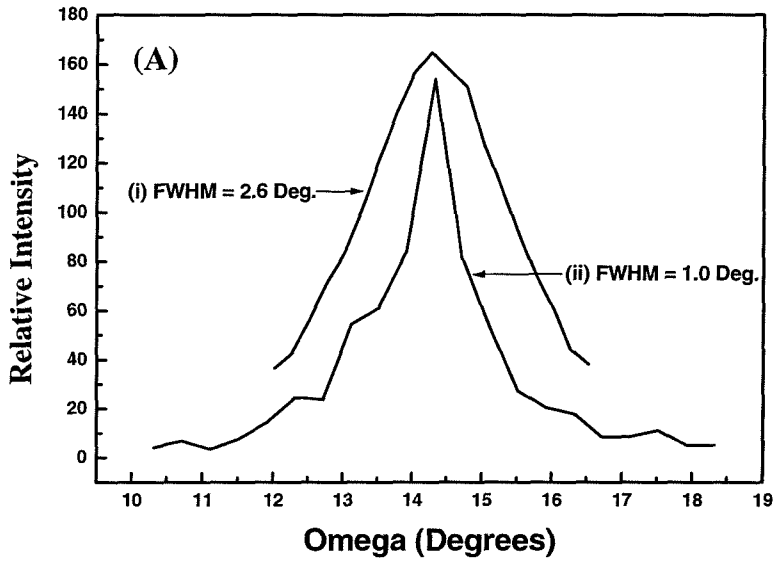

Figure 8.4: X-ray rocking curves for ZnS grown on sapphire at (i) 250°C and (ii) 400°C.

8.3.2 Doping of ZnS with aluminum and silver

The band gap of ZnS is too wide for band-to-band luminescence to be in the visible spectrum, so impurities (dopants) must be introduced in order to form deep levels within the band gap by which the radiative recombination can be brought from the ultraviolet into the visible range. As was shown in Table 7.1, there have been many doping species evaluated for this task, which span the visible spectrum. In this work, our target is a light emitter that could be used as the blue component of a RGB display system. This corresponds to a wavelength requirement of approximately 450 nm which can be satisfied using silver atoms as deep recombination centers, in combination with either aluminum or chlorine as a shallow donor to make the layers conductive. The doping of ZnS with silver was, along with achieving high structural quality films, one of the major efforts of this research. Along with silver, n-type doping was done with aluminum, although chlorine doping was also attempted several times using a $ZnCl_2$ compound source but with no success.

A relatively large number of ZnS films were doped with Al or codoped with Al and

Ag. These growths were done with the aim of optimizing the blue luminescence of the films. Aluminum, under the right conditions, is a shallow donor in ZnS. The Al-doped ZnS can luminesce blue (without silver codoping) because it can be "self-activated," that is, luminescence is via a donor-acceptor-pair (DAP) transition between the Al donor and a deep native point defect such as a Zn vacancy [17, 18].

For codoped films, the radiative transition is a DAP transition from the Al donor to the Ag acceptor. For fabrication of diode structures, the most intense and spectrally pure luminescence is desired, limited by the requirement that the films should be n-type. Thus the doping concentrations of the Al and Ag are very important, as is their relative abundance. The criterion for n-type conduction requires that the concentration of Al donors be higher than the concentration of Ag acceptors, while the luminescence intensity increases as the concentration of both Al and Ag increase, up to a certain point. If too much Al and Ag is put into the film (more than about 10 ppm) the crystalline quality of the ZnS becomes poor, and precipitates start to form.

8.3.3 Optimization of 450 nm blue luminescence

A very useful qualitative tool in the optimization of ZnS doping is observation of cathodoluminescence from the RHEED electron gun. Our MBE growth chamber is equipped with a line-of-sight viewport through which can be seen the e-beam induced luminescence. When the growth and doping concentrations are within the correct window, bright blue luminescence can be clearly seen by eye. With some experience, the saturated blue Al-Ag luminescence at 450 nm can be discerned from the more blue-green "self-activated" luminescence which occurs when the Al concentration is much higher than the incorporated Ag. Using the RHEED beam cathodoluminescence, growth conditions can be adjusted real-time for optimum doping levels and luminescence intensity.

8.3.4 Low temperature PL study of ZnS grown on GaN substrates

Since ZnS films for LEDs have to be grown on GaN substrates, we studied low temperature PL of ZnS grown on GaN substrates and compared them to the ZnS films grown on sapphire. Variable temperature PL data was collected using a home-built system which uses a Liconix He-Cd laser excitation source operating at 325 nm, and a Janis liquid helium dewar in which the sample was mounted. Luminescence was collected with lenses and focused into a SPEX 1269 spectrometer. Spectrally separated light was then collected by a Hamamatsu R943 photomultiplier tube (PMT) in a thermoelectrically cooled PMT housing (Products for Research). The spectrometer position was controlled using a SPEX CD-2B compudrive and a PC was used for data acquisition.

Low temperature (5 K) PL scans of ZnS samples doped with Al and Ag grown on *p*-type GaN, *n*-type GaN and sapphire substrates are shown in Figure 8.5a, b and c, respectively. All samples produced bright blue luminescence. Visible are the two characteristic silver activator bands: silver high (390 nm) and low (440 nm) energy emission centers [18]. The relative intensities of these two bands are known to be influenced by sample preparation, especially the relative amounts of Al and Ag doping [18]. In the samples studied, both bands are present for the ZnS:(Al,Ag) film grown on sapphire as shown in Figure 8.5c, while the lower energy band dominates for the films grown on *n*-type GaN (Figure 8.5b). Films grown on *p*-type GaN show emission predominantly near the high energy (390 nm) band (Figure 8.5a). In the case of ZnS films grown on GaN, it is not possible to exclude GaN substrate luminescence. For example, the *p*-type GaN has luminescence in the blue-violet region (section 3.6.2) which overlaps with the high energy (390 nm) silver band. Also, in Figure 8.5b phonon replicas (370-400 nm) can be observed of the eA (conduction band to deep acceptor) transition of the GaN.

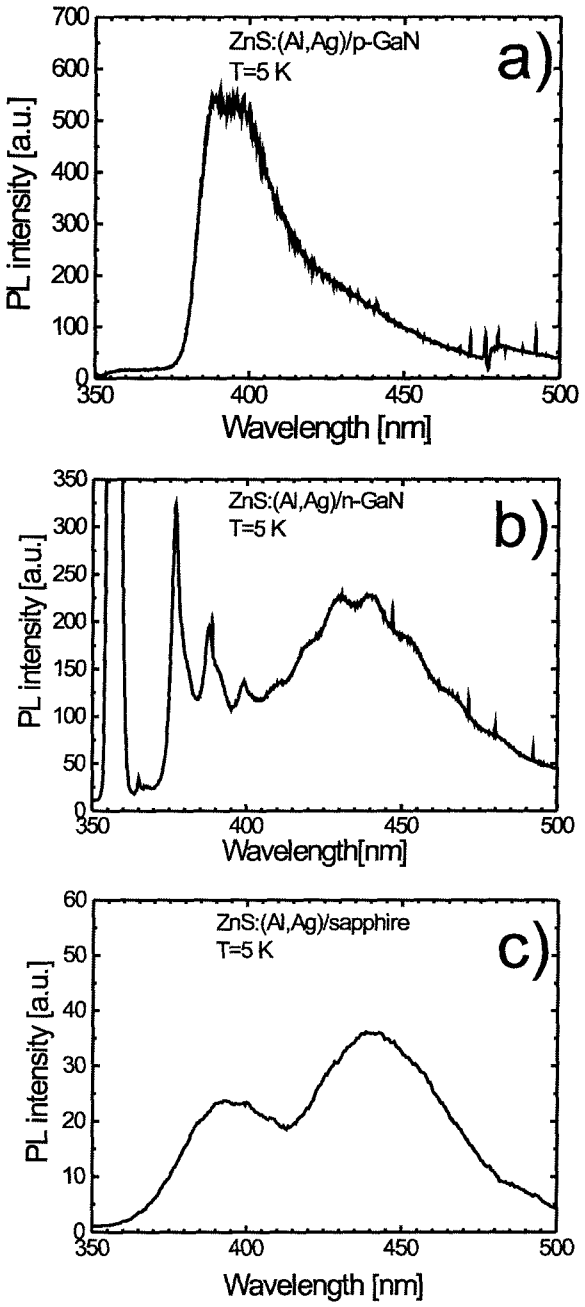

Figure 8.5: Low temperature (T =5 K) PL scans of n-type ZnS doped with (unoptimized) Al and Ag on a) p-type GaN substrate b) unintentionally doped n-type GaN substrate and c) sapphire substrate. The spectra shown in a) likely contains features from the GaN substrate, since the Mg-doped GaN film also luminesces in the violet ($380 - 420$ nm) region (see section 3.6.2). The silver luminescent center is known to emit at high (380 nm) and/or low (450 nm) energies, depending on the sample preparation. Peaks for both of these transitions are evident in the spectra shown in c).

8.3.5 Correlation between structural and optical properties of ZnS

The correlation between structural and optical properties of ZnS was studied for films grown on sapphire (0001), GaN (0001) and GaAs (001) substrates. These ZnS films were characterized by high resolution x-ray diffraction (HR-XRD) and photoluminescence (PL). Room temperature PL scans of ZnS films grown on sapphire (0001), GaAs(001) and GaN (0001) substrates are shown in Figure 8.6A. These samples were doped with Al and Ag and grown in the same growth run (II-411) by simultaneously bonding the three substrates to a Mo holder block. All samples produced bright blue luminescence centered around 450 nm, which is the desired luminescence line characteristic of the silver activator low energy emission band [18]. The laser excitation power density was estimated to be $2.5\,\mathrm{mW/cm^2}$ from the focused spot size and the measured output power of the laser beam. We notice from Figure 8.6A that ZnS grown on GaN has the smallest luminescence intensity. The optical quality of the films clearly is dependent on the structural quality, as can be observed from Figure 8.6B, which shows x-ray rocking curves for the same set of samples. The ZnS film grown on GaN displayed the smallest peak intensity and the largest full width at the half maximum (FWHM) of the x-ray rocking curve, indicating the highest degree of misorientation (mosaicity) in the film and thus the worst structural quality. The correlation between optical and structural properties can perhaps best observed from Figure 8.6C, which directly compares integrated photoluminescence (over the measured wavelength range) and FWHM of the x-ray rocking curves. Clearly, films with wider FWHM of the x-ray rocking curve, and therefore larger mosaicity and lower structural quality, also had smaller integrated luminescence. It is interesting to observe that although the absolute values of lattice mismatch for GaN and sapphire substrates are similar ($\approx 20\,\%$), the ZnS films grown on sapphire have better optical and structural properties. It is important to note that the luminescence of the ZnS film grown on GaN substrate, although smaller when compared to films grown on GaAs and sapphire, is still bright enough to be easily observable by eye in the

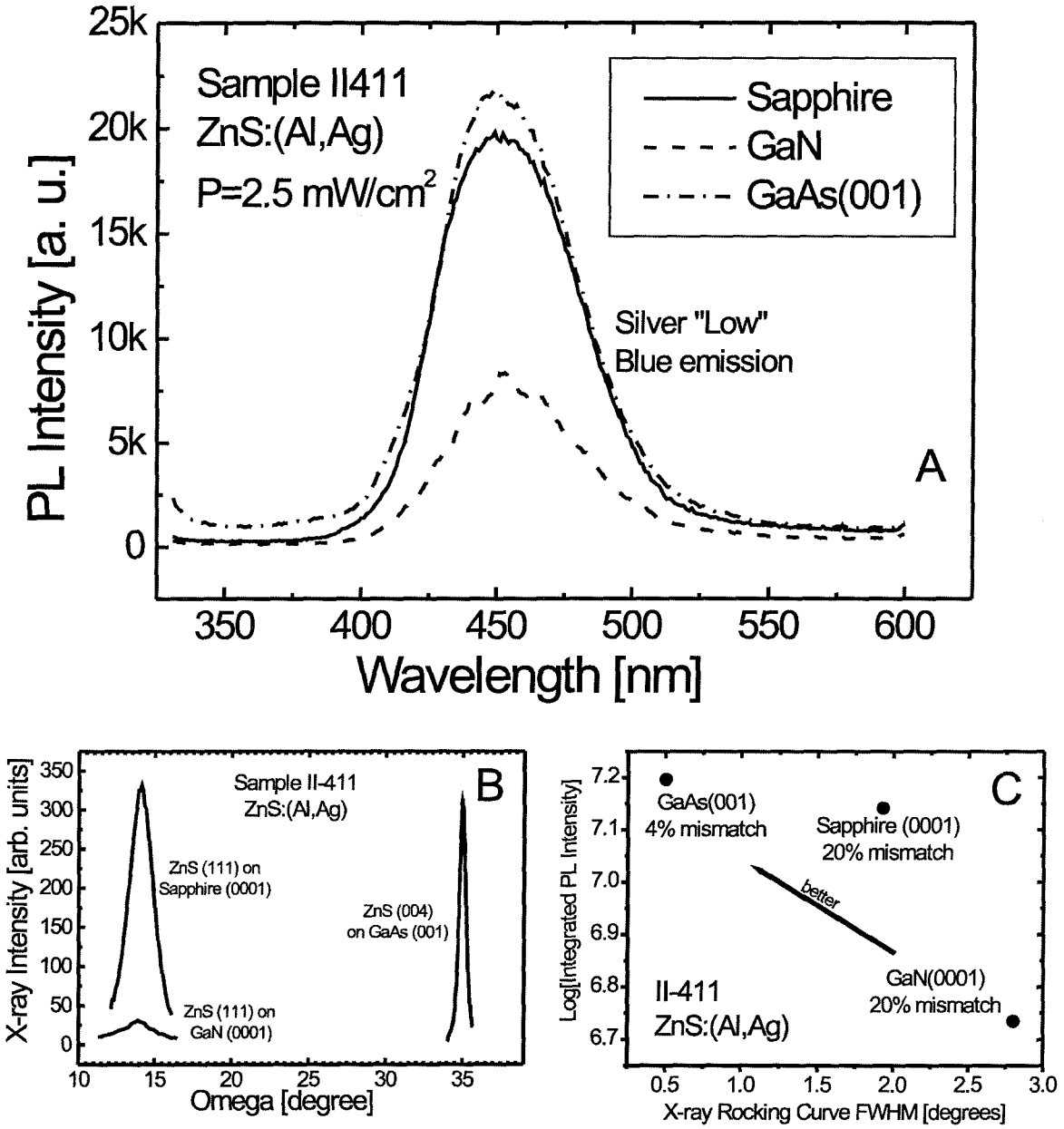

Figure 8.6: A) Room temperature PL scan of ZnS films (samples II-411) grown on sapphire, GaAs and GaN substrates. All samples were doped with Al and Ag and grown concurrently. The PL peaks are centered around the characteristic low energy silver emission band at 450 nm, but of different intensity, indicating a variation optical quality. B) High resolution x-ray diffraction scans of the same sample series. C) Integrated photoluminescence intensity plotted vs x-ray width. The increased structural and optical quality of the film grown on the GaAs substrate, which has the least mismatch, is evident.

laboratory room with the light on.

8.4 High pressure solid phase recrystallization of ZnS thin films

In this section we discuss the solid phase recrystallization (SPR) of undoped, $0.3 - 0.5\,\mu$m thick, MBE-grown (111)-oriented cubic ZnS films on sapphire. These samples were recrystallized by annealing at temperatures in the $825-1000\,^{\circ}$C range, at sulfur overpressures of 10 atm. Thermal annealing at large sulfur overpressure consistently improved the structural properties of the films, thereby compensating the effects of large substrate mismatch. Previous efforts on the recrystallization of thin films are described in Reference [18]. Presently, recrystallization is an important industrial process, and plays a vital role in the manufacture of steel and aluminum [19], and HgCdTe [20]. Solid phase recrystallization of bulk ZnSe, CdTe and CdSe was recently successfully demonstrated by Triboulet, *et al.* [21, 22], by annealing at high temperatures under high column VI element overpressure, and excellent optical and structural properties were obtained [23]. The recrystallization experiments described here were performed by Z. Bandić.

8.4.1 Experimental details

To contain the ZnS samples and sulfur during the experiment, quartz ampoules with 2 mm-thick walls were used. Prior to the experiment, the ampoules were cleaned with organic solvents (acetone and isopropyl alcohol) and then baked at $1000\,^{\circ}$C for $2-4$ hours. The MBE-grown undoped ZnS/sapphire films were placed in the ampoules together with $100-200$ mg of 99.9999 % purity sulfur. The amount of sulfur placed in the ampoule was calculated according to the van der Waals equation of state, so that gas pressure of 10 atm is reached on the anneal temperature. The ampoules were then attached to a turbo-molecular pump to attain a vacuum of $1 \cdot 10^{-6}$ torr, and then sealed while the pump was still running (see Figure 8.7). The sealed ampoules

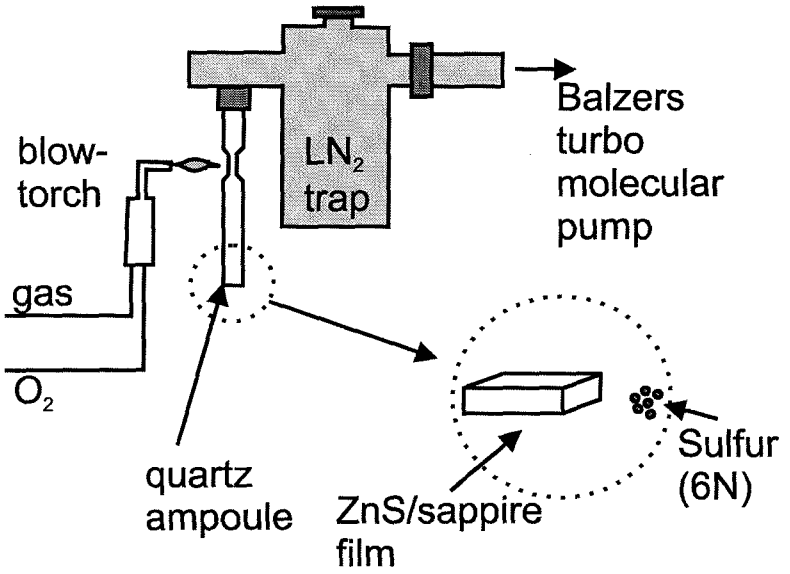

Figure 8.7: Schematics of the experimental setup used to vacuum-seal quartz ampoules containing ZnS thin films and sulfur. The ZnS and sulfur were placed in cleaned and baked ampoules, and ampoules were attached to the Balzers turbo-molecular pump through liquid nitrogen trap. Liquid nitrogen trap was used to prevent streaming of sulfur into turbo pump. The air was evacuated to attain vacuum level of $1 \cdot 10^{-6}$ Torr. The ampoules were then sealed while the pump was still running.

were then transferred into the temperature-controlled furnace. The temperature was slowly increased at the rate of $2-3\,^{\circ}$C/min to avoid thermal strains, until the final temperature in the $825-1000\,^{\circ}$C range was achieved. After the samples were kept at this temperature for $2-20$ hours, the temperature was slowly reduced at the rate of $2-3\,^{\circ}$C/min, again to avoid thermal stressing.

8.4.2 Structural characterization

High resolution x-ray diffraction

Samples were characterized before and after the annealing by high resolution x-ray diffraction (HRXRD). The ω and $\omega/2\theta$ scans around the ZnS thin film (111) reflections were performed in the 4 or 6-crystal mode (without or with Bonse-Hart collimator in front of the detector) respectively, using Ge(220) reflections.

To characterize the effects of different anneal temperatures, one sample (II391) was

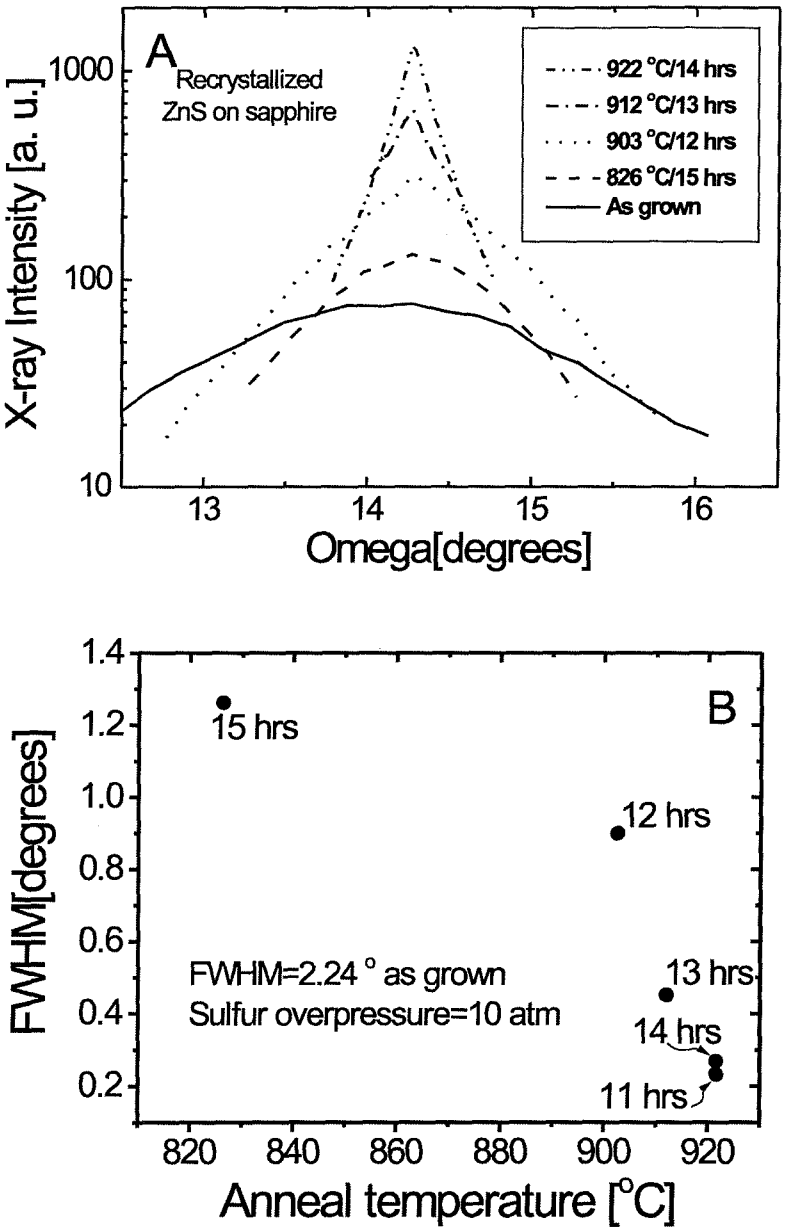

Figure 8.8: A) Summary of x-ray ω-scans for different recrystallization temperatures of sample II391. The curves for samples recrystallized at higher temperatures have lower widths and higher maximum intensity. B) The width of the x-ray rocking curve is plotted as a function of annealing temperature. The most dramatic improvements occur above 900°C.

cut into 5 pieces, and each was annealed at a different temperature between 825 °C and 922 °C. The anneal temperature must be chosen below the melting temperature, but high enough so that the original grain boundaries become unstable. At that point, the conditions are favorable for the migration of grain boundaries and growth of defect-free nuclei. The anneal time ranged between 11 and 15 hours, and sulfur overpressure was kept constant at 10 atm. The x-ray ω-scans (Figure 8.8A), and the full width of the half maximum (FWHM) of the curves as a function of temperature (Figure 8.8B) show that the crystalline mosaicity is significantly reduced at anneal temperatures above 900°C.

The typical FWHM of $\omega/2\theta$ curves for the samples in the II-391 series after recrystallization was approximately 50 arcsec as measured in the 6-crystal configuration. It was not possible to use this particular configuration before recrystallization, because of low diffracted x-ray intensity caused by poor film quality. Measured with the 4-crystal configuration, the typical width before recrystallization was approximately 270 arcsec ($\sim$ 450 arcsec was typically measured, but there is a correction of 180 arcsec for the slit width). The set of ω and $\omega/2\theta$ x-ray rocking curves of the sample II-366 before and after recrystallization at 970°C is shown in Figure 8.9. Ten-fold improvement in crystalline quality can be observed.

Scanning electron microscopy: electron channeling

Electron channeling patterns (ECP) are images formed by electron diffraction in a SEM, analogous to Kikuchi patterns which can be obtained in a transmission electron microscope. Electron channeling patterns (ECP) for GaN and ZnS layers were obtained in a JEOL 6400V scanning electron microscope (SEM). The pattern for sample II366, recrystallized at 970 °C for 3 hours at sulfur pressure of 10 atm, is shown in Figure 8.10. The corresponding ω and $\omega/2\theta$ scans, before and after recrystallization, are shown in Figure 8.9.

It was not possible to obtain visible ECP's for most samples before they were recrystallized due to the large number of defects and relatively poor quality of the films. In Figure 8.10 fine structure can be observed in the ECP, where each line cor-

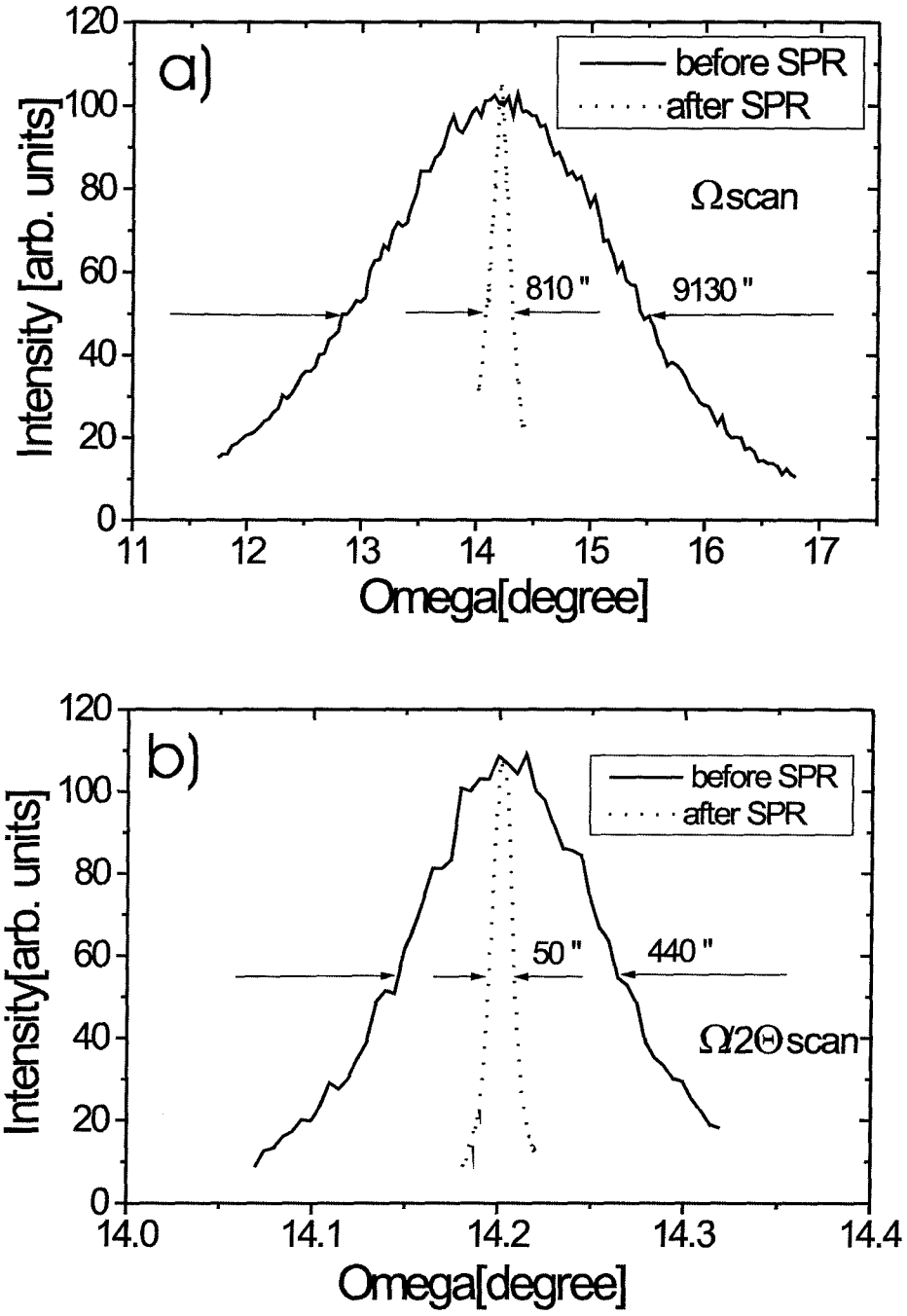

Figure 8.9: The ω and $\omega/2\theta$-scan x-ray curves of the sample II366 before and after recrystallization process. The anneal temperature was 970°C and the sulfur overpressure 10 atm. The maximum intensities of the curves in the case of the recrystallized sample have been reduced to the maximum intensity of the initial curve, so that curve widths can be compared.

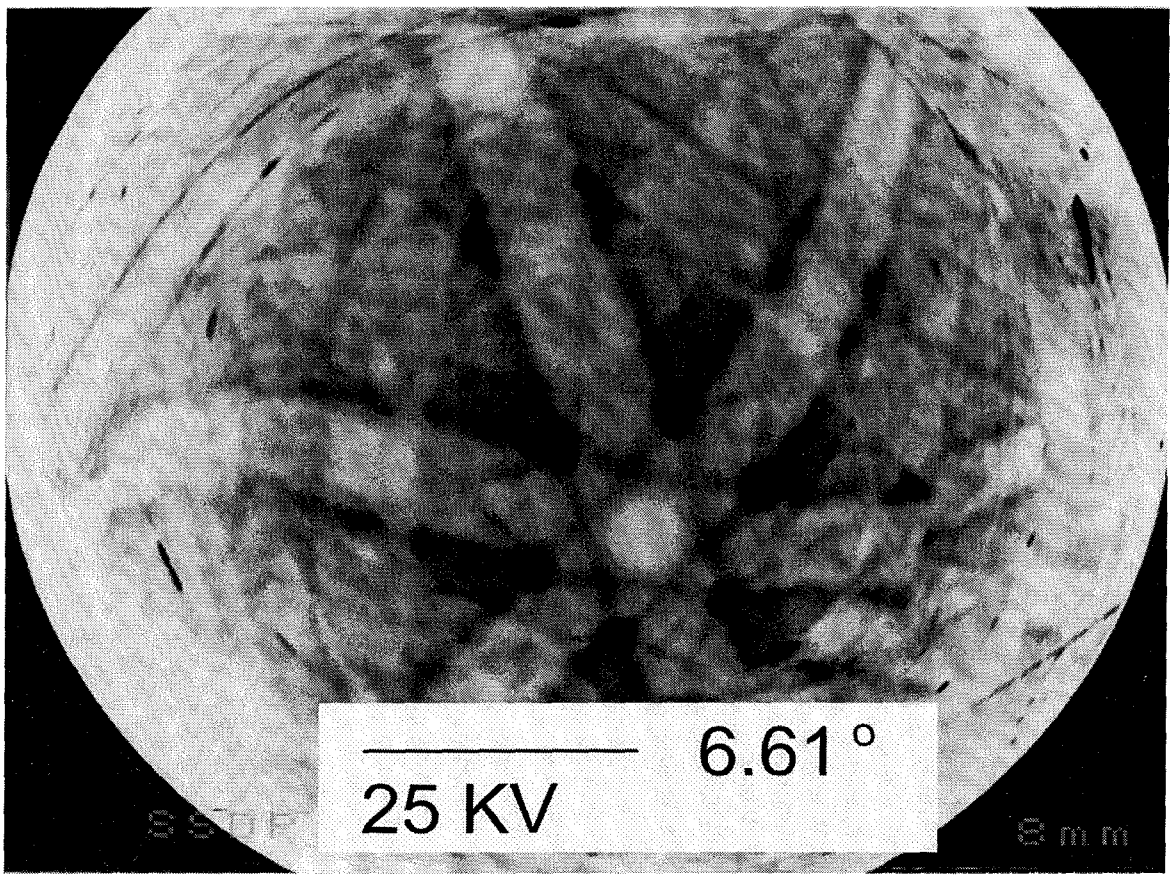

Figure 8.10: Electron channeling pattern of the sample II366, recrystallized at 970 °C for 3 hours at sulfur pressure of 10 atm. The 3-fold symmetry of the pattern indicates cubic crystalline lattice and that no phase transition occurred. The fine structure in the pattern confirms good crystallinity of the sample. (ECP scan by Z. Bandić.)

responds to the set of crystalline planes reflecting or absorbing high energy electrons. The high level of detail on this image indicates good crystallinity, in agreement with the x-ray measurements. The pattern has three-fold symmetry, indicatative of the cubic (zinc blende) polytype, and confirms that no phase transition to the hexagonal crystal modification (which would have six-fold symmetry) occurred.

The changes in surface morphology of the recrystallized samples have been investigated with the SEM. For most of the samples, the surface morphology after recrystallization remained smooth, which is important for device processing. However, on some samples recrystallized at higher temperatures we observed hexagonal pits (see Figure 8.11). One possible reason for the formation of pits at higher recrystallization temperatures is excess crystalline volume associated with large density of defects. During the recrystallization process and boundary migration, the annihilation of defects takes place, during which volume of the crystal reduces resulting in the pit formation. At lower temperatures, however, the boundary migration is slower and crystal relaxation times larger, which leads to fewer or no pits formed.

8.4.3 The role of sulfur

The role of the sulfur gas overpressure in the recrystallization experiment is manifold. First, the high sulfur overpressure greatly reduces zinc partial pressure, and thus prevents the evaporation of the ZnS film. Second, the sulfur-rich stoichiometry produces grain boundaries enriched by fast diffusing sulfur, which helps grain boundary migration. The large solubility of the chalcogen in the chalcogenides was accounted for to explain the result that bulk ZnSe recrystallization cannot be achieved under zinc overpressure [21]. In addition, we hypothesize that sulfur might also play an important role at the ZnS/sapphire interface. The significant difference between recrystallization of thin films and bulk is the large mismatch-related energy accumulated at the interface, which should reduce grain boundary mobilities. One possible route for the relaxation of this energy is a sulfur-rich ZnS/sapphire interface. A sulfur-terminated sapphire surface might become similar to a "quasi van der Waals"

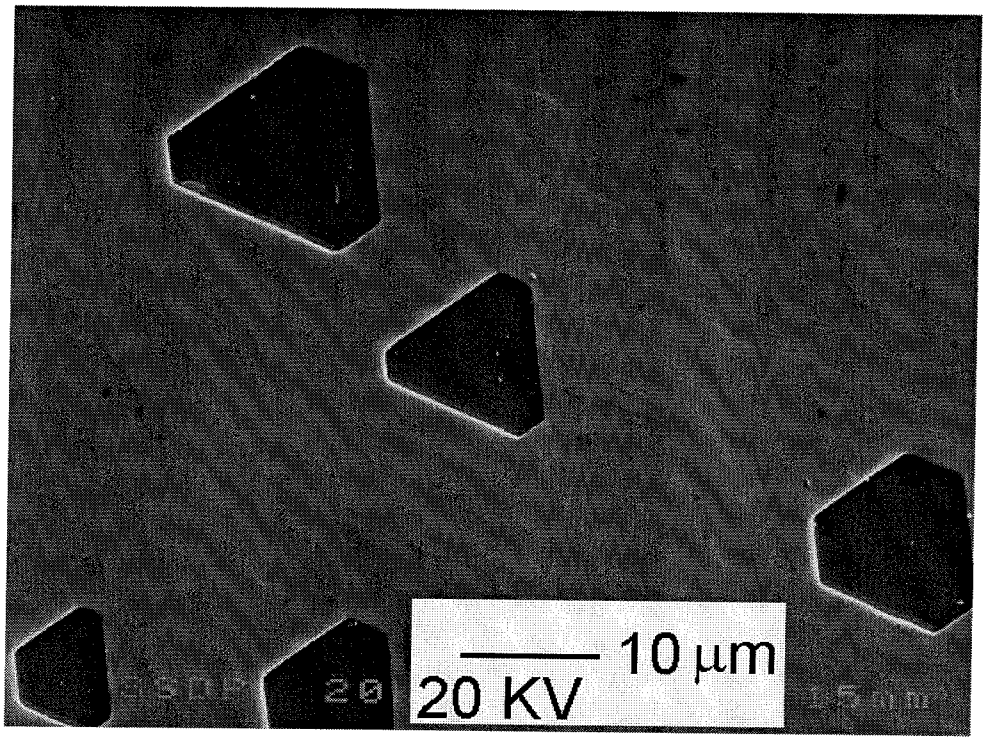

Figure 8.11: Surface of the sample II391 recrystallized at 922 °C. The change in the surface morphology in form of hexagonal pits can be observed. (SEM scan by Z. Bandić.)

bonding configuration, similar to a selenium-terminated GaAs surface [27]. Weaker interface bonding could change the interface structure, assist boundary migration and provide compliancy to the sapphire substrate.

8.5 Fabrication of *p*-GaN/*n*-ZnS blue light emitting heterostructure devices

8.5.1 Device processing

Devices were fabricated using standard photolithographic processes. The insulating sapphire substrate necessitated the use of lateral electrical contacts. The fully processed structure is shown in Figure 8.12. An aluminum top contact was first sputter deposited, following the methods of chapter 6, on the as-grown ZnS:Al,Ag/GaN:Mg layers. Mesas were then patterned and the Al and ZnS layers were etched in a solution of Br:HBr:H_2O (1:100:100), which was found not to etch the GaN. Gold *p*-type contacts were then patterned and deposited using a lift-off process. It is not believed that either contact is completely non-rectifying or of low resistivity. The effects of annealing on the dot-to-dot current-voltage curves for *p*-GaN/Au contacts were observed on a separate substrate, and the results are presented in Figure 6.5. As deposited, it is seen that the contacts are highly rectifying, and do not become fully ohmic even after annealing at 780°C.

8.5.2 Prototype device results

Current-voltage characteristics

The current-voltage measurement of the preliminary *p*-*n* device is shown in Figure 8.13. It shows diode-like behavior, although the non-ideal effects of high series resistance and rectifying contacts are evident. Turn on voltage is seen to be approximately $3-4$ V, which is expected as it corresponds to the band gap of the materials. At low applied voltages ($3-10$ V), luminescence is observed by eye to be a pale blue

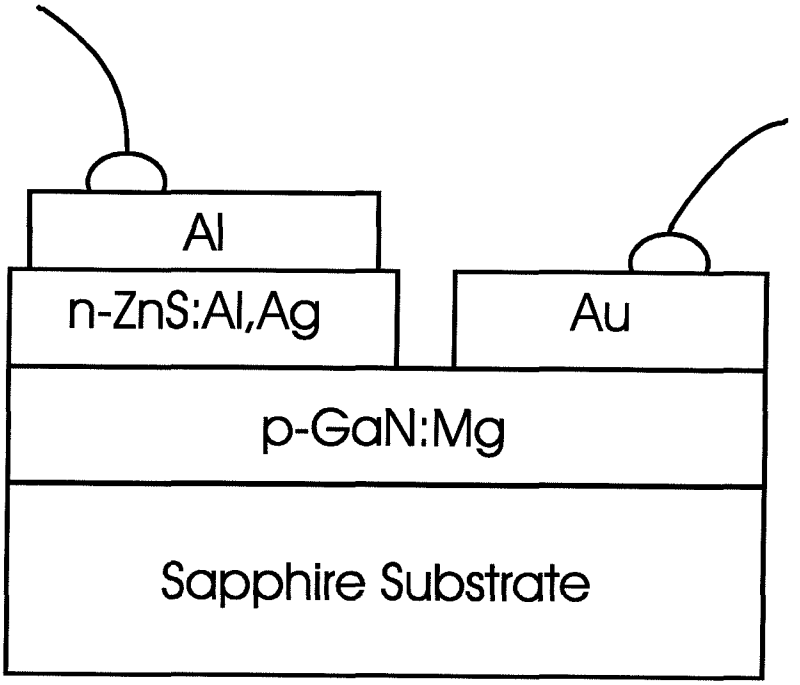

Figure 8.12: Schematic of the fabricated ZnS/GaN LED. Aluminum and gold were used as ohmic contacts for n-ZnS and p-GaN layers respectively.

similar to the hue observed for the sample the PL spectrum of which is shown in Figure 8.5b. The devices are bright enough during room temperature operation to be seen with the room lights on with 1 mA current applied. The expected non-uniformity of luminescence due to current spreading was observed. Additionally, "bright spots" were seen which may be caused by defects or thickness variations in the ZnS layer. As forward bias is increased, light appears more violet colored, similar to low temperature ZnS/p-GaN PL (Figure 8.5a) and the bright spots become more pronounced and similar to those reported for microplama breakdown in p-GaN [28].

Electroluminescence

LED devices were mounted on a die package with epoxy and wire bonded. The electroluminescence from biased devices was then focused on the entrance slit of the SPEX spectrometer and the electroluminescence (EL) spectrum was measured. The EL scan as a function of device bias is shown in Figure 8.14a. At low applied voltages between 3 and 10 V, luminescence is quite broad and centered around $390 - 400$ nm.

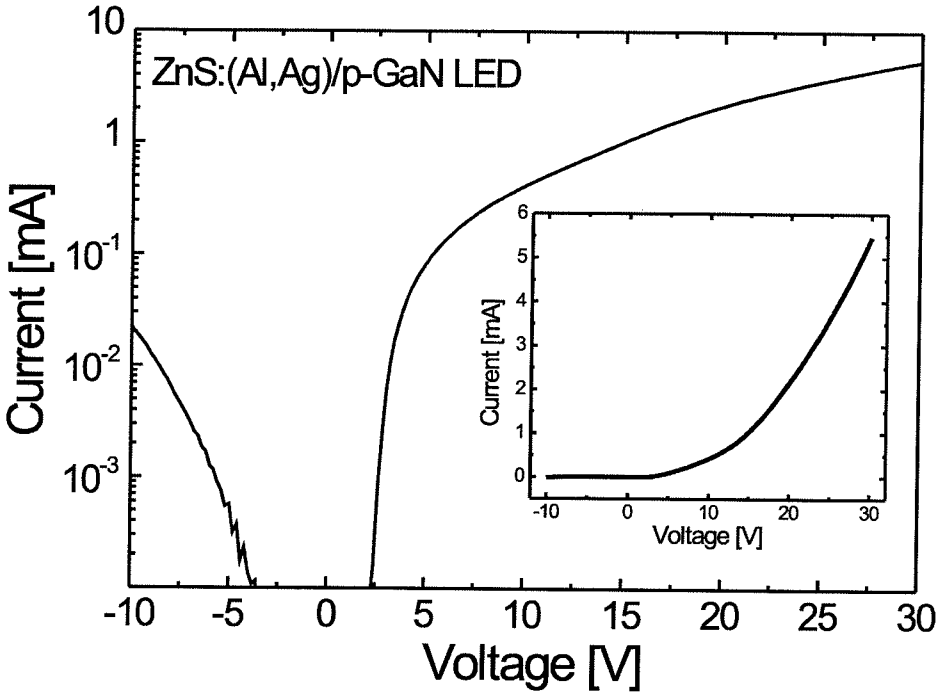

Figure 8.13: Current-voltage characteristics of ZnS:(Al,Ag)/p-GaN diode on the logarithmic-linear scale. The turn-on voltage is approximately $\approx 3 - 4\,\mathrm{V}$. Inset shows the same characteristics on a linear-linear scale.

At higher voltages between 10 and 25 V luminescence is shifted to higher energies and is centered around $385 - 390$ nm. It is not trivial to exactly analyze the luminescence mechanism, since broad PL spectra of both the p-type GaN:Mg and the n-ZnS:(Al,Ag) have peaks in the 390 nm region (see Figure 8.5). Since these preliminary devices did not include any electron blocking layer at the ZnS/GaN interface, it is possible and perhaps likely that electrons injected from n-ZnS into p-GaN recombine with holes, and produce luminescence typical of p-GaN. Other mechanisms may also contribute to the EL spectrum, for instance radiative recombination in either layer may be followed by absorption and fluorescence in the other layer. Also, luminescence at high biases may be linked to avalanche generation processes or microplasmas [28]. We can also observe from Figure 8.14 that at large forward biases above 15 V, integrated electroluminescence saturates, which may indicate that injection has become space-charge limited or that the device is heating up.

Some of the practical problems in the fabrication of the ZnS/GaN LEDs were poor ohmic contacts and lack of a suitably conductive GaN substrate. Ohmic con-

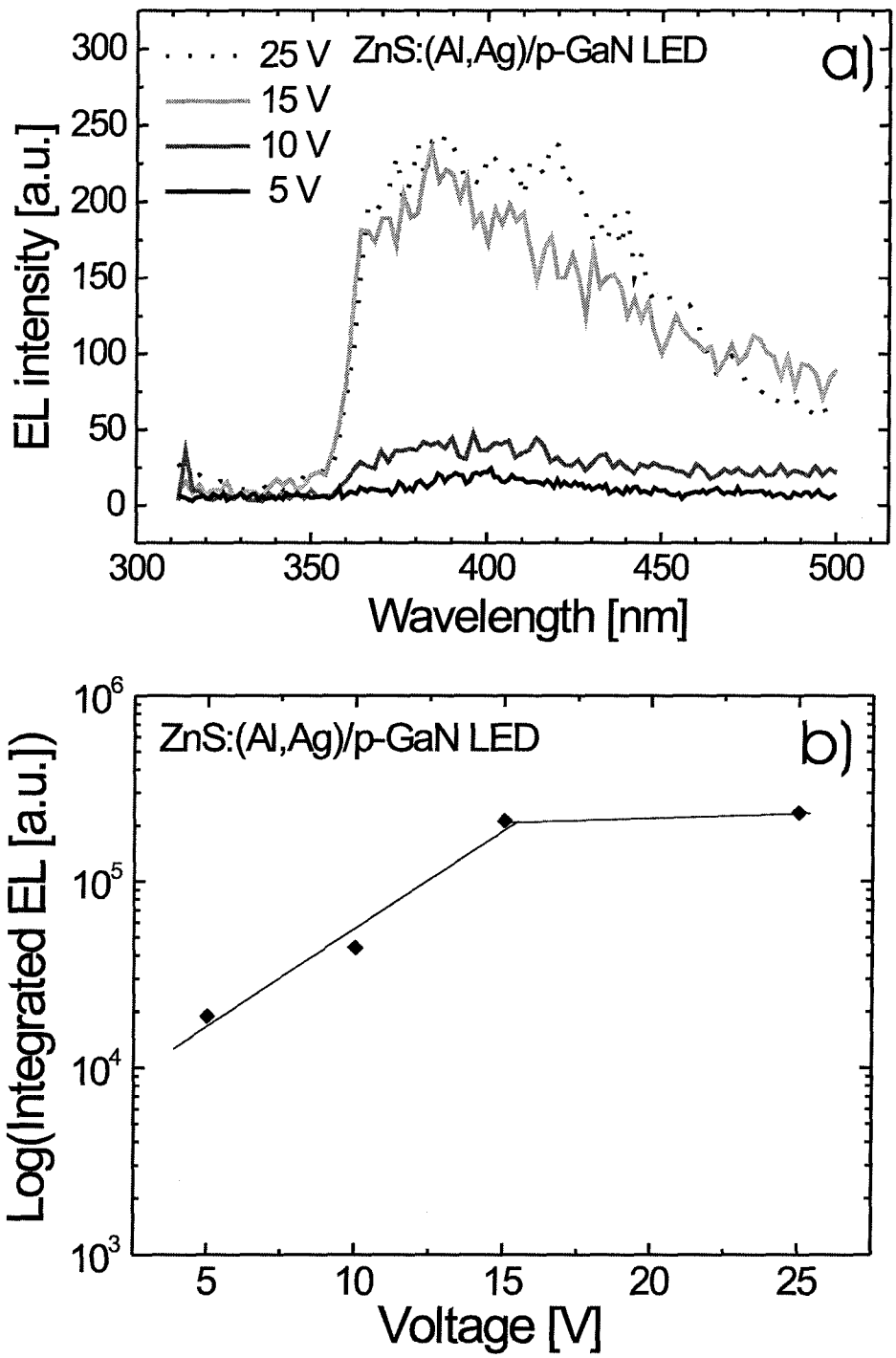

Figure 8.14: a) Room temperature EL as a function of device bias. EL emission is centered around $385-400$ nm, depending on bias voltage with width of luminescence peak varying from 45 nm (at 5 V), to approximately $90-110$ nm (at 10 V and above). b) Integrated EL emission intensity as a function of device bias. We can notice saturation at ≈ 15 V. (EL scan by Z. Bandić.)

tacts are problematic for both the n-ZnS and the p-GaN. The low lying valence band of GaN, which makes it useful as a hole injector for ZnS, also makes contacting a problem since there are no suitable metals of large enough work function to eliminate a Schottky barrier. Likewise, the conduction band of ZnS is rather high, requiring a contact metal of extremely small work function. Small work function metals usually are highly chemically reactive and have a tendency to oxidize. Improvement of contacts is where efforts should be placed to continue the research of these devices. Device performance is also likely limited by the rather poor crystalline quality of MBE-grown ZnS layers. Since the luminescence properties were correlated to the structural crystal quality, devices may be able to benefit from solid phase recrystallization (section 8.4), although the high temperatures involved may cause a significant amount of interdiffusion at the interface. In this mixed III-V/II-VI heterostructure, interdiffusion such as Zn diffusing into the nitride layer or Ga diffusing into the sulfide layer, would cause doping of the adjacent layers. Ga is known to act as a donor in ZnS and Zn a deep acceptor in GaN.

8.6 Summary and conclusion

The n-ZnS/p-GaN heterojunction was described as a novel visible light emitter. In the development of these devices, the MBE growth of ZnS crystalline films was carried out on p-GaN (0001), GaAs (001) and sapphire (0001) substrates. Since p-GaN layers are expensive and largely unavailable, a significant amount of the ZnS growth studies were performed on sapphire substrates. Using a valved cracking source for elemental sulfur, it was shown that crystalline films could be grown that usually contained a high number of stacking faults and twins as observed by RHEED. X-ray diffraction and SEM electron channeling pattern analysis, used to characterize the ZnS structural quality, indicated that the ZnS films were single crystalline with a high degree of mosaic domain tilts and twists. The structural quality of the ZnS films on sapphire was found to be vastly improved by a high temperature recrystallization process. Doping of ZnS was accomplished with aluminum and silver, which act as

shallow donor and deep acceptor centers, respectively. Cathodoluminescence and photoluminescence were very bright for optimally doped films, with emission centered on the 450 nm wavelength Ag blue "low energy" peak. A comparison of growths done on different substrates, including GaN, GaAs, and sapphire, demonstrated an obvious correlation between crystalline quality and luminescence intensity.

ZnS films doped with Al and Ag which were grown on Mg-doped GaN layers were fabricated into p-GaN:Mg/n-ZnS:(Al,Ag) LED structures. Current-voltage and electroluminescence results for these devices indicate diode-like behavior with a slow forward turn on of $3-4$ Volts. The electroluminescence spectrum is blue-violet at turn on, shifting slightly to violet emission at 15 V forward bias, where intensity saturates. This shift to violet likely indicates that electrons from the ZnS layer are transporting across the interface into the GaN layer and recombining at the deep Mg acceptor centers.

Bibliography

[1] M. Yokoyama, K. Kashiro, and S. Ohta, *J. Cryst. Growth* **81**, 73 (1987).

[2] I. P. McClean and C. B. Thomas, *Semicond. Sci. Technol.* **7**, 1394 (1992).

[3] T. Yao and S. Maekawa, *J. Cryst. Growth* **53**, 423 (1981).

[4] J. W. Cook, Jr., D. B. Eason, R. P. Vaudo, and J. F. Schetzina, *J. Vac. Sci. Technol. B* **10**(2), 901 (1992).

[5] K. B. Ozanyan, L. May, J. E. Nicholls, J. H. C. Hogg, W. E. Hagston, B. Lunn, and D. E. Ashenford, *Solid State Commun.* **97**, 345 (1996).

[6] O. Kanehisa, M. Shiiki, M. Migita, and H. Yamamoto, *J. Cryst. Growth* **86**, 367 (1988).

[7] S. Ohta, K. Kashiro, and M. Yokoyama, *J. Cryst. Growth* **87**, 217 (1988).

[8] K. Yoneda, T. Toda, Y. Hishida, and T. Niina, *J. Cryst. Growth* **67**, 125 (1984).

[9] J. E. Ayers, S. K. Ghandhi, and L. J. Schowalter, *J. Cryst. Growth* **113**, 2156 (1991).

[10] E.C. Piquette, Z.Z. Bandic, J.O. McCaldin, and T.C. McGill, *Mat. Res. Soc. Symp. Proc.* **449**, 385 (1997).

[11] E.C. Piquette, Z.Z. Bandic, J.O. McCaldin, and T.C. McGill, *J. Vac. Sci. Technol. B* **15**, 1148 (1997).

[12] Linus Pauling, *General Chemistry* (Dover, New York, 1970).

[13] Precious Metal Platers, Minneapolis, Minnesota.

[14] M. Volmer and A. Weber, *Z. Phys. Chem.* **119**, 277 (1926).

[15] K. Ichino, T. Onishi, Y. Kawakami, S. Fujita, and S. Fujita, *J. Cryst. Growth* **138**, 28 (1994). See Discussion section.

[16] Z. Z. Bandić, E. C. Piquette, J. O. McCaldin, and T. C. McGill, *Appl. Phys. Lett.* **72**, 2862 (1998).

[17] W. Van Gool, Thesis, University of Amsterdam, January (1961).

[18] *Physics and Chemistry of II-VI Compounds*, edited by M. Aven and J.S. Prener (North-Holland, Amsterdam, 1967).

[19] F.J. Humphreys and M. Hatherly, *Recrystallization and related annealing phenomena* (Elsevier Science Inc., New York, 1995).

[20] See for example M.J. Brau and R.A. Reynolds, US Patent N°3, 849, 205, (1974).

[21] R. Triboulet, J.O. Ndap, A. Tromson-Carli, P. Lemasson, C. Morhain, and G. Neu, *J. Cryst. Growth* **159**, 156 (1996).

[22] R. Triboulet, J.O. Ndap, A. El Mokri, A. Tromson-Carli, and A. Zozime, *J. De Phys. IV* **5**, 141 (1995).

[23] E. Tournie, C. Morhain, G. Neu, M. Laügt, C. Ongaretto, J.P. Faurie, R. Triboulet, and J.O. Ndap, *J. Appl. Phys.* **80**, 2983 (1996).

[24] M. Meshkinpur, M.S. Goorsky, G. Chu, D.C. Streit, T.R. Block, and M. Wojtowitz, *Appl. Phys. Lett.* **66**, 748 (1995). See also Reference [23].

[25] F.C. Brown, *The Physics of Solids - Ionic Crystals, Lattice Vibrations and Imperfections* (Benjamin, New York, 1967).

[26] JSM-6400 Scanning Microscope, Manual, Chapter 5, JEOL Ltd. (1989).

[27] A. Koma, *Prog. Crystal Growth and Charact.* **30**, 129 (1995).

[28] A. Osinsky, M. S. Shur, R. Gaska, and Q. Chen, *Electron. Lett.* **34**, 691 (1998).